Marili
Viitak Poço

Estudo numérico dos processos de transporte de sedimentos na Plataforma Continental Noroeste Ibérica

Numerical study of sediment-transport processes in Northwest Iberian Continental Shelf

Marili
Viitak Poço

Estudo numérico dos processos de transporte de sedimentos na Plataforma Continental Noroeste Ibérica

Numerical study of sediment-transport processes in Northwest Iberian Continental Shelf

Dissertação apresentada à Universidade de Aveiro para cumprimento dos requisitos necessários à obtenção do grau de Doutor em Ciência, Tecnologia e Gestão do Mar, realizada sob a orientação científica do Doutor Jesús Dubert, Prof. Auxiliar do Departamento de Física da Universidade de Aveiro e Investigador científico do Instituto de Investigaciones Marinas, IIM-CSIC, Vigo, da Doutora Carmen G. Castro, Cientista titular de Departamento de Oceanografia do IIM-CSIC, Vigo, e da Doutora Rita Nolasco, Investigadora contratada do IIM-CSIC, Vigo.

Apoio financeiro da Fundação para a Ciência e Tecnologia (FCT) através da bolsa de doutoramento SFRH/BD/131256/2017, no âmbito do Quadro de Referência Estratégico Nacional (QREN) e do Programa Operacional de Potêncial Humano (POPH), comparticipado pelo Fundo Europeu e por fundos nacionais do Ministério da Ciência, Tecnologia e Ensino Superior (MCTES). Mais a bolsa COVID/BD/152592/2022. Este trabalho é uma contribuição ao projeto HABWAVE LISBOA-01-0145-FEDER-031265, co-financiado por fundos EU ERDF, dentro do PT2020 Partnership Agreement and Compete 2020, e por fundos nacionais através da Fundação para a Ciência e Tecnologia, I.P.(FCT, I.P.). É agradecido o financiamento à UI/LA CESAM pela FCT/MCTES (UIDP/50017/2020+UIDB/50017/2020+LA/P/0094/2020), através de fundos nacionais, com co-financiamento do FEDER, PT2020 e Compete 2020.

One step at a time is all it takes to get you there

Emily Dickinson

O júri / the jury

Presidente / president

Prof. Doutora Isabel Cristina Saraiva de Assunção Rodrigues Salak
Professora Catedrática, Universidade de Aveiro

Vogais / examiners committee

Prof. Doutor Rui Pires de Matos Taborda
Professor Associado com Agregação, Universidade de Lisboa

Doutora Anabela Tavares Campos Oliveira
Técnica Superior, Instituto Hidrográfico

Prof. Doutor Paulo Manuel Cruz Alves da Silva
Professor Auxiliar, Universidade de Aveiro

Prof. Doutora Ana María Bernabéu Tello
Professora Catedrática, Universidad de Vigo

Prof. Doutor Jesús Manuel Pedreira Dubert
Professor Auxiliar da Universidade de Aveiro (Orientador)

Acknowledgements

Thanks are due for all the people and events in my life that led to the beginning and end of this beautiful chapter in my academic studies.

I am grateful for the support and guidance provided by my supervisors and the entire working group. Thank you, Jesús Dubert, for accepting me to be part of your team, surrounding me with talented and dedicated people and trusting me with this challenge. The knowledge, guidance, and encouragement of Rita Nolasco have been invaluable and meant the world to me. The expertise and feedback of Carmen G. Castro, Nicolás Villacieros-Robineau and Paulo Silva have been instrumental in helping me achieve my academic goals, and I cannot thank them enough for their contributions to my success.

Thanks are due to Tiago Luna and Alfredo Rocha from the Group of Climatology and Meteorology of Aveiro University for providing the WRF data, which was critical for the elaboration of this thesis.

Thanks are also due to Puertos del Estado, Spain, for the Silleiro buoy data, to Confederación hidrográfica Miño-Sil for the river Minho Flow data and to CMEMS and IBI-MFC for providing the data used as boundary and initial conditions.

I also want to extend my gratitude to everyone who has supported me along the way, including my family, friends, and colleagues. Thank you for being there for me through the ups and downs of my academic journey and for being a source of strength and inspiration.

Palavras-chave Modelação numérica, CROCO, plataforma continental do Noroeste Ibérico, transport sedimentar, BBL, variabilidade sazonal, afloramento costeiro, rios.

Resumo O transporte de sedimentos na plataforma continental influencia muitas áreas interdisciplinares, incluindo problemas ecológicos e sociais. Compreender os processos subjacentes que controlam o transporte de sedimentos é essencial para a gestão costeira, a distribuição de nutrientes, de poluentes e da abundância da fauna e flora bentónica, que podem impactar toda a cadeia alimentar no ecossistema marinho. O presente trabalho visa melhorar a compreensão da variabilidade espacial e temporal do transporte de sedimentos, na plataforma continental do Noroeste Ibérico. Utilizando ferramentas numéricas, este estudo procura melhorar a compreensão dos processos físicos que afetam o transporte de sedimentos nesta região. Um modelo oceânico 3D CROCO (v1.0), que inclui um módulo integrado de transporte de sedimentos, foi implementado e configurado para este estudo. Este sistema foi acoplado com um modelo de ondas e com um modelo atmosférico durante um ciclo anual completo, de nov. de 2008 até dez. de 2009. Um conjunto de dados *in situ* foram utilizados para validar, com sucesso, os resultados do modelo. A análise estatística e quantitativa do sistema de modelação demonstrou uma concordância relativamente boa com os dados observados. Os padrões de transporte de sedimentos, foram influenciados pela sazonalidade da dinâmica da plataforma continental e pela atividade das ondas. Embora se tenha observado um transporte em geral fraco durante a primavera, o verão e o outono, observou-se um transporte considerável durante o inverno, associado a tempestades. A circulação da plataforma, em resposta aos forçamentos atmosféricos, determinou a direção do transporte, enquanto a energia das ondas regulou a re-suspensão dos sedimentos. Os eventos de afloramento e afundamento induzidos pelas tempestades, promoveram o transporte de sedimentos para Sul e para Norte respetivamente, principalmente na camada limite de fundo. As características morfológicas da plataforma e a dinâmica frontal de interação entre as águas oceânicas e as águas mais doces, limitaram o transporte transversal de sedimentos em suspensão. Na região norte da zona de estudo, foi ainda possível observar a formação de vôrtices junto ao fundo, criando vias de transporte de sedimentos para o oceano aberto. O fluxo de matéria em suspensão de origem fluvial foi modelado com sucesso.

Keywords Numerical modelling, CROCO, NW Iberian Continental Shelf, sediment transport, BBL, seasonal variability, coastal upwelling system, rivers.

Abstract Sediment transport in the continental shelf regions affects many interdisciplinary areas, including ecological and social problems. Understanding the underlying processes influencing sediment transport is essential for coastal management, distribution of nutrients, pollutants and abundance of benthic fauna and flora, which can impact the entire food chain in the marine ecosystem. The present work aims to enhance our understanding of spatial and temporal variability of sediment transport in the NW Iberian Continental Shelf. By using numerical tools, this study seeks to provide new insights into physical processes affecting sediment transport at different time scales. State-of-the-art 3D oceanic numerical model CROCO (v1.0), which includes an integrated sediment transport module, was implemented and configured for this application. The modelling system was coupled offline with 2D spectral wave and atmospheric models. The model simulation covered an entire annual cycle from November 2008 to December 2009, and available in situ data was used to validate the results. The statistical and quantitative analysis of the modelling system demonstrated a relatively good agreement with the observational data sets. The sediment transport patterns were influenced by the seasonality of the shelf dynamics and wave activity. While low sediment movement was observed during spring, summer and autumn, considerable transport could be seen during winter, associated with storms. The shelf circulation, driven in response to atmospheric forcing, determined the transport direction, while wave energy regulated the re-suspended sediment mass. The storm-driven upwelling and downwelling events promoted the Southward and Northward transport of sediments mostly through the Bottom Boundary Layer. The morphological features of the shelf and the frontal dynamics between the oceanic and fresh water in the mid-and inner shelf limited the cross-shore transport of suspended sediments. In the Northern region of the study area, a formation of shelf-scale near-bottom eddies was modelled, creating sediment transport pathways to the open ocean. River inflow of suspended matter was also successfully simulated.

Contents

List of Figures

List of Tables

List of Abbreviations

BBL	Bottom Boundary Layer
CESAM	Centro de Estudos do Ambiente e do Mar
CROCO	Coastal and Regional Ocean COmmunity model
CSTM	Community Sediment Transport Model
GETM	General Estuarine Transport Model
IH	Instituto Hidrográfico
IPC	Iberian Poleward Current
mab	meters above the bed
MAPAMA	Ministero de Agricultura y Pesca, Alimentación y Medio Ambiente
MUSTANG	MUd and Sand TranSport modelliNG
NWCIP	NW Coast of the Iberian Peninsula
NW	Northwest
POC	Particulate Organic Carbon
POM	Princeton Ocean Model
q-q plot	quantile-quantile plot
RMSE	Root Mean Square Error
ROMS	Regional Ocean Modeling System
SST	Sea Surface Temperature
SWAN	Simulating Waves Nearshore
SNIRH	Sistema Nacional de Informação de Recursos Hídricos
SWAT	Soil Water Assessment Tool
SPM	Suspended Particulate Matter
USGS	United States Geological Survey
WAM	Wave Modelling
WENO	Weighted Essentially Non-Oscillatory
WIBP	Western Iberian Buoyant Plume
WKB	Wentzel–Kramers–Brillouin approximation
WRF	Weather Research and Forecasting Model
WWIII	WAVEWATCH III

Chapter 1

Introduction

1.1 State of the art and motivation

Coastal regions are an important part of the global carbon cycle despite their relatively small surface area in the oceans. Characterized by high primary production and downward flux of POC (Particulate Organic Carbon), creating a potentially large sink for CO_2 burial (*Karakaş et al.*, 2006). Likely, the unburied part is transported from the continental margin to the open ocean in dissolved and suspended particulate form (*Wollast*, 1998; *Bauer and Druffel*, 1998; *Muller-Karger et al.*, 2005; *Liu et al.*, 2010) through the surface, intermediate and bottom nepheloid layers, in which the lateral transport is highly affected by the bottom boundary layer dynamics (*Thomsen*, 2002; *Hwang et al.*, 2010).

The mid-shelf mud depocenters are one of the major sinks for material coming from the land, formed through the near-bottom sediment dispersal and accumulation on the shelf (*Hanebuth et al.*, 2015). These mud belts contain valuable information about the global source-to-sink system and environmental variability (*Sommerfield and Wheatcroft*, 2007; *Hanebuth and Lantzsch*, 2008). In addition, due to the relatively calm hydrodynamic conditions, these areas serve as cradles of life (*Rosenberg*, 2001). In general, the soft-bottomed sediment hosts some of the ocean's highest benthic biodiversity, which in return greatly influences the higher trophic levels (*Gray et al.*, 1997; *Thrush and Dayton*, 2002). The Northwest (NW) Iberian shelf is known as one of Europe's most important fishing areas, therefore the understanding of spatial and temporal variability of the seafloor is vital for effective marine governance.

Various studies have been performed on the NW Iberian shelf, addressing the patterns of sediment transport and the spatial distribution, along with the bottom nepheloid layer behaviour (*Dias et al.*, 2002b; *Huthnance et al.*, 2002; *Oliveira et al.*, 2002a; *Thomsen et al.*, 2002; *Vitorino et al.*, 2002a; *Van Weering et al.*, 2002; *Villacieros-Robineau et al.*, 2013; *Oberle et al.*, 2014; *Zhang et al.*, 2016; *Villacieros-Robineau*, 2017; *Villacieros-Robineau et al.*, 2019). Several studies have demonstrated the advantages of numerical models while covering different temporal and spatial scales. Among others, to investigate the continental shelf circulation (*Oliveira et al.*, 2009), characterize wave climate (*Rusu and Guedes Soares*, 2009; *Semedo et al.*, 2011) and atmospheric conditions in morphodynamic studies (*Gonçalves et al.*, 2014), reproducing quite realistically the actual processes (*Rusu and Soares*, 2013; *Carvalho et al.*, 2014; *Cordeiro et al.*, 2015). Nevertheless, until now, only

a handful of numerical modelling studies have been performed to represent the sediment transport in the NW Iberian shelf. *Davies et al.* (2002) studied the sediment transport at the Iberian margin using idealized winds in the simulations. *Xing and Davies* (2003a) investigated suspended sediment transport due to tides and the influence of wind direction, waves and density stratification (*Xing and Davies*, 2002) focusing on the shelf edge areas. The three studies referenced above (*Davies et al.*, 2002; *Xing and Davies*, 2003a, 2002) used a 2D model consisting of a cross-shelf section, leaving aside the alongshore variability of the coastal circulation. *Oberle et al.* (2014) simulated the wave-driven changes on the seabed using only a wave model, neglecting the influence of other forces. They considered the seasonal and storm-specific wave conditions, showing a strong influence of medium to severe storm events on the overall seabed mobilisation. *Zhang et al.* (2016) studied the storm-driven bottom sediment transport for one month in September 2014, considering currents and waves.

All the numerical modelling that has been done so far, in the area of fine-grained sediment transport in the NW Iberian shelf, still has left some unanswered questions and does not provide information about the long-term spatial and temporal variability. There is a need for a better understanding of these mechanisms and the assessment of longer-period sediment budgets. This information would be valuable for several interdisciplinary areas, where sediment transport is a key factor, for instance, studies of benthic habitats (*Snelgrove*, 1999), coastal management (dredging and beach nourishment), resuspension of contaminants associated with the sediments resuspension, detection of oil-spill deposition, effects of sediments in fisheries (aquaculture, trawling) and development of coastal and seafloor structures (platforms, pipelines, cables), among others.

The present PhD thesis aims to provide a new insight into the underlying processes affecting the spatial and temporal variability of sediment transport in the NW Iberian continental shelf. For this purpose various numerical models were implemented, simulating hydrodynamics, waves and suspended sediment transport. Chapter 2 presents a detailed description of the models, set-up and configuration applied to study the sediment movement on the shelf. An application of the spectral wave model used to include the wave forcing is shown in Chapter 3. The published chapter evaluates the influence of wind data from various sources on wave modelling in the area of interest. Next, Chapter 4, concentrates on the assessment of the developed modelling system to study the sediment transport processes. An extensive comparison with the observational data sets is performed, demonstrating the capabilities and shortcomings of this application. The successful validation of the models, allowed us to gain knowledge about the importance of different phonemes controlling the sediment transport and their interrelationship, from which the fifth chapter, 5, arose. The results of the previous chapter were the motivation to create an even more sophisticated simulation. The sediment input from the rivers was added, permitting to study the fate of sediments coming from the river systems in Chapter 6.

1.2 Objectives

The fundamental objectives of the present study are the implementation and configuration of a modelling system, followed by the analysis of the results. This is to understand the dynamical mechanisms of transport of fine-grained sediments on the continental shelf and to better comprehend the underlying physical processes in the NW Iberian shelf. To fulfil these objectives, this work is based on recent and current international project results, like the ones obtained under the scope of the RAIA, RAIA.co and MarRisk, involving this region's scientific community, and supported by collaboration with researchers from internationally referenced institutions (Centro de Estudos do Ambiente e do Mar, University of Aveiro – CESAM-UA, Aveiro, Portugal and Instituto de Investigaciones Marinas – CSIC, Vigo, Spain). The scientific development objectives are:

- Development of a modelling system including high resolution 3D oceanic model with a sediment transport module, coupled offline with a spectral 2D wave model and an atmospheric model. The sediment transport module allows to solve the re-suspension, transport and suspension processes of sediments (coarse and fine sands).
- Validation of the modelling system, with the available historic observational data.
- Study the physical processes affecting sediment transport at different time scales, from short-term processes (storm events) to inter-annual variability.

  The three main research questions to answer are:

1. What is the role of the driving forces (waves, shelf circulation, river and estuarine outflows, meso- and submesoscale circulation, among others) on the sediment transport and sediment patterns in the NW Iberian Peninsula continental shelf?
2. What happens to the re-suspended sediments and what quantity is exported to the adjacent ocean?
3. What is the fate of the sediment input from the river systems of the study area?

To sum up, we are looking to give a quantitative comprehension of the transport processes that carry material from source to sink to explain the existence of different geologic signatures (for example, mud patches, etc.).

1.3 Characterization of the Western Iberian Margin

The study site, NW Iberian continental margin (*Rey et al.*, 2014), includes the Galician Continental shelf and the northern part of the Portuguese Continental shelf. Hundreds of kilometres long coastline is configured by the presence of rivers, rocky outcrops and sandy dunes. The shelf is narrow, about 30 km, off from the Galician Rías and slightly broader elsewhere, around 50 km (*Maestro et al.*, 2013). The continental slope in the North is

steep and a wide re-entrance arc is formed in the outer shelf. Whereas, in the South, the continental shelf is gentle and a barrier is formed in front of the shelf break by rock plateaux (*Dias et al.*, 2002a).

The two most important rivers providing fresh water and particulate matter to the shelf, are Minho in the North and the Douro in the South. It has been estimated that the Douro River introduces approximately 87 % of the fluvial sediments to the shelf (*Dias*, 1987). In addition, along the NW Iberian continental margin, there are several smaller estuaries like Ave, Cávado, Lima and Galician Rías, which also contribute, but likely to a smaller extent. In the last decades, the intensive construction of dams in the rivers has drastically reduced the sediment input to the shelf (*Jouanneau et al.*, 2002).

Several authors have found that the inner and mid-shelf in the study area are greatly decoupled from the large-scale ocean circulations which prevail off the shelf edge along the Iberian margin and the hydrodynamic system is mainly driven by tides and wind-forced currents on the shelf (*Csanady and Shaw*, 1983; *Relvas et al.*, 2007; *Zhang et al.*, 2016).

Two atmospheric systems, the Azores high-pressure area and Iceland's low-pressure area, are influencing the shelf dynamics in the study area (*Wooster et al.*, 1976). Seasonal variations in these systems create two mean circulation patterns: downwelling from October to March, caused by predominant southerly winds and upwelling from April to September due to the north-easterly winds. Over the slope density-driven Iberian Poleward Current (IPC) flows Northward, carrying warm and saline waters from the Southern regions to the NW Iberian continental margin (*Frouin et al.*, 1990; *Haynes and Barton*, 1990; *Peliz et al.*, 2003a,b). The current intensifies during the winter period due to the prevalent downwelling conditions (*Teles-Machado et al.*, 2016). Downwelling promotes the onshore advection of surface waters, creating a thermohaline front between the saline oceanic waters and freshwater exported from the rivers, generating buoyant plumes over the shelf, named generically as the WIBP (West Iberian Buoyant Plume) (*Peliz et al.*, 2002; *Mendes et al.*, 2016). The location and extent of the plume are determined by the prevalent wind forcing. Under Southerly wind the plume is constrained against the coast, constricting the coastal waters to the shelf and impeding the cross-shelf exchange between the shelf waters and the ocean (*Castro et al.*, 1997; *Álvarez-Salgado et al.*, 2003). When forced by Northerly winds the plume can dislocate more across the shelf, mainly in the surface layers.

The wave regime of the study area is strongly seasonal and highly energetic, especially during the winter and transition periods. Typical winter conditions are dominated mostly by NW swells while occasionally turning to SW, characterized by a significant wave height of about 3-4 m and a mean period of 8-9 s (*Vitorino et al.*, 2002b). During storm events, wave height exceeds 5 m and periods over 10 s occur (*Lorente et al.*, 2017). Although waves more than 7 m in height with periods around 13 s or higher are not uncommon (*Pita and Santos*, 1989; *PO-Waves Group*, 1994). The summer wave regime is mild, with significant wave heights < 3 m and mean period < 8 s (*Vitorino et al.*, 2002b,a).

Chapter 2

Modelling system

2.1 Introduction

The advances in the computational capabilities of computers have opened a way for the development of more complex numerical model configurations. This has allowed a multidisciplinary approach for representing various processes in different spatial- and time scales (*Li et al.*, 2017; *Pinto et al.*, 2012; *Sykes and Barciela*, 2012; *Warner et al.*, 2008). Improved measurement equipment and new techniques have made it possible to gather more data and given access to areas with difficult environmental conditions (e.g. stormy continental platform, deep sea, interactions between ocean-atmosphere, sediment composition) (*Bosnic*, 2017; *Zhang et al.*, 2016; *Villacieros-Robineau et al.*, 2019). This new insight and information about different aspects of regional oceanography have been also exploited in numerical models. The continuous improvement of numerical description of physical processes, and assimilation of measurement data into the systems, has remarkably improved the quality and reliability of modelling results (*Kari et al.*, 2017; *Miles et al.*, 2015).

Numerical models are successfully representing atmospheric dynamics (e.g WRF - *Skamarock et al.* (2019)), hydrodynamics (e.g ROMS - *Shchepetkin and McWilliams* (2005), CROCO - *Debreu et al.* (2012), POM - *Blumberg and Mellor* (1987), GETM - *Burchard and Bolding* (2002)), wave propagation (SWAN - *Booij et al.* (1999), WWIII - *Tolman* (1989), WAM - *WAMDIG* (1988)) and sediment-transport (CSTMS - *Warner et al.* (2008), MUSTANG - *Le Hir et al.* (2011), USGS - *Sherwood et al.* (2005)). Taking advantage of each of these model abilities and their coupling capabilities, numerous modelling systems have been developed to study coastal morphology and sediment transport. These systems generally interconnect hydrodynamics, turbulence and wave models, providing information about the dynamical forcing to estimate the shear stresses in the bottom layers for example through parameterizations or using Bottom Boundary Layer models (BBL). These various approaches implemented in modelling systems, distinguish them, giving each one its advantages and disadvantages.

The choice of a numerical model and its assessment, is one of the fundamental components, determining the success of a modelling study. *Amoudry and Souza* (2011), presents a detailed synopsis of five widely used modelling systems: ROMS, Delft3D, ECOMSED,

TELEMAC and MIKE. These systems present distinct strengths and shortcomings, regarding coastal zone modelling, both physical and numerical. Moreover, they are facing more general issues related to the empirical nature of the characterisation of sediment transport, turbulence closure schemes and parametrization. Challenges also arise from the representation of large- and small-scale processes, where one is governed by simple and well-understood principles (e.g. conservation of mass) and the other includes complex and still poorly understood processes (e.g shear stress estimates, re-suspension of sediments in the bottom boundary layer, formation of bedforms, etc). The different time scales associated with these processes make the problems even more elaborate. The uncertainties in models are also increased, by neglecting mixed beds, cohesive sediments and biological effects, among other things.

In the present study, an off-line modelling system was developed using the new CROCO v1.0 based on the ROMS-AGRIF hydrodynamic model (*Shchepetkin and McWilliams*, 1998, 2003, 2005; *Penven et al.*, 2006), with sediment-transport capabilities (CSTM, *Blaas et al.* (2007)), coupled offline with spectral wave model SWAN (*Booij et al.*, 1999) and atmospheric model WRF (*Skamarock et al.*, 2019). The hydrodynamic model ROMS-AGRIF was chosen due to the extensive experience of the investigation group with this model, which has led to a successful implementation and fine-tuned configuration of the model for the study area e.g. *Nolasco et al.* (2013); *Cordeiro* (2018); *Cordeiro et al.* (2021). The sediment model applied in this thesis is integrated into the CROCO system, making its use very accessible and effective. The wave model SWAN was selected due to the previous experience and knowledge of the doctorate student (*Viitak et al.*, 2016, 2020).

2.2 SWAN

SWAN is a third-generation spectral wave model developed at the Delft University of Technology, Netherlands. Wave generation and propagation over a realistic bathymetry are described with a two-dimensional wave action density spectrum N (*Booij et al.*, 1999).

$$N(\sigma,\theta) = \frac{E(\sigma,\theta)}{\sigma} \tag{2.1}$$

where $E(\sigma,\theta)$ is the wave energy density, σ relative frequency as observed in a frame of reference moving with current velocity and θ the wave propagation direction. An action balance equation is solved to describe the evolution of the action density N, without any *a priori* restrictions on the spectrum, which reads

$$\frac{\partial N}{\partial t} + \nabla_{\vec{x}} \cdot [(\overrightarrow{c_g} + \overrightarrow{U})N] + \frac{\partial c_\sigma N}{\partial \sigma} + \frac{\partial c_\theta N}{\partial \theta} = \frac{S_{tot}}{\sigma} \tag{2.2}$$

where the second term represents the propagation of wave energy in two-dimensional geographical $\overrightarrow{x}$-space, with wave group velocity $\overrightarrow{c_g}$ and the ambient current $\overrightarrow{U}$. The third term stands for the effect of shifting of the relative frequency due to variations in depth and mean currents. Finally, the fourth term designates depth- and current-induced refraction.

c_σ and c_θ terms symbolize the wave propagation velocities in spectral space (σ, θ). So, the left-hand side of the equation represents the kinematics, and on the right-hand side all the physical processes that generate, dissipate or redistribute the wave energy. The S_{tot} contains the source/sink terms

$$S_{tot} = S_{in} + S_{nl3} + S_{nl4} + S_{ds,w} + S_{ds,b} + S_{ds,br} \tag{2.3}$$

These terms represent wave growth by the wind, nonlinear transfer of wave energy through three- and four-wave interactions, and dissipation of wave energy due to white-capping, bottom friction and depth-induced wave breaking, respectively. For more detailed information about different formulations in the wave model, the Scientific and Technical Documentation of SWAN should be consulted (*SWAN*, 2013).

2.3 CROCO

CROCO is a free-surface split-explicit oceanic model using terrain-following curvilinear coordinates (*Shchepetkin and McWilliams*, 2003, 2005).

The free-surface ζ of the ocean is represented as a function of space (x, y) and time (t) $\zeta = \zeta(x, y, t)$. This approach is more realistic, allowing the ocean surface to continuously change.

A split-explicit time-stepping scheme divides the solution into a barotropic (i.e. depth independent) and baroclinic mode. This makes it possible to advance the surface elevation and barotropic momentum, using a short time step and a much larger one, for 3-dimensional variables like salinity, temperature and baroclinic momentum.

The vertical S-coordinate system enables the model to adapt to the irregularities of the bathymetry, maintaining the number of levels, consequently, the resolution is higher in shallower areas and smaller in deeper regions. To reduce the error in the pressure gradient calculations, when using the S-coordinate, an advection scheme based on the work done by *Marchesiello et al.* (2009) is adopted. Arakawa C-grid is used for horizontal discretization, where velocity vectors are defined in the grid faces and the rest of the variables inside the grid cells.

The incompressible primitive equation can describe the ocean state to a good approximation (2.4, 2.5, 2.6). So, CROCO solves the simplified Navier-Stokes equation, using the Boussinesq and hydrostatic approximations (2.7), along with the advective-diffusive equation (2.8) and a nonlinear equation of state (2.9). The following equations are in Cartesian coordinates, where u, v, w are the x, y, z (longitude, latitude, depth) components of vector velocity $\overrightarrow{\mathbf{v}}$, $f(y)$ Coriolis parameter $2\Omega \sin\phi$, $\Phi(x, y, z, t)$ the dynamic pressure $\Phi = P/\rho_0$, with P the total pressure and $\rho = \rho_0 + \rho^{'}$ the water density (ρ_0 the average density and $\rho^{'}$ the perturbation), $\mathcal{F}_u, \mathcal{F}_v, \mathcal{F}_C$ denote the forcing terms, $\mathcal{D}_u, \mathcal{D}_v, \mathcal{D}_C$ represent the diffusive terms. For a more thorough description, consult *Shchepetkin and McWilliams* (2003, 2005).

The momentum balance in the x and y directions is expressed in terms of grid-scale and subgrid-scale velocity components. The vertical fluxes of the latter are parametrized using turbulent closure schemes.

$$\frac{\partial u}{\partial t} + \vec{\nabla}.(\vec{\mathbf{v}}\, u) - fv = -\frac{\partial \Phi}{\partial x} + \mathcal{F}_u + \mathcal{D}_u \tag{2.4}$$

$$\frac{\partial v}{\partial t} + \vec{\nabla}.(\vec{\mathbf{v}}\, v) + fu = -\frac{\partial \Phi}{\partial y} + \mathcal{F}_v + \mathcal{D}_v \tag{2.5}$$

The continuity equation for an incompressible fluid is expressed as,

$$\vec{\nabla}.(\vec{\mathbf{v}}) = \frac{\partial u}{\partial x} + \frac{\partial v}{\partial y} + \frac{\partial w}{\partial z} = 0 \tag{2.6}$$

The hydrostatic approximation assumes that there is a balance between the vertical pressure gradient and the buoyancy force. All the non-hydrostatic processes must be parametrized.

$$\rho_0 \frac{\partial \Phi}{\partial z} = -\rho g \tag{2.7}$$

where g is the acceleration of gravity.

The advective-diffusive equation expresses the time evolution of a scalar concentration field $C(x, y, z, t)$ such as salinity, temperature and sediment concentration.

$$\frac{\partial C}{\partial t} + \vec{\nabla}.(\vec{\mathbf{v}} C) = \mathcal{F}_C + \mathcal{D}_C \tag{2.8}$$

The equation of state,

$$\rho = \rho(T, S, P) \tag{2.9}$$

2.4 Sediment transport

The USGS sediment model, derived from the UCLA/USGS ROMS community, is used in this application (*Blaas et al.*, 2007; *Warner et al.*, 2008; *Shafiei et al.*, 2022). It is embedded as a module in CROCO.

This study concentrates only on the suspended sediment movement in the continental shelf, considering that it is the dominant mode of transport for fine sands (*Bosnic*, 2017). Moreover the formation of individual morphologic features, for example, sandbanks or sediment exchange with subaerial beach exceeds the scope of the present application.

2.4.1 Surface sediment distribution

The sediment bed is represented by three-dimensional arrays with a constant number of layers beneath each horizontal model cell. Each cell of the bed is initialized assigning the

following properties: thickness, sediment-class distribution, porosity, and age. Using these values and the grain density, the mass of each sediment class in each cell can be determined (*Warner et al.*, 2008). In addition, the evolving properties of the seabed, including bulk properties of the surface layer, like active-layer thickness, mean grain diameter, mean density, mean settling velocity and mean critical stress for erosion and descriptions of the subgrid-scale morphology (ripples) are stored in two-dimensional arrays (see Appendix A). Based on these properties, estimates of bed roughness are obtained using the BBL formulations, described in more detail in the subgrid-scale processes section 2.4.3 and fed into the bottom stress calculations. The sediment routines use the bottom stresses to determine the resuspension and transport of sediments.

Active layer z_a represents the average vertical dimension of the transport system, interpreted physically as the thickness of the mobile layer, which is estimated at the beginning of each time step (*Harris and Wiberg*, 1997).

$$z_a = k_1 \rho_0 (\tau_{sf} - \overline{\tau_{ce}}) + k_2 D_{50} \tag{2.10}$$

where τ_{sf} (Pa) is the total skin-friction bottom stress caused by the combined maximum wave-current activity, $\overline{\tau_{ce}}$ (Pa) is the critical stress for erosion averaged over all sediment classes, $\rho_0 = 1025$ (kg/m^3) Boussinesq approximation mean density, D_{50} (mm) is the median grain diameter and empirical constants $k_1 = 0.007, k_2 = 6$ (*Jullien et al.*, 2022). When sediments are re-suspended or transported and the thickness of the top layer is less than the z_a, sediment mass from the deeper layers is entrained until the top layer thickness equals z_a. If more than two layers are mixed, then the bottom layer is split, to keep the constant number of layers and conserve the sediment mass. If through deposition processes the top layer thickness exceeds the user-defined threshold, the bottom two layers are combined and a new layer is provided to begin the accumulation of depositing mass. The mass of each sediment class available for transport is limited to the mass available in the active layer. When erosion and deposition have been calculated the active-layer thickness is recalculated and bed layers are readjusted. So, any newly deposited material, with a thickness less than the z_a is lost. In the end, the sediment bed characters, such as D_{50}, ripple geometry etc., are updated, to be used in the bottom stress calculations (*Warner et al.*, 2008).

2.4.2 Suspended sediment transport

Sediments suspended in the water column are transported by solving an advection-diffusion equation:

$$\frac{\partial (H_z C)}{\partial t} + \frac{\partial (u H_z C)}{\partial x} + \frac{\partial (v H_z C)}{\partial y} + \frac{\partial (\Omega H_z C)}{\partial s} = -\frac{\partial}{\partial s}(\overline{c'w'} - \frac{\nu_\theta}{H_z}\frac{\partial C}{\partial s}) + C_{source} \tag{2.11}$$

where H_z is grid-cell thickness, C tracer quantity, u,v and Ω are the mean components of velocity in the horizontal (x-longitude and y-latitude) and vertical (s) directions respectively, time-averaged fluctuating c′ turbulent concentration and w′ turbulent velocity s-direction; ν_θ tracer kinematic diffusivity (*Warner et al.*, 2008). The first term, on the left-hand side, in equation 2.11 represents the changes in time of the sediment concentration rate of a particular size class, the second, third and fourth terms are the horizontal and vertical advection, respectively. On the right-hand side, the first term detonates the mixing processes (*Jullien et al.*, 2022). C_{source} is the tracer source/sink term added for the vertical settling and exchange with the bed, for suspended sediments.

$$C_{source,m} = -\frac{\partial w_{s,m} C_m}{\partial s} + E_{s,m} \tag{2.12}$$

where $w_{s,m}$ is the sediment settling velocity, $E_{s,m}$ erosion source and m is the sediment size class index. Each size class of sediments is treated separately, calculating the net upward flux of eroded material and the deposition flux. The settling velocity $w_{s,m}$ is a user input parameter that does not take into account the flow conditions and hindered settling, depending only on the sediment grain size. The vertical settling of suspended sediments is computed via a semi-Lagrangian advective flux algorithm, using a parabolic vertical reconstruction of suspended sediment in the water column with piece-wise parabolic method (*Colella and Woodward*, 1984) for high-order interpolation and WENO scheme constraints to avoid oscillations (*Liu et al.*, 1994).

Erosion flux is computed following *Ariathurai and Arulanandan* (1978) as,

$$E_{s,m} = E_{0,m}(1-\phi)\frac{\tau_{sf} - \tau_{ce,m}}{\tau_{ce,m}} \tag{2.13}$$

when the total skin-friction bottom stress (τ_{sf}) is higher than the critical shear stress ($\tau_{ce,m}$), $\tau_{sf} > \tau_{ce,m}$. E_s is the surface erosion mass flux, E_0 is the empirical erosion rate, ϕ porosity of the top layer and m is an index for each sediment class. The erosion flux E_s on the sea bed, is limited by the availability of each sediment class in the top layer of the sediment bed.

2.4.3 The Bottom Boundary Layer processes

A regional-scale application does not have the vertical resolution necessary to resolve the wave boundary layer, suspended sediment matter (SPM) and gradients in the velocity field near the bed, which vary significantly over a short vertical distance. These subgrid-scale processes are parameterized in the BBL and currently, two different approaches are implemented. Simple drag-coefficient methods or more complex expressions taking into account the influence of waves and currents over moveable bed (*Jullien et al.*, 2022) to estimate shear stresses at the bottom.

In the current application, the more elaborated approach was used, also applied by *Blaas et al.* (2007), based on the *Soulsby* (1995) formulations for the wave-current activity

and combined with the bottom roughness estimates of *Li and Amos* (2001), *Grant and Madsen* (1982) and *Nielsen* (1986).

The bottom roughness length incorporates three terms,

$$Z_0 = k_s + k_t + k_f \tag{2.14}$$

in which the first is associated with the grain, so-called skin roughness k_s, the second is the sediment transport term k_t and the third is related to bedforms k_f (ripples).

The skin roughness caused by the sediment grains on the bed considers the Nikuradse roughness height, which is related to the roughness length (*Nikuradse*, 1933) as

$$Z_0 = \frac{k_s}{30} \tag{2.15}$$

Depending only on the grain size as $k_s = 2.5D_{50}$, giving a practical conventional measure (*Nielsen*, 1992). The transport roughness k_t is usually the smallest in comparison with the rest of the terms and depends on the thickness of the bedload layer (*Li and Amos*, 2001). The presence of ripples causes a form drag, causing the shear stress to increase from ripple trough to crest (*Grant and Madsen*, 1982; *Nielsen*, 1986).

The maximum wave-current shear stress at the bottom within a wave cycle is obtained by combining the wave-induced shear stress τ_w and current-only bed shear-stress τ_c (Equation 2.20). In the present application, there are no feedback mechanisms between the waves and currents. The maximum wave-current shear stress is then used to determine whether or not the sediments are re-suspended from the seabed (*Jullien et al.*, 2022).

The current shear stress

The current induced bottom shear stress is calculated as,

$$\tau_c = \frac{\kappa^2}{ln^2(z/z_0)} \mid u \mid^2 \tag{2.16}$$

where $\kappa = 0.41$ is von Kármán constant, z is the elevation above the bed, z_0 is the empirical bottom roughness length defined by the user and $\mid u \mid = \sqrt{u^2 + v^2}$, where u and v are the current cross- and along-shore velocity components near the bottom. The von Kármán law formulation assumes that the flow in the BBL has a logarithmic profile, defined by the shear velocity of the current and the bottom roughness.

The wave shear stress

The wave shear stress calculations are based on the following formula,

$$\tau_w = 0.5\rho f_w u_b^2 \tag{2.17}$$

where ρ is the water density, f_w is the wave-friction factor and u_b is the wave orbital velocity. The wave-friction factor f_w is calculated according to *Soulsby* (1995) as,

$$f_w = 1.39(u_b/\omega_p z_0)^{-0.52} \tag{2.18}$$

where the u_b is determined from significant wave height H_s and wave peak frequency ω_p, using the Airy wave theory:

$$u_b = \omega_p \frac{H_s}{2sinh(kh)} \tag{2.19}$$

with h the local depth and k the local wavenumber from the dispersion relation.

The maximum wave-current shear stress

The maximum combined bottom shear stress within a wave cycle is obtained as

$$\tau_{wc} = ((\bar{\tau}_{wc} + \tau_w \cos\varphi)^2 + (\tau_w \sin\varphi)^2)^{1/2} \tag{2.20}$$

where ϕ is the angle between currents and waves. The wave-averaged, combined wave-current bottom stress $\bar{\tau}_{wc}$ according to *Soulsby* (1995), is found as,

$$\bar{\tau}_{wc} = \tau_c(1 + 1.2(\frac{\tau_w}{\tau_w + \tau_c})^{3.2}) \tag{2.21}$$

Only when the wave orbital velocity $u_b > 0.01$ m/s, the combined effect of waves and currents are taken into account, otherwise only current conditions apply.

2.5 Configuration and set-up

A High-Performance Computing system ARGUS, provided by CESAM, University of Aveiro, was used to run the simulations. Using 48 nodes and 49 gigabytes of memory, a simulation of 14 months with one nested grid took approximately 10 days to complete. Model output was requested every 12 hours and occupied close to 680 GB of space.

A nested grid system with a 1-way configuration was set up to produce a high-resolution simulation for the study area (Figure 2.1). Although initially the hydrodynamic model was tested in a 2-way configuration, the sediment module demonstrated various problems in this mode. The regional grid covered an area between $39°N$ $44.5°N$ of longitude and $-12°W$ $-8°W$ of latitude, with resolution approximately $1/60°$ ($\sim$ 1.38 km). By down-scaling using a factor of 3, the local grid was centred between $41°N$ $43°N$ and $-9.9278°W$ $-8.5389°W$, with resolution approximately $1/180°$ ($\sim$ 0.459 km). The bathymetry grids (Figure 2.1, local grid), were created using data obtained through RAIA observatory[1]. The original data was based on ETOPO1 (*Amante and Eakins*, 2009) with corrections made by the Portuguese and French Hydrographic Offices (HIDROGRAFICO and SHOM). The shoreline was manually adjusted and the minimum depth was set to 5 m.

[1] http://www.marnaraia.org

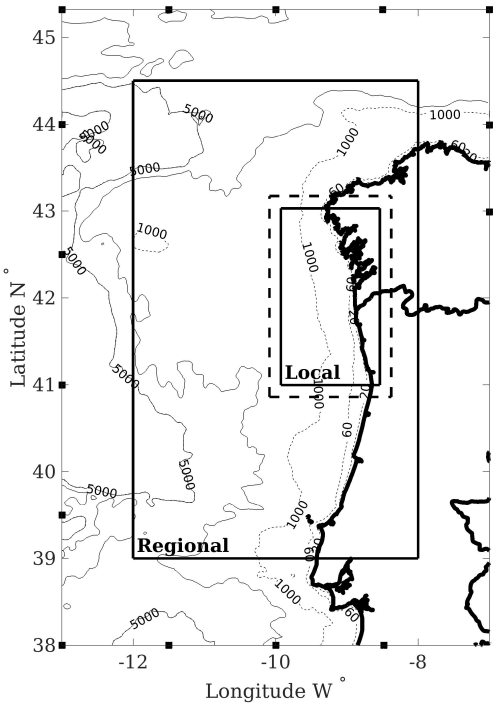

FIGURE 2.1: A nested grid system setup. Black continuous lines represent the CROCO model areas of regional and local grids, respectively. The biggest domain represents the wave model SWAN regional grid area with black squares indicating the location of the inserted wave boundary. The discontinuous black line demonstrates the local grid.

The atmosphere-ocean fluxes were obtained from a WRF simulation of the Iberian region provided by the Meteorology and Climatology Group of the University of Aveiro [2]. The atmospheric model covered a period between 1 June 2008 and 31 December 2009, containing 3 nested domains with resolutions of 27 km, 9 km and 3 km. More information about the performance of WRF simulation on hindcasting the winds and ocean-atmosphere fluxes over this region can be found in *Carvalho et al.* (2012). In the present study, the data from the smallest domain with the highest resolution was used, with a temporal time step of 4 hours.

To use the bulk sub-model, the atmospheric model provided the oceanographic model with net shortwave and downward longwave fluxes, relative humidity, precipitation rate, air temperature and wind velocity.

The climatological-oceanic data was obtained from the Iberia Biscay Ireland - Monitoring and Forecasting Center reanalysis with resolution 1/12°, within the Copernicus Marine Environment Monitoring Service (*Levier et al.*, 2014), to initialize the model and provide information at the boundaries. Daily mean values of temperature, salinity, sea surface

[2] http://climetua.fis.ua.pt

height and current velocities, with a temporal resolution of 2 days, were imposed on the outer boundary of the regional grid.

Measured river discharge and temperature information were provided when available. Rivers introduced to the model, located in the Spanish territory were Eume, Mandeo, Xallas, Tambre, Ulla, Umia, Lérez, Verdugo, and Miñor. River Minho crosses a border between Spain and Portugal and rivers Lima, Cavado, Douro, Vouga, and Mondego in Portuguese territory (Figure 2.2, only the rivers in the local grid are shown). River runoff on the Spanish side was obtained from *Sistema de Información del Anuario de Aforos* MAPAMA. Information for the Portuguese rivers originates from the SNIRH database [3]. Missing data points were replaced with the model SWAT output from MeteoGalicia [4] or available flow data of neighbouring rivers. For rivers, Eume, Verdugo, Cavado, Vouga and Mondego monthly climatologies values were used, while for the rest of the rivers, daily values were used. Inside the estuaries of the rivers mixing between the salty and fresh waters occurs. So, a constant salinity was applied at the mouths of each river in the model surface cell. The values varied depending on the size and configuration of the river estuary.

The wave forcing was obtained from the wave model SWAN, which was run previously, using the same topography grid and atmospheric forcing as described above. The wave model domain was extended out 1° from the western border and 0.5° from the North and South borders for the regional grid and approximately 0.15° for the local grid. This was to guarantee that possible errors generated close to wave model boundaries would not affect the area of interest. The boundary conditions for the largest domain were acquired from ERA5 reanalysis wave data set (*Hersbach et al.*, 2020), with resolution 0.2815°. Black squares in the external rectangle on figure 2.1 represent the 15 points inserted onto the boundary, spaced approximately every 1.5°, except for some corner points. Waves were characterized using five variables varying in space and time: significant wave height of combined wind waves and swell, peak wave period, mean direction of total swell and wave spectral directional width. The initial spectra were computed from the local wind velocities, using the deep-water growth curve of *Kahma and Calkoen* (1992), cut off at values of significant wave height and peak frequency from (*Pierson and Moskowitz*, 1964). The average (over the model area) spatial step size was used as fetch with the local wind. The shape of the spectrum was preserved as the default option of JONSWAP with a $\cos^2$-directional distribution. Timestep of 15 min, directional resolution of 5° and 25 spectral frequency bins logarithmically spaced between 0.0418 Hz and 0.8 Hz were chosen. The first-order upwind scheme BSBT was applied to guarantee numerical stability (*SWAN*, 2013) and Westhuysen whitecapping formulation (*van der Westhuysen et al.*, 2007). Nonlinear wave-wave interactions (triad and quadruplet), wave friction and breaking were also taken into account. The wave model provided information about the amplitude of significant wave height, peak wave period and direction to the hydrodynamic model.

The sediment module has some specific requirements for the hydrodynamic model, to resolve the transport processes. The time steps for the CROCO regional and local grid in

[3] www.snirh.pt

[4] www.meteogalicia.gal

baroclinic mode were set to 150 / 50 s and 3.75 / 1.25 s in barotropic mode, respectively. The model uses Arakawa C-grid terrain-following stretched vertical coordinates, which allows for increased vertical resolution at the surface and bottom, together with uniform grid spacing in between (*Shchepetkin and McWilliams*, 2005). In the current application the number of vertical levels was set to $N = 45$, stretching factor at the surface $\theta_s = 5$ and $\theta_b = 0.6$ to enhance the resolution at the surface and bottom layers. A turbulent closure model K-profile planetary (KPP) boundary layer scheme (*Large et al.*, 1994) parameterizes the unresolved subgrid-scale processes, like mixing in the bottom boundary layer.

The CROCO configuration and set-up are similar to the simulations in *Cordeiro* (2018); *Cordeiro et al.* (2021), which were extensively validated and successfully reproduced the NW Iberian margin dynamics.

2.5.1 Surface sediment distribution

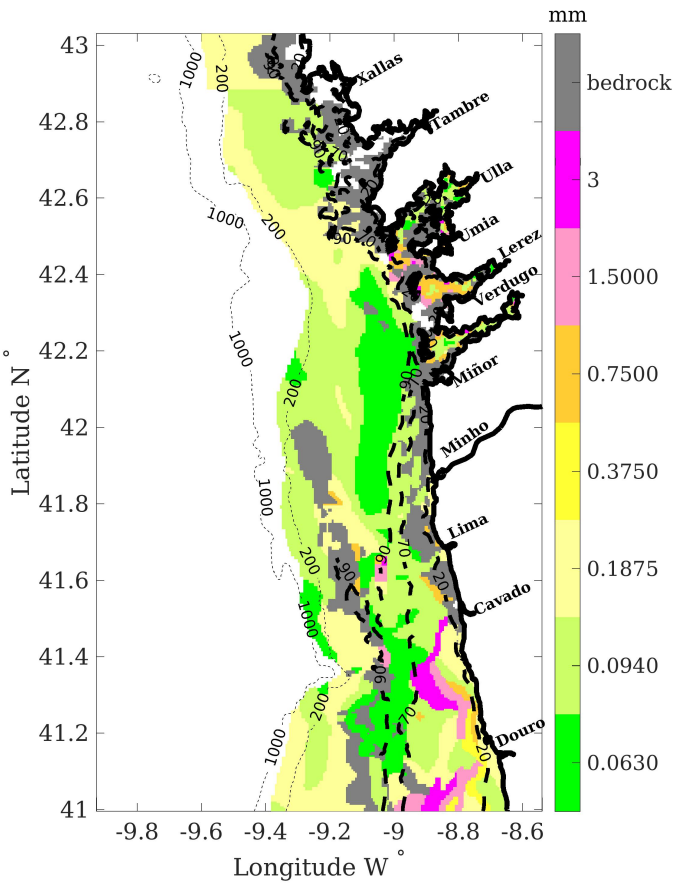

FIGURE 2.2: The seafloor surface sediment map representing the mean grain size on the highest resolution grid for the study area, based on the work of *Dias et al.* (2002b), with additional information inside the Rías from *Vilas et al.* (2005).

The seafloor surface sediment grid for the study area (Figure 2.2), was created based on the median grain size distribution map by *Dias et al.* (2002b). The grid was completed with additional sediment data inside the Rías (Ría de Vigo, Pontevedra and Arousa) derived from *Vilas et al.* (2005). For the regional grid, the surface sediment spatial distribution maps from *López-Jamar et al.* (1992) (figures 2 and 4) and *IH* (2010) were used close to the Northern and Southern boundaries of the study area. All the data was digitized and mapped onto a regular grid with a resolution of 1 km.

The sediments were divided into 8 size classes, each with specific properties (Table 2.1). The total thickness of the sediment bed was set to 6 m and divided into 8 layers, to have an unlimited supply of sediments. The first 5 layers from the top were considered relatively fine, with a thickness of 0.01 m and the rest of the layers were 0.95, 2 and 3 m, respectively.

The critical stress $\tau_{ce,m}$ was calculated as

$$\tau_{ce,m} = 6.4 \times 10^{-7} \rho_0 w_{s,m}^2 \tag{2.22}$$

where ρ_0 density and $w_{s,m}$ is the settling velocity. This stress was modified for silt and very fine sand classes according to *van Rijn* (2007) methodology to incorporate the cohesive effects of fine particles into the model. This was done because with smaller $\tau_{ce,m}$ the finer fraction of sediments was widely dispersed all over the continental shelf. These two sediment size classes represent the fractions of sand in the model, located in areas where in reality sand-silt-clay mixtures can be found according to the *Shepard* (1954) classification of sediments. It is expected that these mixtures also have cohesive properties, therefore altering the characteristics of the sediments. This also explains the wide disperse of the fine fraction sediments in the model with the initial settings and justifies increasing $\tau_{ce,m}$, as it was done by (*Oberle et al.*, 2014) and *Zhang et al.* (2016).

Appendices A presents a detailed overview of the formulations used and coefficients assigned as input, to characterize the seafloor sediments.

TABLE 2.1: Mean grain size classes, represented by the sediment size intervals and corresponding D_{50}. $w_{s,m}$ - settling velocity, E_0 - erosion rate and τ_{ce} - critical shear stress for sediment motion for suspended load.

	interval (mm)	D_{50} (mm)	$w_{s,m}$ (mm/s)	E_0 $(kg/m^2 s)$	τ_{ce} (N/m^2)
1) Silt	< 0.063	0.063	2.487	$6.6\ 10^{-05}$	0.1
2) Very fine sand	0.063-0.125	0.0940	5.464	$1.4\ 10^{-04}$	0.125
3) Fine sand	0.125-0.250	0.1875	19.506	$5.2\ 10^{-04}$	0.24352
4) Medium sand	0.250-0.500	0.3750	51.580	$1.4\ 10^{-03}$	1.7027
5) Coarse sand	0.500-1	0.750	96.294	$2.6\ 10^{-03}$	5.9344
6) Very coarse sand	1-2	1.5000	150.841	$4.0\ 10^{-03}$	14.562
7) Gravel	> 2	3	221.218	$5.9\ 10^{-03}$	31.32
8) Rock - fictive					

2.5.2 Limitations of the model

Ocean dynamics and the interaction with the atmosphere, lithosphere and biosphere are extremely complex and sophisticated. Therefore, using numerical models to study different aspects of its dynamics, demands simplifications and parameterizations, as it is nearly impossible to describe all the processes at once. To better understand and interpret the numerical outcome, it is useful to know all the limitations and physical processes that the modelling system represents.

The CROCO v1.0 regional ocean model is the first stable release, which was launched on 26 June 2018, and is built upon the ROMS AGRIF ocean model (*Shchepetkin and McWilliams*, 2005). During the implementation process, various bugs were encountered and fixed. In addition, some of the applications used in the scope of the present thesis, like realistic wavefield from an offline source and reading sediment bed data from the initial netCDF file, were not fully implemented. Therefore, several improvements were made and the source code of the model had to be modified. The complete list of the modifications in the source code can be seen in the Appendices B. The work done with the code in this thesis consumed a lot of time. At the same time, it allowed a better understanding of the very complex code and interaction with the code developers.

Coupling of models

The coupling between the atmosphere, wave and ocean models is done offline. So, all the models are run separately and the information from each is fed into the hydrodynamic model. *Alves et al.* (2018) concluded that 2-way coupled WRF-ROMS model performance in Iberian summer upwelling conditions has a moderate impact on the model statistics and in many applications, there is no need for fully coupled models.

Warner et al. (2010) tested a fully coupled ocean-atmosphere-wave-sediment transport modelling system and evaluated its performance. They demonstrated how adding waves to the ocean model increased the bottom stress at the sea bed, but on the other hand, also increased the surface roughness and surface mixing of the ocean. This led to cooler SST (Sea Surface Temperature) that reduced wind speed. While the coupled system presented the best results for waves, that were obtained with reduced winds, indicating that the wind-wave growth formulations overestimate the wave growth in strong wind applications. On the other hand, studies where the wave model is coupled offline with an atmospheric model, demonstrate an underestimation of the wave field in high wind conditions (*Silva et al.*, 2015; *Soares et al.*, 2014). Therefore, it is expected that with the current configuration, during storm events, the wave-induced bottom stress is underestimated.

While 2-way coupling improves to some extent the model performances, the know-how and computation time of a fully coupled system come at a cost that does not always justify its use.

Ocean model physics

Wave-current interactions are not taken into account. However, several studies have shown how wave-current interactions can increase the wave height and current speed, depending on the travelling direction of waves and currents (*Bever and Harris*, 2014; *Benetazzo et al.*, 2013; *Warner et al.*, 2010; *Dietrich et al.*, 2010). A preliminary test, with the embedded WKB wave model for monochromatic waves (*Uchiyama et al.*, 2010), indicated the existence of several issues while considering these interactions. Additionally, in CROCO version 1.0, a realistic wavefield from an offline source was not entirely implemented and was completed in the framework of this study. So, the wave-current interaction module together with the waves from an offline source, at this point, is not prepared to work together in this version of CROCO (1.0).

The influence of tides was neglected, as the present application focuses on the shelf area, where the residual currents are weak (*Quaresma and Pichon*, 2013) and not sufficiently strong to resuspend sediments alone (*Oberle et al.*, 2014; *Zhang et al.*, 2016). In application to estuarine systems, the tides should be considered (*Villacieros-Robineau et al.*, 2013).

In the current model implementation, a one-way nesting procedure is considered. This means that the information from the regional grid is passed on to the local one, but not *vice verse*. During the testing period, it was confirmed that there might be some bugs in the model with two-way nesting while the sediment module is activated. On the other hand, the one-way nesting module demonstrated reasonably good results and it was also computationally less time-consuming, reducing the overall model running time.

Sediment transport model

Within the scope of this thesis, all the sediment classes represented were considered non-cohesive. However, the real behaviour of shelf sediments of the finest fractions, located for the most part in the outer shelf areas, is more similar to the combination of silt and clay than to sand. The silt-clay mixture needs more energy to be re-suspended than sand for the same particle size. At the same time, the settling of sand is faster than for silt-clay of the same size. Therefore, as the model considers all the particles as non-cohesive, it would be expected that the re-suspension events started and ended before it was expected in the real scenario with silt-clay characteristics. Nevertheless, the critical shear stresses for the two finest sand classes were altered according to *van Rijn* (2007) methodology to reduce these differences.

Very high sediment concentration in the water column can reduce the settling velocity (*Soulsby*, 1997). This was not taken into account while calculating the settling velocity of each sediment class.

The morphological bed changes and the biogenic contribution in estimating the bedform roughness are not considered. Moreover, the biological activity in the water column was not simulated and the littoral sediment input from rivers was not taken into account initially. However it was considered in Chapter 6, when studying the fate of sediments from the river systems.

Chapter 3

Evaluating wind datasets for wave hindcasting in the NWCIP

This chapter has been published in the Journal of Operational Oceanography in 2020 with the following reference:

Viitak, M., P. Avilez-Valente, A. Bio, L. Bastos, and I. Iglesias (2020), Evaluating wind datasets for wave hindcasting in the NW Iberian peninsula coast,*Journal of Operational Oceanography, Online,* 1–14.

3.1 Introduction

The wave action in coastal zones can generate strong erosion. During extreme events, the combination of wave setup and hazardous wave conditions may result in significant risks to coastal navigation, structures, ecosystems and population. To minimize the risks on a vulnerable coastline, it is necessary to anticipate the storm's impacts and increase coastal resilience. The Intergovernmental Panel on Climate Change (IPCC) depicts a future with an increase in the frequency and strength of the extreme events and larger waves, associated with sea-level rise (*IPCC*, 2014). Monitoring the ocean condition is needed to describe the coastal dynamics. However, they are vast, and thus, the observational data is scattered over large areas (*Bastos et al.*, 2016). Numerical models can fill this gap, being able to represent the complex patterns of coastal dynamics and allowing to set up of an early warning tool to predict the potential effects of storms on coastal environments.

The growing importance of accurate prediction of wave conditions and wave climate requires continuous improvements of the modelling systems. The model's performance depends both on a correct physical formulation and on the quality of the forcing wind data. The accuracy of the wind products can change from one region to another and should be taken into account when choosing the best dataset to force a wave model. *Alvarez et al.* (2014) evaluated different wind products for the Bay of Biscay through comparisons with real data. *Carvalho et al.* (2013) tested QuikSCAT and Cross-Calibrated Multi-Platform (CCMP) project wind datasets for the Iberian Peninsula. QuikSCAT products were also validated for the Ligurian Sea by *Pensieri et al.* (2010), while *Sharp et al.* (2015) assessed the UK CFSR hourly wind speed product using onshore and offshore wind measurements.

Regarding the dataset's efficiency in ocean modelling, *Stopa and Cheung* (2014) carried out a long-term (1980–2010) inter-comparison of wind speed and wave height from ERA-Interim and CFSR in the NE Pacific and NW Atlantic. Both products have good spatial homogeneity, with a consistent level of errors, and show that ERA-Interim generally underestimates and CFSR tends to over-predict the wind speed and wave heights. *Appendini et al.* (2013) assessed the wave modelling performance in the Gulf of Mexico and the Western Caribbean Sea, analysing NCEP/National Centre for Atmospheric Research (NCAR), ERA-Interim and NCEP's North American Regional Reanalysis (NARR) wind products. They found that NCEP/NCAR and ERA-Interim data sets outperform NARR. NARR is more suitable for simulating extreme cyclonic events due to its higher resolution in time and space. However, the capabilities of different wind datasets for wave modelling forecasting in the Iberian Peninsula have so far received little attention.

For this study, the numerical wave model SWAN was selected. It has been successfully applied to several oceans and seas (*Lalbeharry and Ritchie*, 2009; *van der Westhuysen*, 2012; *Alari*, 2013; *Viitak et al.*, 2016), and also to the Iberian Peninsula coast, assessing the performance of its numerical and physical formulations (*Faria*, 2009; *Rusu and Soares*, 2013; *Rusu et al.*, 2015; *Silva et al.*, 2015)

The goal of this work is to implement and validate SWAN v41.10 (*SWAN*, 2016), using six wind data products and applying them to the NW Coast of the Iberian Peninsula. The following questions will be addressed. Which wind dataset leads to the most accurate simulation of wave propagation? How do the spatial and temporal properties of wind data influence wave modelling? How accurate is the SWAN wave model?

3.2 Methods and data

3.2.1 Characterization of the study area

The NWCIP is a complex region in terms of meteo-oceanic conditions (*Bastos et al.*, 2016). It is characterised by a relatively narrow continental shelf (<40 km-wide) and a steep continental slope (>20°). The ocean becomes deeper than 1000 m in just a few tens of kilometres away from the coast (*Gómez-Gesteira et al.*, 2011). The coastal bathymetry presents prominent capes, submarine canyons and promontories that induce hydrodynamic features such as filaments and eddies (*Pinheiro et al.*, 1996; *Peliz et al.*, 2003b; *Lávin et al.*, 2006; *Mason et al.*, 2005; *Relvas et al.*, 2007; *Rossi et al.*, 2013).

The North Atlantic Oscillation mainly mediates the weather conditions in the NWCIP. The Azores High induces northerly and north-westerly (NW) winds over the area that is prevalent throughout the year, with the highest magnitudes in the summer season (*Ramos et al.*, 2011). As a result, dominant NW waves are produced with a mean significant wave height of 2 m and a peak period between 9 and 13 s (*Costa and Esteves*, 2009). During winter, low-pressure systems generated over the Atlantic can cross the NWCIP with associated south-westerly (SW) and south (S) winds, producing extremely high energetic conditions on the continental shelf (*Vitorino et al.*, 2002b). Hs between 3 and 6 m are not

uncommon, reaching between 9 and 12 m during strong storm events (*Dias et al.*, 2002a; *Vitorino et al.*, 2002b,a; *Costa and Esteves*, 2009).

3.2.2 Case study: winter storm events

The time window between 12/2013 and 01/2014 was selected, because, during this period, several storms hit the NWCIP causing extensive damage to infrastructures, such as roads and harbours (*Rusu et al.*, 2015). Between 5-7/01/2014, the passage of the low-pressure system Hercules caused floods in coastal areas, washed away sand dunes and dragged away breakwater concrete armour units, leaving behind considerable damage in harbours, beach structures, roads, sidewalks and promenades. Deposits of sand, mud and debris were moved inland (*Santos et al.*, 2014). During this event, strong SW winds blew over the entire region, producing long-period waves with measured maximum wave heights between 7 and 12 m (Figure 3.1). During the entire analysis period, the mean wave direction was from the N–W sector, with mean Hs between 4 and 5 m, and mean wave period from 7 to 9 s.

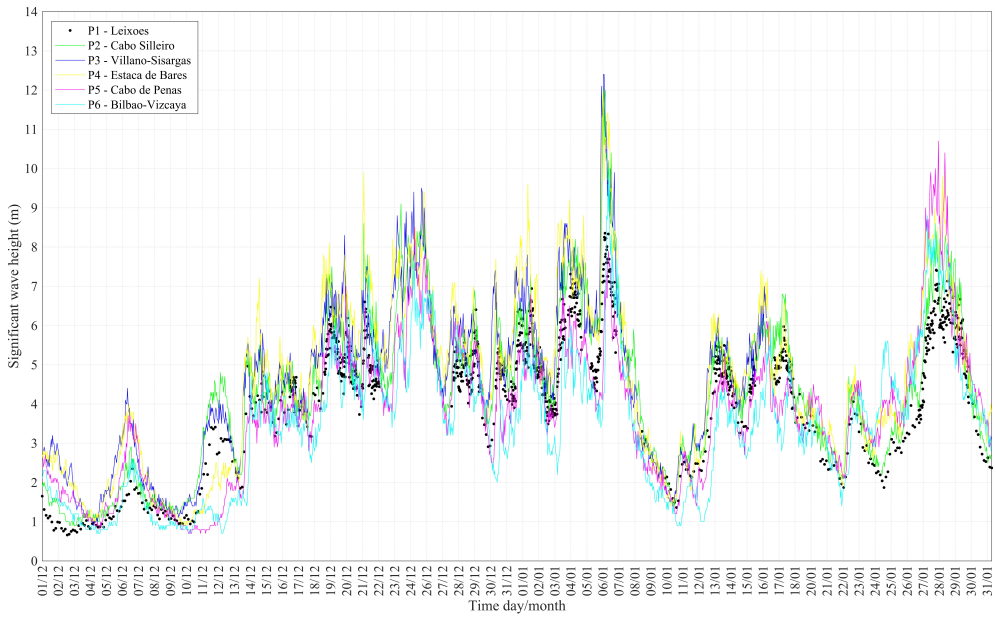

FIGURE 3.1: Hs evolution observed for the 6 buoys during the study period (01/12/2013–31/01/2014).

3.2.3 Wind data products

Surface wind fields were obtained from six databases (Table 3.1), with a reference height of 10 m above the sea level. They were applied in different stages depending on their spatial coverage.

From the ECMWF, the two most recent reanalyses were selected: ERA-Interim (*Dee et al.*, 2011) and ERA5 (*C3S*, 2017) (Copernicus Climate Change Service 2017). ERA-Interim is a global atmosphere reanalysis, continuously updated in real-time with data available since 1979. ERA5 is a recent reanalysis of the EU-funded Copernicus Climate Change Service (C3S) operated by ECMWF. The first segment (2010–2016) provides data at higher spatial and temporal resolution than ERA-Interim.

MERRA-2 (*GMAO*, 2015), the second version of NASA atmospheric reanalysis was constructed using the Goddard Earth Observing System Model V5 with Atmospheric Data Assimilation System.

From the NCEP products, the 6-hourly forecast sur- face winds products from CFSv2 ds094.0 and the hourly time-series from CFSv2 ds094.1 were selected (*Saha et al.*, 2011a,b, 2014).

Finally, historical forecasts from the regional Weather Research and Forecasting model, implemented by MeteoGalicia[1] for local forecast, were considered. This model runs operationally twice a day with three available domains and spatial resolutions. The highest spatial resolution product was selected.

TABLE 3.1: Wind datasets characteristics.

Dataset	$\Delta x \times \Delta y$ (°)	Δy (h)	Availability
ECMWF Era-Interim	0.75 × 0.75	6	1979–2019
ECMWF ERA5	0.2815 × 0.2815	1	2010–present
NASA MERRA-2	0.5 × 0.625	1	1980–present
NCEP CFSv2 (ds094.0)	0.5 × 0.5	1	2011–present
NCEP CFSv2 (ds094.1)	0.5 × 0.5	1	2011–present
WRF-MeteoGalicia	0.1079 × 0.1079	1	2008–present

3.2.4 Observational data

Model results were validated against data from six wave buoys at various depths (Figure 3.2 b)). Leixões (P1) is maintained by the Instituto Hidrográfico[2]. The directional Waverider Datawell is moored in shallow waters (83 m), and records data in a 3-hour interval, increasing the frequency during energetic events (Hs > 5 m). Cabo Silleiro (P2), Villano-Sisargas (P3), Estaca de Bares (P4), Cabo de Peñas (P5) and Bilbao-Vizcaya (P6) are maintained by Puertos del Estado[3], gathering data in a 1-hour interval. They are equipped with a directional Met-Oce sensor and located in relatively deep waters close to the continental shelf border or areas of complex bathymetry and strong depth gradients.

[1] http://www.meteogalicia.gal/
[2] https://www.hidrografico.pt/boias
[3] http://www.puertos. es/

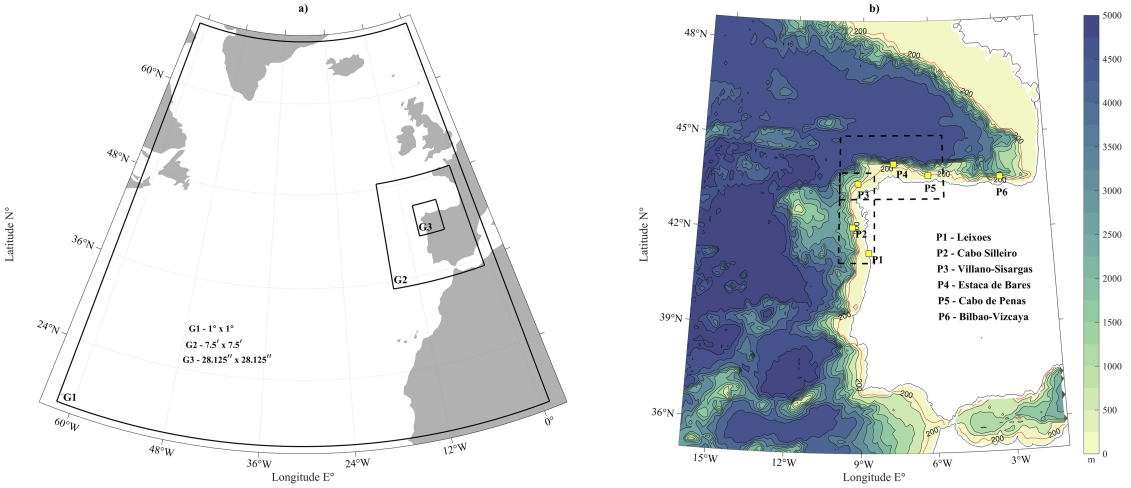

FIGURE 3.2: a) Nesting set-up and computational grids G1, G2 and G3 placements and b) bathymetry of the G2 computational area. The two sectors of the study area are, Atlantic (West) and Cantabrian (North), marked with black intermediate lines and the red isoline indicates the border of the continental shelf. Additionally, the locations of wave buoys are shown with yellow squares.

Due to the resolution of the available bathymetric data and the discrete nature of the computational grids, there is a difference between the computed depth and the real depth at the buoy locations (Table 3.2), especially evident for the coarser grid.

TABLE 3.2: Buoys location and depth (real and interpolated at the numerical grids).

		Location		Depth (m)			
Buoy	Name	Latitude	Longitude	Real	G1	G2	G3
P1	Leixões	41.32 °N	8.98 °W	83	84	82	86
P2	Cabo Silleiro	42.12 °N	9.43 °W	600	2564	702	700
P3	Villano-Sisargas	43.50 °N	9.21 °W	386	Inland	422	482
P4	Estaca de Bares	44.12 °N	7.67 °W	1800	751	1514	1586
P5	Cabo de Peñas	43.75 °N	6.16 °W	615	2393	350	497
P6	Bilbao-Vizcaya	43.64 °N	3.09 °W	870	1789	894	Outside

3.2.5 Numerical model setup

SWAN is a third-generation wave model developed at the Delft University of Technology. Short-crested wind-wave generation and propagation over realistic bathymetry are

described by means of a two-dimensional wave action density spectrum. A spectral wave action balance equation is solved without any a priori restrictions on the spectrum for wave growth evolution (*Booij et al.*, 1999).

A grid nesting procedure was implemented to guarantee proper simulation of nearshore processes. Three computational grids with different spatial extent and resolution were defined (Figure 3.2 a)). The first and coarser grid, G1 (1°x1°), covered the whole North Atlantic to provide swell information for inner computational grids (G2, G3). It lacks detailed information on depth over the continental slope and shelf, thus significantly altering the nearshore wave processes and leading to inaccurate readings at buoy locations. Nevertheless, G1 resolution was enough to accurately represent the long-wavelength low-frequency waves travelling across the ocean. The first nested level or second grid G2 (7.5'×7.5'), covered most of the oceanic area around the Iberian Peninsula. Finally, the second nested level G3 (28.125"×28.125") covered the NW coastal seas of the Iberian Peninsula. The increase in the resolution along with the reduction of the observed area (Figure 3.2 a)) allowed a better agreement between the buoy's real depth and depth on the grid (Table 3.2).

Bathymetric information for G1 was extracted from the GEBCO 30" global grid (*Becker et al.*, 2009). G2 and G3, used information extracted from the West Iberian bathymetry model WIBM2009 (*Quaresma and Pichon*, 2013), which has 1' resolution.

G1 results were compared with observational data from five wave buoys (P1, P2, P4, P5, P6) out of six. P3 was considered a land cell on this grid due to the low resolution, as each cell covered an area of, approximately, 112 × 112 km, causing some inaccuracies in the coastal line representation. G3 covered also five buoys out of six (P1, P2, P3, P4, P5), leaving out the most eastward wave buoy (P6) (cf. Figure 3.2 b)).

In the G1 level all the wind datasets except MeteoGalicia, due to its limited spatial coverage, were used for the wave hindcast. For the next nesting level G2, MeteoGalicia data plus the three G1 best-performing wind data- sets were applied. The boundary conditions for the simulation with MeteoGalicia winds were obtained from the G1 grid run with ERA5 wind data. In the second nesting level G3, the three best-performing wind datasets in G2 were tested.

A spin-up time of 1 week was considered to avoid model inconsistencies. After several tests, spectral directional resolution of 5° and 25 spectral frequency bins logarithmically spaced between 0.0418 and 0.8 Hz were chosen. For G1 and G2, the higher-order numerical S& L scheme and Janssen whitecapping formulation (*Janssen*, 1991) were selected. At G3, the first-order upwind scheme BSBT was applied to guarantee numerical stability (*SWAN*, 2013) and Westhuysen whitecapping (*van der Westhuysen et al.*, 2007) was chosen.

3.2.6 Validation method

To assess the quality of the results, a statistical analysis was performed for three wave parameters: significant wave height (Hs) and the spectrum mean zero-up-crossing wave period (Tm02), calculated from the density spectrum as:

$$Hs = 4\sqrt{E(\omega,\theta)d\omega d\theta} \tag{3.1}$$

$$Tm02 = 2\pi\left(\frac{\omega^2 E(\omega,\theta)d\omega d\theta}{E(\omega,\theta)d\omega d\theta}\right)^{-\frac{1}{2}} = 2\pi\left(\frac{\omega^2 E(\sigma,\theta)d\sigma d\theta}{E(\sigma,\theta)d\sigma d\theta}\right)^{-\frac{1}{2}} \tag{3.2}$$

and, the spectrum peak wave direction (Pdir), which is the peak direction in $E(\theta) = \int E(\omega,\theta)d\omega$, where E is the variance density spectrum, ω the absolute circular frequency determined by the Doppler shifted dispersion and θ the wave propagations direction. Note that Pdir, correspond to the absolute maximum bin of the corresponding discrete wave spectra $E(\theta)$ and hence might not be the real Pdir.

Four statistical parameters, the Root Mean Square Error (RMSE), the Scatter Index (SI), the mean error (BIAS), and the correlation coefficient (Cor) were considered:

$$RMSE = \sqrt{\frac{\sum_{n=1}^{n}(a_i - b_i)^2}{n}} \tag{3.3}$$

$$SI = \frac{RMSE}{\frac{1}{n}\sum_{n=1}^{n} b_i} \times 100 \tag{3.4}$$

$$BIAS = \overline{a_i} - \overline{b_i} \tag{3.5}$$

$$Cor(a,b) = \frac{cov(a,b)}{\sigma_a \sigma_b} \tag{3.6}$$

where a represents the model results, b the observed measurements, n the number of observations, cov(a,b) the covariance between a and b, and σ_a and σ_b the standard deviation of a and b, respectively.

Regarding Pdir, to eliminate any discontinuity between 0° and 360°, the difference between observations θ_{obs} and model results θ_{mod} was obtained (*Pensieri et al.*, 2010). The corrected values were calculated as:

$$\theta_{mod} = \theta_{mod} - 360^\circ \; when \; \theta_{obs} - \theta_{mod} > 180^\circ \tag{3.7}$$

$$\theta_{mod} = \theta_{mod} + 360^\circ \; when \; \theta_{obs} - \theta_{mod} \leqq -180^\circ \tag{3.8}$$

However, due to the proper definition of the statistical parameters, SI was not calculated for Pdir, and the results of this variable were validated using only RMSE.

3.3 Results

3.3.1 Wind datasets performance

Significant wave height (Hs)

The results show a good performance for all the considered wind datasets, with a satisfactory reproduction of the Hs evolution over time. Nevertheless, some differences arise in terms of Hs magnitude. ECMWF products and MERRA-2 were underestimating the highest Hs peaks, while the NOAA-NCEP datasets were largely overestimating them. Both ECMWF products gave similar results, but some improvements can be seen with ERA5 (Figure 3.3a).

The best wind dataset for Hs at G1 was ERA5 (Table 3.3), giving the best results for three considered buoys (P1, P4, P5). In these locations, ERA5, RMSE varies from 0.43–0.71 m, SI from 9.30–17.52%, BIAS from -0.12–0.17 m and Cor from 0.92–0.95. For P2 and P6, the best results are obtained with MERRA-2 and ERA-Interim, respectively.

G2 was forced with the MeteoGalicia WRF dataset and the three best-performing wind datasets in grid G1 ERA-Interim, ERA5 and NCEP CFSv6 (ds094.0). As expected, some improvements can be seen when compared with G1 (Table 3.3). For ERA-Interim, RMSE reduced between 0.02 and 0.03 m at P1 and P4, but presents higher values, up to 0.26 m, for the rest of the buoy's locations. For ERA5, Hs RMSE improves a few centimetres in P1 and P2, but the error increases up to 0.17 m in the rest of the buoys. NCEP CFSv6 (ds094.0) demonstrates better results compared to the G1 level. The Cor coefficient maintains the same values or improves a bit for the G2 domain.

G3 did not show almost any improvement over the previous grid. Comparing the statistical metrics for the three considered domains (G1, G2, G3), G3 outputs present the worst results, even when the MeteoGalicia highest resolution wind dataset was implemented.

Minimal differences between G1 and G2 results were depicted in the estimated values for P2 (Figure 3.3b). Furthermore, the G3 results seem to lead to a higher Hs underestimation. This is further confirmed by the P5 results, where this underestimation was even larger.

The best results for Hs at G1 and G2 were produced using ERA5, for G3 MeteoGalicia.

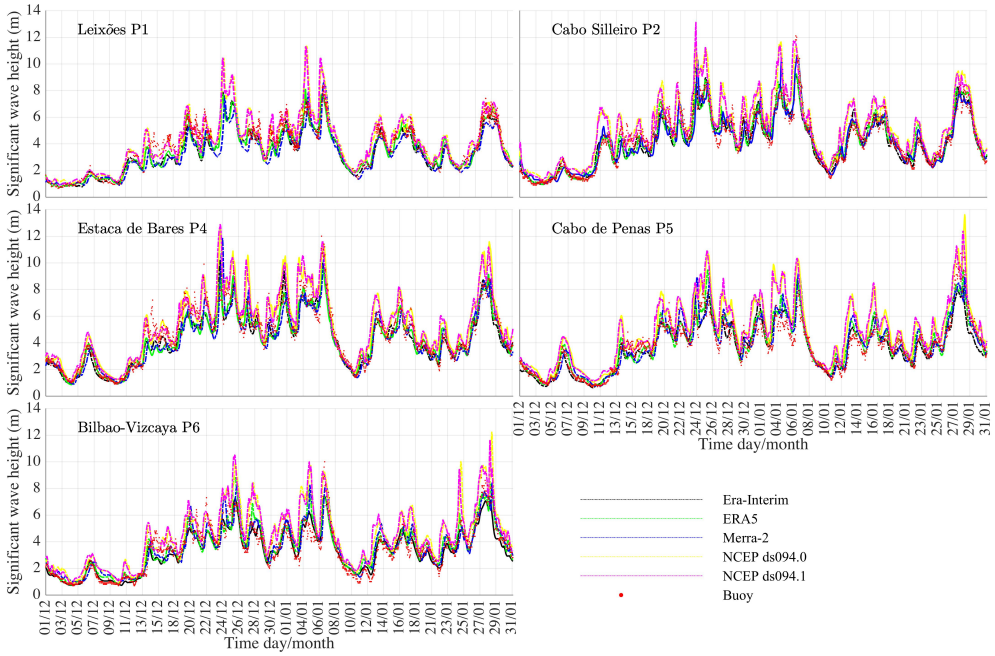

(A) Comparison of measurements and G1 computational grid.

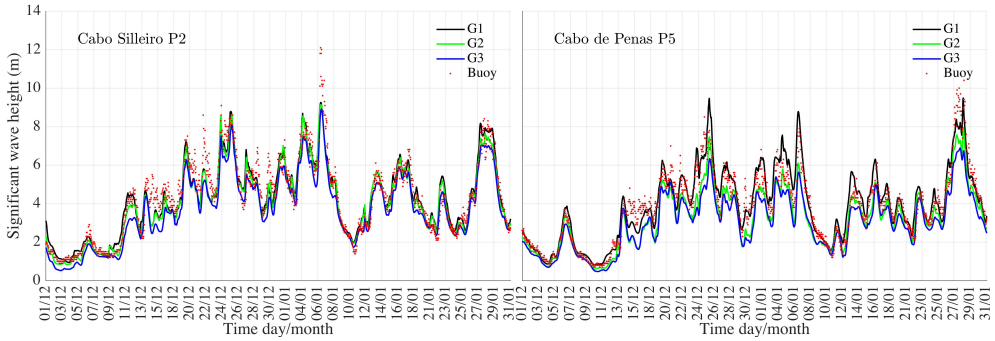

(B) Measured and modelled results with ERA5 wind data, representing all three computational grids in buoy locations P2 and P5.

FIGURE 3.3: Measured and modelled Hs for the period between 01.12.13–31.01.14. Red dots represent buoys measurement, dotted lines are SWAN results for each wind dataset considered. The bold line indicates the best fit for each buoy.

TABLE 3.3: RMSE, SI, BIAS and Cor for each computational domain (G1, G2 and G3) at buoys location for significant wave height. The most optimal dataset for each domain is marked in bold.

	Mean (m)			RMSE (m)			SI (%)			BIAS			Cor		
Hs	G1	G2	G3	G1	G2	G3	G1	G2	G3	G1	G2	G3	G1	G2	G3
P1	4.62														
ERA-Int.	4.17	4.24	4.04	0.47	0.44	4.48	10.12	9.46	10.47	-1.18	-0.15	-0.22	**0.92**	**0.92**	**0.94**
ERA5	**4.30**	**4.36**	**4.12**	**0.43**	**0.40**	**0.45**	**9.30**	**8.74**	**9.76**	**-0.12**	-0.10	**-0.19**	**0.92**	**0.92**	**0.94**
Merra-2	4.09			0.55			11.98			-0.21			0.89		
ds094.0	5.10	5.13		0.62	0.62		13.52	13.45		0.18	0.20		0.89	0.89	
ds094.1	5.08			0.64			13.84			0.18			0.80		
MetGalic		4.50	**4.12**		0.44	0.46		9.57	9.98		**-0.05**	-0.19		0.90	0.93
P2	4.30														
ERA-Int.	4.21	4.02	3.71	0.68	0.71	0.82	15.84	16.39	19.16	-0.10	-0.29	-0.59	0.94	**0.95**	**0.96**
ERA5	4.28	4.08	3.76	0.67	**0.66**	0.81	15.49	**15.26**	18.72	-0.02	-0.22	-0.55	0.94	**0.95**	**0.96**
Merra-2	**4.29**			**0.64**			**14.85**			**-0.01**			**0.95**		
ds094.0	5.22	4.91		1.27	1.03		29.55	24.04		0.92	0.61		0.93	0.94	
ds094.1	5.18			1.33			30.96			0.88			0.90		
MetGalic		**4.21**	**3.77**		0.72	**0.78**		16.67	**18.21**		**-0.09**	**-0.53**		0.94	**0.96**
P3	4.52														
ERA-Int.		**4.53**	4.06		0.63	**0.67**		13.97	14.82		**0.00**	-0.36		0.94	**0.96**
ERA5		4.41	3.99		**0.55**	0.71		**12.25**	15.67		-0.08	-0.41		**0.95**	**0.96**
ds094.0	5.36			1.08			23.77			0.64			0.94		
MetGalic		4.66	**4.07**		0.76	**0.67**		16.73	**14.77**		0.11	**-0.35**		0.93	**0.96**
P4	4.57														
ERA-Int.	4.30	4.32	3.82	0.77	0.75	0.99	16.77	16.43	**21.65**	-0.27	-0.25	**-0.75**	0.94	0.94	**0.96**
ERA5	**4.31**	4.31	3.82	**0.71**	**0.72**	1.01	**15.57**	**15.77**	22.14	**-0.26**	-0.26	**-0.75**	**0.95**	**0.95**	0.95
Merra-2	**4.31**			0.86			18.82			-0.25			0.92		
ds094.0	5.31	5.24		1.14	1.09		24.85	23.96		0.74	0.67		0.94	0.94	
ds094.1	5.29			1.20			26.15			0.72			0.93		
MetGalic		**4.60**	**3.95**		0.90	**0.91**		19.66	19.82		**0.03**	-0.62		0.92	**0.95**
P5	3.79														
ERA-Int.	**3.77**	3.10	2.94	0.71	0.93	1.07	18.68	24.57	28.17	-0.03	-0.70	-0.86	0.92	**0.95**	**0.95**
ERA5	3.96	3.24	3.02	**0.66**	0.83	1.01	**17.52**	22.00	26.60	0.17	-0.56	-0.77	**0.94**	0.94	**0.95**
Merra-2	3.95			0.74			19.38			**0.15**			0.93		
ds094.0	4.86	**3.86**		1.43	**0.64**		37.60	**16.86**		1.07	**0.06**		0.93	**0.94**	
ds094.1	4.89			1.51			39.72			1.09			0.91		
MetGalic		**3.72**	**3.22**		0.83	**0.81**		21.88	**21.40**		-0.07	**-0.57**		0.91	**0.95**
P6	3.46														
ERA-Int.	3.32	2.83		**0.64**	0.90		**18.39**	26.04		-0.14	-0.63		**0.94**	**0.95**	
ERA5	**3.58**	3.17		0.72	**0.77**		20.74	**22.33**		**0.12**	-0.29		0.92	0.92	
Merra-2	3.63			0.72			20.92			0.17			0.92		
ds094.0	4.41	3.79		1.33	0.78		38.49	22.45		0.96	0.33		0.91	0.92	
ds094.1	4.45			1.43			41.46			1.00			0.88		
MetGalic		**3.35**			0.81			23.38			**-0.11**			0.89	

Mean wave period (Tm02)

Tm02 was reasonably well represented whatever the wind dataset used at the G1 grid. Nevertheless, ERA-Interim, ERA5 and MERRA-2 lead to an underestimation of the Tm02 at all the buoy locations, whereas it was overestimated at some locations for both NOAA datasets.

For the first two weeks (01/12–13/12), the mean period was largely underestimated for all the datasets with the exception of buoy P4, where SWAN results were closer to measured values than at any other considered buoy (Figure 3.4a). The correlation results reveal a better performance of the wind datasets in the Cantabrian sector, with Cor between 0.77 and 0.86. In the West Atlantic sector, Cor was lower, between 0.71 and 0.79. When compared with Hs Cor values, a decrease in the correlation of 17% in the West Atlantic sector and 11% in the Cantabrian sector was noticed (Table 3.3 and 3.4).

Nevertheless, and contrary to the Hs results, Tm02 for G2 presents a slightly poorer outcome at all buoys but P1, being quite improved for G3. G3 shows the best results from the three considered computational grids. RMSE for Tm02 was close to or over 1.50 s for most buoys and wind datasets for G1 and G2, while for G3 it remains below 1.0 s for ERA5 and close to 1.0 s for all the other wind datasets (Table 3.4).

For the two initial simulation weeks, G1 and G2 solutions do not accurately represent Tm02 evolution. Such a pattern was corrected for the highest resolution simulation on grid G3. At P1, and after the first two weeks within the simulation, it seems that for G1 and G2, the wave energy was more spread along the frequency bins, nevertheless, the lower frequency bins were under-represented in G3. At P5, G3 results clearly show a much better performance, with a good capture of Tm02, which might indicate a better representation of the wave energy along the different frequency bins (Figure 3.4b). The best results for Tm02 at G1 and G2 were produced using NOAA NCEP ds094.0. For the three wind datasets selected for forcing the waves on G3, ERA5 led to the best results for Tm02.

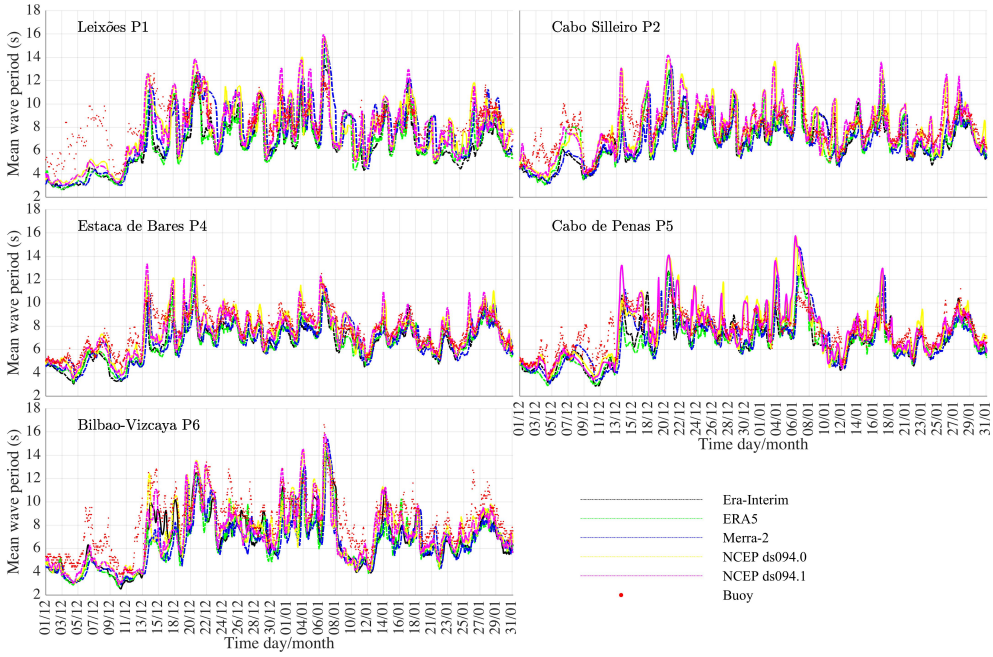

(A) Comparison of measurements and G1 computational grid.

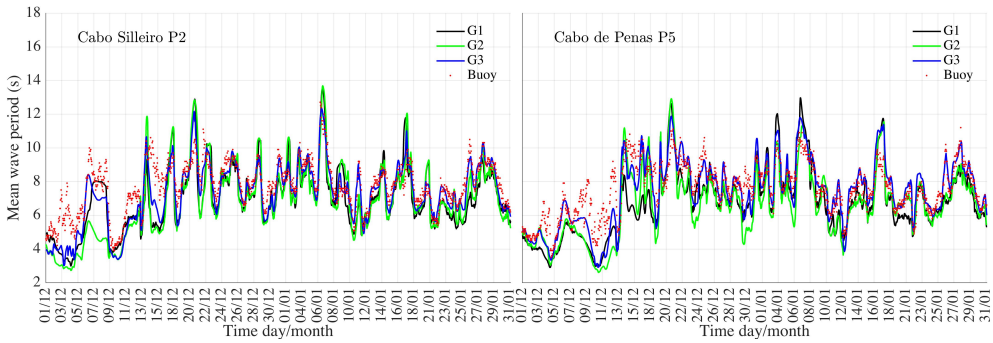

(B) Measured and modelled results with ERA5 wind data representing all three computational grids, in buoy locations P2 and P5.

FIGURE 3.4: Measured and modelled Tm02 for the period between 01.12.13 – 31.01.14. Red dots represent buoys measurement, dotted lines are SWAN results for each wind dataset considered. The bold line indicates the best fit for each buoy.

TABLE 3.4: RMSE, SI, BIAS and Cor for each computational domain (G1, G2 and G3) at buoys location for mean wave period. The most optimal dataset for each domain is marked in bold.

	Mean (m)			RMSE (m)			SI (%)			BIAS			Cor		
Tm02	G1	G2	G3	G1	G2	G3	G1	G2	G3	G1	G2	G3	G1	G2	G3
P1	8.94														
ERA-Int.	7.62	7.86	7.90	1.24	1.13	0.85	13.85	12.56	9.55	-0.51	-0.42	-0.40	0.75	0.76	0.84
ERA5	7.66	7.86	**7.95**	1.25	1.14	**0.82**	13.96	12.77	**9.13**	-0.49	-0.42	**-0.38**	0.76	0.76	**0.86**
Merra-2	8.46			1.14			12.71			-0.19			0.71		
ds094.0	8.87	**9.16**		**1.02**	**0.89**		**11.43**	**9.96**		**-0.03**	**0.09**		**0.79**	**0.82**	
ds094.1	**8.95**			1.10			12.31			0.00			**0.79**		
MetGalic		7.61	7.72		1.27	0.95		14.24	10.61		-0.52	-0.47		0.72	0.84
P2	7.73														
ERA-Int.	6.95	6.85	7.23	1.59	1.68	1.04	20.52	21.68	13.40	-0.78	-0.88	-0.51	0.71	0.74	0.87
ERA5	6.94	6.81	**7.27**	**1.43**	1.65	**0.94**	18.47	21.36	**12.19**	-0.79	-0.93	**-0.46**	0.77	0.76	**0.89**
Merra-2	6.94			1.58			20.45			-0.79			0.72		
ds094.0	**7.86**	**7.85**		**1.43**	**1.53**		**18.46**	**19.82**		**0.12**	**0.12**		**0.78**	**0.79**	
ds094.1	7.93			1.50			19.46			0.20			0.76		
MetGalic		6.78	7.20		1.71	1.02		22.11	13.21		-0.95	-0.53		0.71	0.87
P3	7.65														
ERA-Int.		6.75	7.11		1.2	0.80		15.72	10.48		-0.68	-0.41		0.81	0.90
ERA5		6.86	**7.19**		**1.17**	**0.75**		15.29	**9.78**		-0.6	**-0.35**		0.81	**0.91**
ds094.0		**7.69**			**1.17**			**15.27**			**0.03**			**0.8**	
MetGalic		6.78	7.12		1.26	0.81		16.48	10.58		-0.66	-0.40		0.77	0.90
P4	7.60														
ERA-Int.	6.61	6.59	7.05	1.32	1.42	0.94	17.42	18.75	12.38	-0.99	-1.01	-0.55	0.85	0.81	0.90
ERA5	6.67	6.62	**7.10**	1.26	1.36	**0.87**	16.55	17.95	**11.46**	-0.93	-0.97	**-0.50**	0.85	0.83	**0.91**
Merra-2	6.76			1.24			16.30			-0.84			0.83		
ds094.0	7.44	**7.34**		**0.95**	**1.14**		**12.53**	**14.97**		**-0.15**	**-0.26**		**0.86**	**0.84**	
ds094.1	**7.42**			1.03			13.50			-0.18			0.84		
MetGalic		6.53	6.97		1.44	0.97		18.87	12.77		-1.06	-0.63		0.81	0.90
P5	7.56														
ERA-Int.	6.82	6.46	7.38	**1.40**	1.8	1.12	18.52	23.81	14.83	-0.73	-1.1	-0.17	0.80	0.69	0.82
ERA5	6.69	6.62	**7.43**	1.49	1.51	**0.96**	19.66	19.93	**12.70**	-0.86	-0.94	**-0.12**	0.78	0.8	**0.87**
Merra-2	6.92			1.41			18.64			-0.63			**0.81**		
ds094.0	**7.59**	**7.21**		**1.40**	**1.35**		**18.53**	**17.9**		**0.03**	**-0.34**		**0.81**	**0.81**	
ds094.1	7.61			1.54			20.32			0.06			0.78		
MetGalic		5.95	6.75		1.97	1.24		16.12	16.39		-1.61	-0.81		0.72	0.84
P6	8.31														
ERA-Int.	**8.31**	**7.01**		1.98	**1.9**		23.88	**22.89**		-1.56	**-1.3**		**0.86**	**0.83**	
ERA5	6.50	6.07		2.24	2.69		26.99	32.32		-1.81	-2.25		0.82	0.76	
Merra-2	6.47			2.37			28.51			-1.84			0.77		
ds094.0	7.20	6.69		1.89	2.31		22.73	27.85		**-1.11**	-1.62		0.80	0.73	
ds094.1	7.20			**1.81**			**21.73**			**-1.11**			0.83		
MetGalic		5.83			2.93			35.3			-2.48			0.72	

Peak direction (Pdir)

For Pdir, the best G1 results were obtained with NCEP ds09.1, MERRA-2 and Era-Interim (Figure 3.5). The best statistical parameters were obtained at P1, where NCEP ds09.1 and MERRA-2 provided similar outcomes. For both datasets, RMSE was 10° and Cor was 0.92. For the other buoys, the RMSE was mostly close to 30° reaching up to 39°, with the exception of the ERA-Interim results at P6 where RMSE of 19° was obtained. All the wind datasets clearly display a bias in the peak wave direction, with a tendency for an anti-clockwise error in the estimated wave direction (Table 3.5).

Similar to Tm02, the numerical model seems to be less accurate in estimating Pdir for all the buoys locations for the initial two weeks period.

For G2, the best wind datasets were NCEP CFSv2 (ds094.0) for P1 and P3 and Era-Interim for P2, P4, P5 and P6. For G3, the best dataset was ERA-Interim, although the Atlantic sector results present small differences (from 1° up to 4°) between the considered datasets. In the Cantabrian sector, larger differences arise, reaching up to 13° at P1.

There existed a small but consistent improvement in almost each buoy location for all the wind datasets when G1 and G3 results were compared.

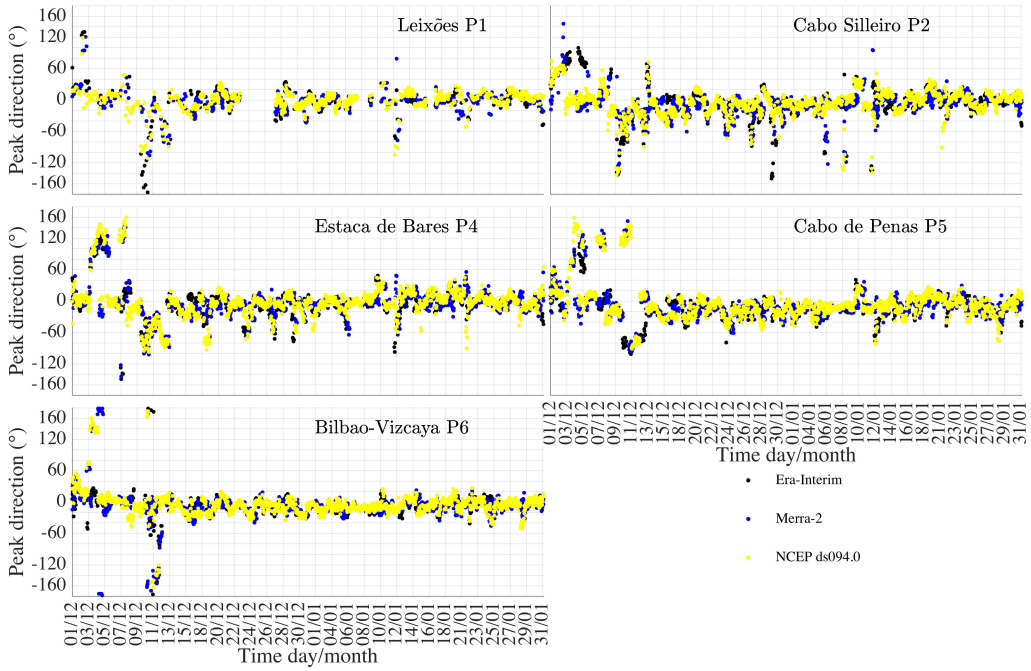

FIGURE 3.5: Difference between buoys and model outcome (G1) with three wind datasets, ERA-Interim, Merra-2 and NCEP ds094.0.

TABLE 3.5: RMSE, SI, BIAS and Cor for each computational domain at buoys location for peak direction. The most optimal dataset for each domain is marked in bold.

	Mean (m)			RMSE (m)			BIAS			Cor		
Pdir	G1	G2	G3	G1	G2	G3	G1	G2	G3	G1	G2	G3
P1	322											
ERA-Int.	**322**	**326**	**325**	12	**9**	10	0.21	**1.43**	1.31	0.88	0.94	0.93
ERA5	324	327	326	15	11	**9**	4.64	2.06	1.52	0.84	0.91	**0.94**
Merra-2	323			**10**			0.44			**0.92**		
ds094.0	**322**	**326**		**10**	**9**		**0.02**	1.79		**0.92**	**0.95**	
ds094.1	322			11			0.19			0.90		
MetGalic		329	**325**		17	10		2.81	**1.08**		0.83	0.93
P2	297											
ERA-Int.	**302**	**304**	**303**	31	**24**	**20**	5.16	**7.34**	**5.68**	0.91	**0.95**	**0.97**
ERA5	304	306	304	33	27	22	7.51	9.12	6.68	0.91	0.94	0.96
Merra-2	305			**26**			**7.95**			**0.94**		
ds094.0	303	306		27	27		6.46	9.06		0.94	**0.95**	
ds094.1	**302**			29			4.88			0.93		
MetGalic		313	305		42	24		16	7.69		0.89	0.95
P3	293											
ERA-Int.		**298**	**296**		29	**25**		**3.94**	**1.82**		0.94	**0.95**
ERA5		301	298		30	**25**		5.73	3.25		0.94	0.95
ds094.0		300			**27**			4.77			**0.85**	
MetGalic		303	**296**		37	27		7.5	1.85		0.91	0.94
P4	313											
ERA-Int.	318	317	317	31	**29**	**25**	4.84	4.35	3.62	**0.89**	**0.9**	**0.92**
ERA5	317	**313**	315	33	37	27	3.84	-0.59	2.01	0.88	0.86	0.91
Merra-2	317			31			3.80			**0.89**		
ds094.0	**316**	**313**		35	35		**2.45**	**-0.26**		0.86	0.86	
ds094.1	317			**30**			4.29			**0.89**		
MetGalic		318	**314**		40	34		4.82	**1.09**		0.83	0.87
P5	316											
ERA-Int.	328	**317**	320	**29**	**29**	**25**	11.74	**0.66**	3.62	**0.63**	**0.53**	**0.61**
ERA5	321	312	**317**	35	34	31	5.57	-4.18	0.81	0.54	0.46	0.49
Merra-2	324			32			8.13			0.60		
ds094.0	**320**	311		37	31		**4.21**	-4.87		0.52	0.5	
ds094.1	**320**			39			4.39			0.51		
MetGalic		315	315		38	37		-1.14	**-0.68**		0.43	0.43
P6	320											
ERA-Int.	327	**321**		**19**	**18**		6.87	**0.92**		**0.85**	**0.83**	
ERA5	**325**	**318**		29	30		4.91	-2.68		0.75	0.71	
Merra-2	326			33			5.43			0.69		
ds094.0	**325**	**318**		29	25		**4.09**	-2.64		0.74	0.75	
ds094.1	326			31			5.80			0.71		
MetGalic		323			34			2.57			0.69	

3.4 Discussion

The presented results revealed minor differences in model solutions when using different wind datasets. Nevertheless, for each considered wave parameter, the best ones can be clearly distinguished. ERA5 gives the best results for Hs, Era-Interim for Pdir and NCEP CFSv2 (ds094.0) for Tm02, although the difference between NCEP CFSv2 (ds094.0) and ERA5 was relatively small and both can be considered to properly simulate mean wave period (Table 3.4).

The temporal and spatial characteristics of the wind datasets did not have a big influence on the results. The best Pdir results were obtained with Era-Interim, which was the lower temporal and spatial resolution database (Table 3.1). Therefore, to simulate the approaching swell, coarse grids and larger time steps with a proper representation of wind speed and direction, seem to be appropriate to produce accurate solutions.

The different responses observed for the wave parameters in G3 could be related to the wave spectrum. When calculating the wave variables, different parts of the wave energy spectra are considered. Hs is calculated taking into account the total wave energy, whereas the rest of the parameters are found through circular frequency or direction. Errors in the

velocity and direction fields of the wind could be transferred to the wave model and may produce inaccurate frequencies transference to the surface waters. This seems not to have such a big effect on the total energy but rather affects the individual components.

Alvarez et al. (2014) concluded that coarser databases are less reliable in near-shore areas. Additionally, they noted that the wind speed and direction are less accurate for low wind speed events ($< 4m/s$). In wave modelling it is not possible to determine which waves are induced with low wind speed, so another approach was considered. Calm and storm periods were analysed separately considering a 5 m wave height threshold. The results obtained at P1 and P5 with ERA5 for all three modelling levels revealed that the more accurate Hs results were obtained mostly during calm conditions (Table 3.6). Tm02 and Pdir were better represented during storms. This confirms that, with lower wind speed, the wave simulations are less accurate and the total energy spectre of the waves is less affected by the individual parts.

Our model configuration was reliable when compared with similar studies, presenting results with the same level of accuracy, or better than previously developed works (Table 3.7). This comparison is not straightforward due to differences such as the geographical area, the grid's resolution, the location of the buoys, the type of wind data, etc. Nevertheless, it provides an indication of the type of accuracy and credibility of the wave model set- up that was implemented in this study.

TABLE 3.6: RMSE, SI, BIAS and Cor for each computational domain (G1, G2 and G3) at P1 and P5 in a storm and calm situation using ERA5 wind fields.

		Hs				Tm02				Pdir			
		P1		P5		P1		P5		P1		P5	
		storm	calm	storm	calm	storm	calm	storm	calm	storm	calm	storm	calm
G1	RMSE	0.33	0.28	0.43	0.51	0.74	1.01	0.60	1.36	7	13	12	33
	SI	5.50	7.55	6.99	16.54	7.48	12.13	6.81	18.98	2.22	4.12	3.87	10.49
	BIAS	-0.07	-0.06	0.04	0.13	-0.16	-0.34	-0.08	-0.78	0.04	0.88	4.62	0.96
	Cor	0.72	0.90	0.73	0.91	0.72	0.70	0.67	0.73	0.65	0.87	0.45	0.56
	Med. s	5.49	3.47	6.35	3.22	8.85	6.83	8.49	6.13				
	Med. m	5.91	3.72	6.17	3.06	9.84	8.31	8.85	7.16	329	317	315	316
G2	RMSE	0.30	0.27	0.59	0.59	0.64	0.94	0.63	1.37	5.05	10.17	7.48	32.86
	SI	5.11	7.22	9.52	19.38	6.52	11.36	7.09	19.14	1.54	3.21	2.37	10.40
	BIAS	-0.06	-0.04	-0.24	-0.32	-0.12	-0.29	-0.17	-0.77	0.58	1.48	2.25	-6.44
	Cor	0.73	0.91	0.82	0.90	0.71	0.71	0.70	0.76	0.69	0.93	0.57	0.48
	Med. s	5.54	3.52	5.17	2.64	9.05	7.02	8.13	6.15				
	Med. m	5.91	3.72	6.17	3.06	9.64	8.31	8.85	7.16	329	317	315	316
G3	RMSE	0.34	0.30	0.75	0.67	0.47	0.67	0.36	0.89	2.81	8.49	8.66	29.51
	SI	5.74	7.99	12.21	21.96	4.73	8.06	4.03	12.44	0.86	2.68	2.75	9.34
	BIAS	-0.11	-0.09	-0.33	-0.45	-0.15	-0.23	0.04	-0.16	0.42	1.09	3.13	-2.32
	Cor	0.78	0.92	0.81	0.92	0.82	0.81	0.84	0.84	0.84	0.95	0.59	0.51
	Med. s	5.24	3.34	4.79	2.47	8.90	7.29	9.00	6.95				
	Med. m	5.91	3.72	6.17	3.06	9.84	8.31	8.85	7.16	329	317	315	316

TABLE 3.7: Validation results of wave mode SWAN from various studies around the world.

Author	*Rusu et al.* (2015)	*Rusu and Soares* (2013)	*Silva et al.* (2015)	*Viitak et al.* (2016)	This study
Area	West Iber. co.	Cont. Portugal	Spanish co.	Baltic Sea	NW Iber. co.
Wind	HIPOCAS	MM5	ERA-Interim	HIRLAM	ERA5
Hs					
RMSE	0.74	0.40	0.81	0.28	0.45
SI	0.17	0.19	0.42	0.22	0.10
BIAS	0.23	0.12	0.36	0.19	-0.19
Cor	0.9	0.95	0.83	0.95	0.94
Tm02					
RMSE	0.99	1.11	1.83	-	0.82
SI	0.11	0.15	0.31	-	0.09
BIAS	0.25	-0.69	-0.37	-	-0.38
Cor	0.82	0.86	0.68	-	0.86

3.5 Conclusion

All the wind datasets selected for this study were able to depict quite well the evolution of the wave fields. The differences arise when analysing the wave parameters. The obtained results allow us to distinguish the most optimal dataset for each wave characteristic. Hs was well represented with ERA5, Tm02 with NCEP CFSv2 (ds094.0) or ERA5, and Pdir with Era-Interim. Overall, the ECMWF datasets seem to produce the most reliable outcome for the region under study, particularly for Hs and Tm02, with a slight improvement when using ERA5. This should be taken into account for future wave modelling studies.

The spatio-temporal resolution of the wind datasets does not have as big impact on wave modelling as the accuracy of the wind speed and direction. The errors in wind datasets were most likely transferred to waves, contributing to the wave model solutions' inaccuracy. It was noted that, with lower wind speed values, the results of wave modelling were not as accurate as with higher wind speed values.

The method applied to simulate NWCIP waves with SWAN was generally reliable and comparable to other similar studies. The model succeeds to predict extreme wave conditions with relatively good accuracy, depicting the wave field development during storm events. The best results were obtained for Hs, being more challenging to accurately represent Tm02 and Pdir.

The obtained results depicted the performance of a numerical wave model considering different wind data-sets. Model inaccuracies were pointed out, as well as the best wind databases for each considered parameter, providing valuable information to produce the best numerical solutions and properly predict the effects of extreme events on a vulnerable seaboard, helping to mitigate the associated risks for ecosystems and populations.

Chapter 4

Validation of the models

4.1 Introduction

The configuration and set-up of modelling systems involve sensitivity tests, using different prediction methods, and understanding the context and problems at hand. At the same time, taking into account the limitations of the models and observational data. The configurations of the hydrodynamic model CROCO, wave model SWAN and sediment model presented in Chapter 2, are based on the validation results presented in this chapter.

In the current application, special attention was put into the validation of the modelling system to most adequately represent the waves and circulation on the shelf. Even the most advanced models to date can only predict sediment transport within a factor of two at best and higher uncertainties are common. This is due to the power dependence of sediment-transport rates on the flow velocities, which for the bed load is at a power of three and for the suspended load even higher. Therefore, any small errors in the hydrodynamics create strong amplifications in the sediment-transport (*Amoudry and Souza*, 2011).

The sediment transport processes are complex, involving continuous interactions between the flow of water and the seabed in different time scales, from a few seconds to hundreds of years and cover space scales, from a few mm to mesoscale. Therefore, there is a need for generalization and a location-specific approach. In many cases, the site-specific calibration and the quality of dynamical forcing determine how successfully the numerical models resolve the sediment dynamics. This is because sediment transport depends on many complicated and interactive processes, of which several these are not completely understood and in many cases not even measured, for example, biological effects (*Soulsby*, 1997). Consequently, the available observational data usually provides a partial description of the three-dimensional sediment-transport process, presenting a big challenge for the validation of the 3D modelling systems.

Most commonly, the uncertainties in the sediment transport modelling arise from the use of empirical expressions, for example in the turbulence closure schemes and bedforms. In addition, heavy dependence on different coefficients that can exhibit a large variability, e.g. erodibility constant, and settling velocity of sediments. Often, the continuous sediment size distribution is represented by a series of discrete values. In many cases, some of the processes are neglected altogether such as mixed beds or cohesive effects of sediments

(*Amoudry and Souza*, 2011). Calibrating the formulas and coefficients for site-specific use helps to improve considerably the margin of error.

A similar approach has been used by other authors to study the sediment transport processes. For instance *Blaas et al.* (2007) concentrated on the Southern Californian shelves and *Warner et al.* (2008) presented a detailed overview of the sediment model functionalities, results of sensitivity tests and a realistic application in Massachusetts Bay. *Karakaş et al.* (2006); *Fischer et al.* (2007) and *Fischer and Karakaş* (2009) studied the sediment movement and particle advection across the NW African shelf. All of the above-referred models used an earlier version of the CROCO model. Only a handful of numerical studies have been performed considering NW Iberian shelf as the study site while using 3D models (*Zhang et al.*, 2016, 2019). Therefore, the present study contributes to advancing the understanding of different sediment transport processes in this area. As well, further validates and improves the knowledge about the CROCO modelling system's efficiency and applicability in different locations around the world.

The following chapter focuses on evaluating the performance of the modelling system configuration presented in Chapter 2.

4.2 Methods and data

4.2.1 Modelling system

The numerical models and their configurations described in Chapter 2 were specifically developed to model the sediment transport in the NW Iberian Peninsula. A simulation from November 2008 to December 2009 was performed, covering an annual cycle and two distinct winters. The chosen period enabled to simulate the movement of sandy sediments on the shelf in terms of intra-annual changes, during all four seasons, and study the impact of some specific events like downwelling or upwelling, and different storm responses. It should be noted, that in the current simulation, the sediments available for transport originated only from the seabed. No external source of sediments was available, i.e. from the rivers.

Both the wave and ocean models had a necessary spin-up time that allowed them to stabilize. Thereafter, one by one, each module in the CROCO model was activated. Firstly, atmospheric forcing was added, then a realistic wave field was considered, next the sediments and finally river discharge, allowing us to analyze and understand the role of each of the forcing terms.

4.2.2 Statistical analysis

To evaluate the performance of the numerical models, a variety of statistical metrics were calculated for different variables. When possible, the quality of the wave and ocean models and sediment modules were assessed based on five statistical parameters.

The mean, denoted with an over-bar, of model estimates a or observations b, were obtained by the sum of respective values divided by n, the number of values :

$$\overline{a} = \frac{\sum_{i=1}^{n} a_i}{n} \tag{4.1}$$

The correlation coefficient, RMSE and BIAS were estimated as

$$Cor(a,b) = \frac{cov(a,b)}{\sigma_a \sigma_b} \tag{4.2}$$

$$RMSE = \sqrt{\frac{\sum_{i=1}^{n}(a_i - b_i)^2}{n}} \tag{4.3}$$

$$BIAS = \overline{a} - \overline{b} \tag{4.4}$$

where $cov(a,b)$ is the covariance between a and b, σ_a and σ_b the standard deviation of a and b, respectively. Finally, based on *Willmott* (1981) metric a model skill was calculated,

$$S_W = 1 - \frac{\sum_{i=1}^{n}|a_i - b_i|^2}{\sum_{n=1}^{n}(|a_i - \overline{a}| + |b_i - \overline{b}|)^2} \tag{4.5}$$

where skill score one indicates a perfect agreement between the model and observations. As the model diverges from the observations the skill approaches zero.

4.2.3 Observational data

For almost 18 months, from November 2008 to April 2010, an upward-looking SonTek 500 Acoustic Doppler Current Profiler (hereafter ADCP) was moored at 75 m depth close to Cabo Silleiro (white circle in Figure 4.1, $42.083°N$ and $-8.933°W$), recording every 5 minutes with a vertical resolution of 3 m (*Barton et al.*, 2019a). The ADCP allowed retrieving information about the current velocities along the water column, temperature 2 meters above the bed (mab) and backscatter signal. The ADCP has the highest sensitivity for particles with a radius of 480 μm. For larger particles, the sensitivity is inversely proportional to particle radius. The minimum detectable radius was 25 μm (*SonTek.Inc*, 1997). During the same period, an automated Technicap PPS 4/3 sediment trap was deployed at 35 m of water depth at the base of the photic zone in an additional mooring line (*Zúñiga and Castro*, 2019). The sediment trap data was used to determine gravimetrically the total mass fluxes. A detailed explanation of the sediment trap sampling strategy and processing can be found in *Zúñiga et al.* (2016). Monthly hydrographic surveys were conducted along a $42.08°N$ across-shelf section, in 7 equally spaced stations from 75 m ($-8.93°W$) to 580 m ($-9.44°W$) depth, during the same period (Figure 4.1) (*Barton et al.*, 2019b; *Castro et al.*, 2020a,b). The duration of the cruise was approximately 4 hours starting between 08:00 and 11:00 and ending at the deepest station between 12:00 and 15:00. Using a CTD - Seabird 25 equipped with additional sensors, profiles of salinity,

temperature, fluorescence and turbidity were obtained among other parameters. More detailed information about the field measurements and backscatter data corrections can be found in the article of *Villacieros-Robineau et al.* (2019).

The wave information was obtained from two different wave buoys, located on the shelf at various depths. Wave buoy Leixões ($41.32°N$, $-8.98°W$) is located at 83 m depth on the coast of Portugal and maintained by the Instituto Hidrografico [1]. The information is gathered in 3-hour intervals and increased in frequency when significant wave height reaches over 5 m. Cabo Silleiro wave buoy ($42.12°N$, $-9.43°W$), is found on the coast of Galicia at a depth of 600 m, belonging to Puertos del Estado [2], recording data at every hour. All the wave buoys are represented with white stars in Figure 4.1.

[1] https://www.hidrografico.pt/
[2] https://www.puertos.es/

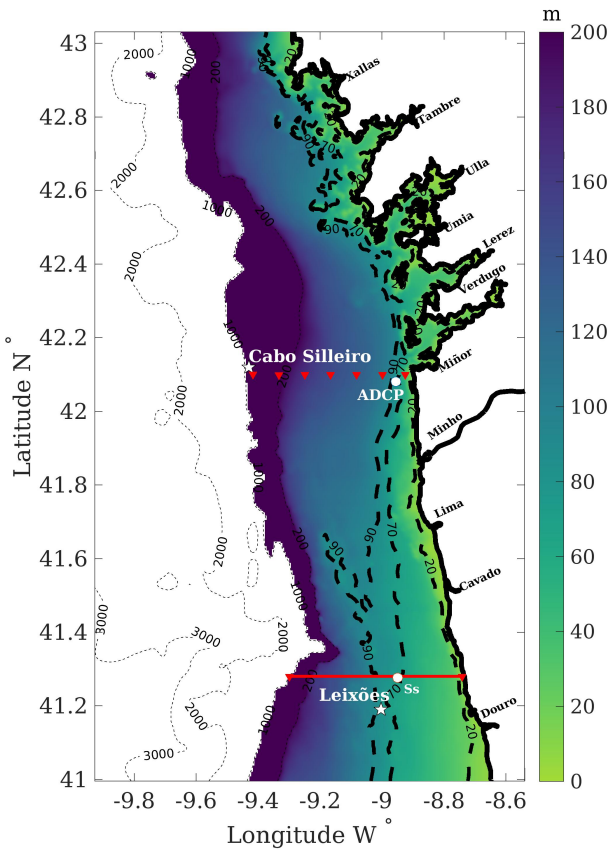

FIGURE 4.1: Bathymetric grid of the highest resolution grid in the CROCO model (local), with red triangles marking the monthly CTD stations (Ns). A white circle shows the location of ADCP, and white stars represent the locations of wave buoys (Cabo Silleiro and Leixões). In the Southern area of the study site, the section marked with a red line and a station (Ss) with a white circle, were chosen to represent this area's dynamics. From these locations relative data from the model results was retrieved.

4.3 Results

In the following sections, the estimates of waves, circulation and sediments were evaluated separately. The results of the statistical analysis were gathered into one table (Table 4.1) for a better general overview of the model assessments.

TABLE 4.1: The duration of the modelled period was 14 months, from November 2008 until December 2009. The results of the wave model and the ocean model with the sediment transport module during this term were analyzed based on five statistical parameters: mean value, correlation coefficient, RMSE, BIAS and model skill. The asterisk * in the ocean model section, indicates, that the absolute values of each variable were considered.

Wave model	Location	Source	Mean	Cor.	RMSE	BIAS	Model skill
Sig. wave height (m)	Leixões	Modeled	2.18	0.95	0.15	-0.02	0.97
		Observation	2.20				
	Cabo Silleiro	Modeled	2.43	0.96	0.40	-0.05	0.98
		Observation	2.48				
Peak wave period (s)	Leixões	Modeled	10.85	0.80	0.61	-0.33	0.89
		Observation	11.18				
	Cabo Silleiro	Modeled	10.80	0.81	1.63	0.95	0.85
		Observation	9.85				
Peak wave direction (∘)	Leixões	Modeled	293	0.96	9.92	-5.82	0.98
		Observation	299				
	Cabo Silleiro	Modeled	280	0.95	28.10	-6.43	0.97
		Observation	287				

Ocean model	ADCP	Source	Mean	Cor.	RMSE	BIAS*	Model skill
Meridional (v) (m/s)	65.5 mab	Modeled	0.18*	0.72	0.17	0.007*	0.81
		Observation	0.17*				
	2.5 mab	Modeled	0.10*	0.71	0.09	0.05*	0.76
		Observation	0.06*				
Zonal (u) (m/s)	65.5 mab	Modeled	0.05*	0.19	0.09	-0.02*	0.49
		Observation	0.07*				
	2.5 mab	Modeled	0.03*	0.33	0.03	0.01*	0.56
		Observation	0.02*				
Temperature (C°)	2.5 mab	Modeled	12.9	0.85	0.50	-0.19	0.90
		Observation	13.1				

Sediment module	ADCP	Source	Cor.	Measured against
Max. w-c shear stress (Pa)	Bot	Modeled	0.65	Backscatter (dB)
Max. w-c shear stress (Pa)	Bot	Modeled	0.90	*Villacieros-Robineau et al.* (2019) (Pa)

4.3.1 Wave model

An overview of the wave model and its application, using a very similar configuration, was presented in the preceding chapter (Chapter 3), which has been previously published in *Viitak et al.* (2020). In this section, the parameters entering the hydrodynamic model CROCO were compared to two wave buoys, located in the local grid (Figure 4.1). The validation of the regional grid is not shown here, as it demonstrated similar tendencies observed in the local grid and all the sediment transport analysis was done, considering the results of the highest resolution grid.

In the ocean model, the wave field was characterized using the information about the amplitude of waves, that is, one-half of the significant wave height, peak wave period and direction.

The wave model SWAN skillfully reproduces the evolution of the wave field. The significant wave height and peak wave direction were underestimated, as can be confirmed by the negative values of BIAS (Table 4.1). This was especially noticeable during winter periods of high energy, for example during mid-January 2009 and the end of November 2009, in both wave buoys for significant wave height (Figure 4.2 a), b)) and it has been reported to be one of the common problems of SWAN (*Silva et al.*, 2015). The underestimation tendency reduces significantly during late spring, summer and early autumn, with lower wave energy conditions. The q-q plot vividly confirms these tendencies. Very similar distributions can be seen, between the model and wave buoy data in Leixões and Cabo Silleiro for significant wave heights under 5 m (Figure 4.3 a) and d)). When these values are exceeded, the model begins to underestimate the wave heights.

The peak wave period was represented reasonably well (Figure 4.2 c), d)). According to the BIAS value 0.95 s in the deeper water buoy, Cabo Silleiro, an overestimation occurred. Where as, the shallower water buoy demonstrated slight underestimation, with BIAS -0.33 s. Much of the same propensity could be seen from the q-q plot, revealing further details. The overestimation in the Cabo Silleiro wave buoy was mainly a contribution of shorter wave periods, roughly under 13 s. As the distribution on the q-q plot started to diverge notably with higher wave periods, demonstrating an underestimation of the model (Figure 4.3 d)). A similar trend could be observed in the wave buoy Leixões. Short waves with periods under 10 s were eminently overestimated, while overall the differences between the observations and the model increased with decreasing wave period. The underestimation tendencies arise with periods over 13 s and higher (Figure 4.3 b)). It also seems to be the most challenging wave parameter to simulate, as the correlation coefficient was the lowest, around 0.80 at different wave buoy locations and model skill ranged between 0.85-0.89. On the other hand, significant wave height and peak direction were in very good accordance with the observations, exhibiting a correlation coefficient over 0.95 and model skill over 0.97. The RMSE improves with decreasing water depth, due to the improved representation of the buoy location in the model, demonstrating values of 0.15 m for the significant wave height, 0.61 s for peak wave period and 9.92° for peak wave direction (Table 4.1).

Compared with similar studies, the current model configuration presents reliable results with the same level of accuracy or better, in the Iberian Peninsula (*Rusu and Soares*, 2013; *Rusu et al.*, 2015; *Silva et al.*, 2015) and the rest of the world (*Soares et al.*, 2014).

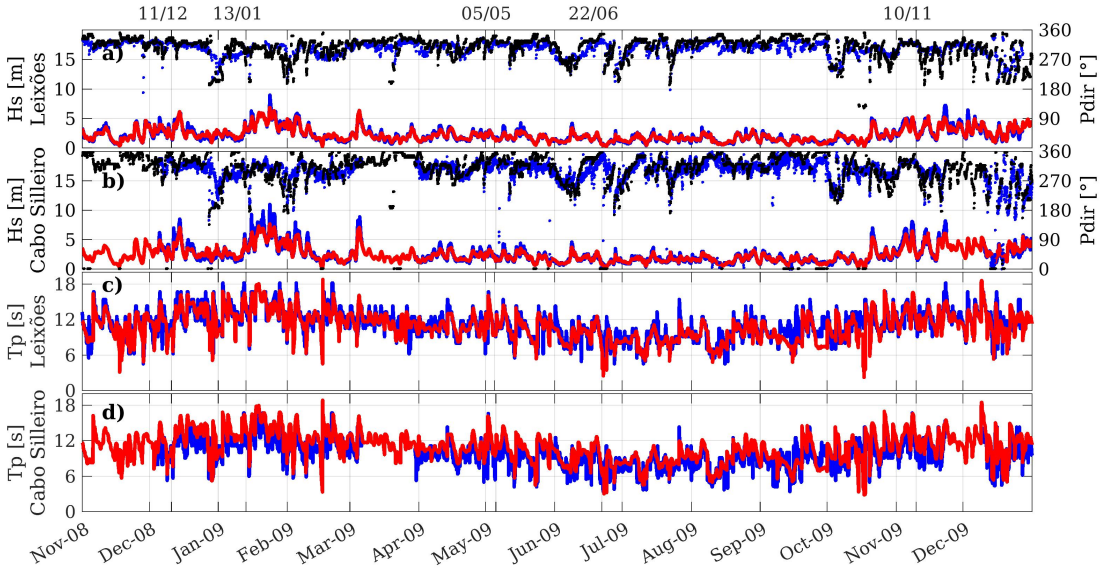

FIGURE 4.2: The wave model metrics comparison with wave buoys: a) and b) the significant wave height (red - modelled, blue - observations) and peak wave direction (black - modelled) measured at wave-buoys Leixões (41.32°N, −8.98°W, 83 m) and Cabo Silleiro (42.12°N, −9.43°W, 600 m), respectively. See Figure 4.1 for locations on the shelf. c) and d) the peak wave period (red - modeled, blue - observations) at Leixões and Cabo Silleiro, respectively.

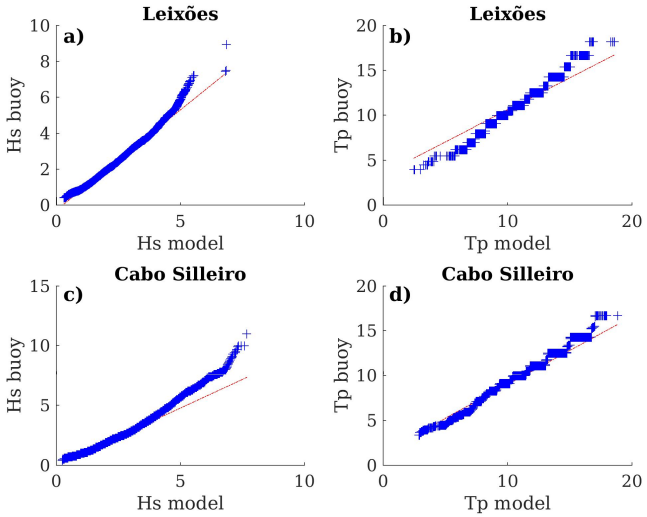

FIGURE 4.3: Comparison of the distributions between the wave model output and wave buoy using q-q plot: a) and c) the significant wave height, b) and d) the peak wave period at the wave buoy Leixões and Cabo Silleiro locations, respectively.

4.3.2 Hydrodynamic model

The ADCP measurements close to Cabo Silleiro (Figure 4.1 shows location) enabled the recording of the current velocity at various depths along the water column. The ocean model successfully reproduced the meridional (v) and zonal (u) current components in the surface, middle and bottom layers (Figure 4.5 and 4.6). It was possible to verify that the alongshore directional component (v) was modelled better than the across-shore component (u). Furthermore, the bottom layer was more accurately represented than the surface one for the latter component, whereas the meridional component did not demonstrate such significant differences. The statistical analysis confirmed these tendencies (Table 4.1). A correlation coefficient over 0.71 and model skill over 0.76 for component v was obtained, whereas, with component u, the correlation coefficient was 0.19 with a model skill score of 0.49 for the surface layer and at the bottom layer 0.33 with model skill 0.56.

During the configuration process, various combinations of stretching factors for the surface (θ_s) and bottom (θ_b) were tested to have a balance between the numerical stability of the model, computational expense and the requirements of the application. The utmost importance of the BBL dynamics in the study led to a reduction of the resolution at the surface layers and reinforcement at the bottom layers. In general, the model was slightly underestimating the current velocity meridional component v in the surface layers, with positive velocity values above 0.2 m/s (Figure 4.4 a)). An overestimation occurred at the bottom layers with velocities over 0.1 m/s (Figure 4.4 c)). The zonal component u was slightly underestimated at the surface, with negative velocity values below -0.05 m/s and overestimated with values above 0.15 m/s (Figure 4.4 b)). At the bottom layers the model underestimated velocities below -0.03 m/s and higher than 0.03 m/s (Figure 4.4 d)).

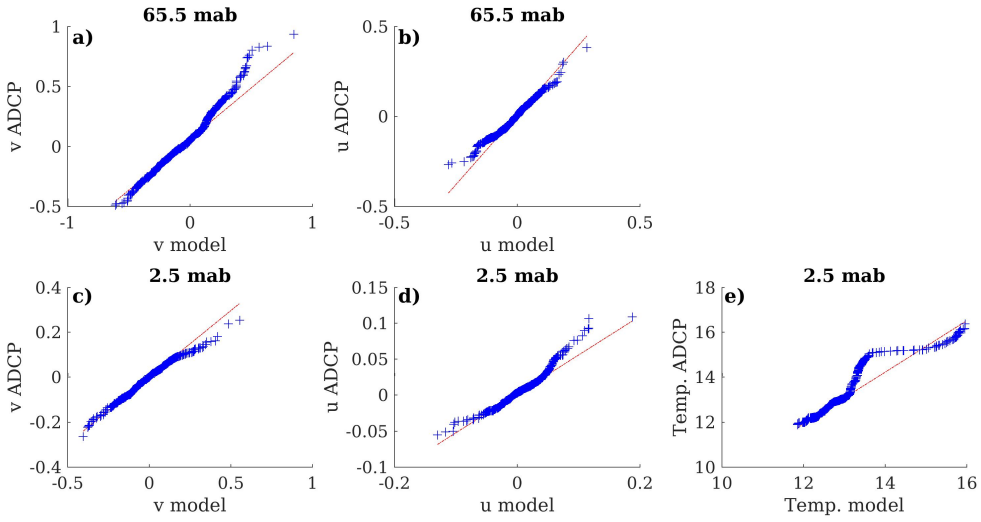

FIGURE 4.4: Comparison of the distributions between the CROCO model and ADCP measurements using q-q plot: a) and c) The meridional current component (v), b) and d) the zonal current component (u), e) temperature at the ADCP location in the surface and bottom layers, respectively.

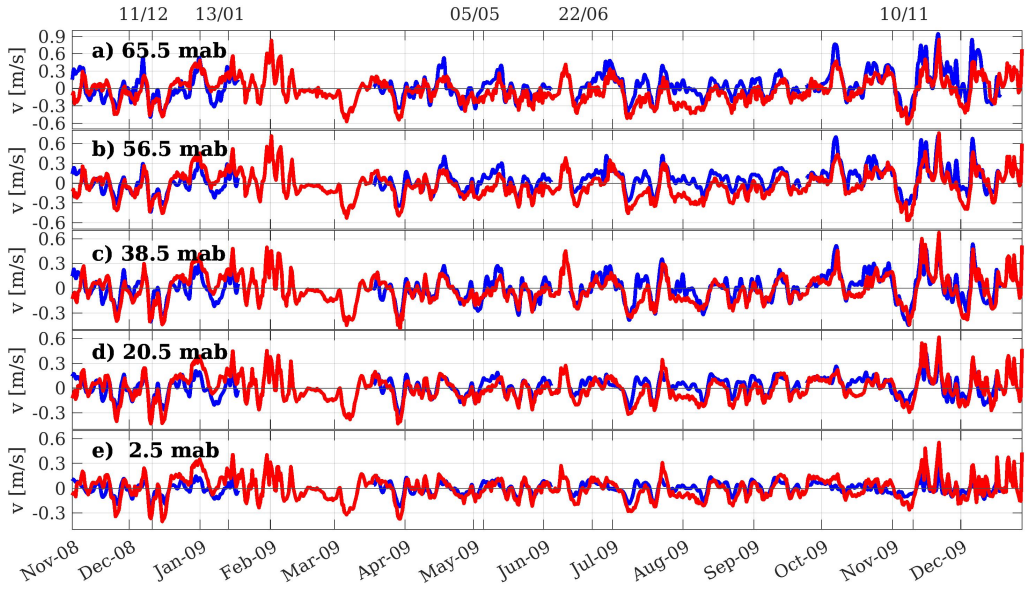

FIGURE 4.5: Meridional current component (v) obtained with the ADCP (blue) and the model (red) at various depths along the water column: a) 65.5 mab, b) 56,5 mab, c) 38.5 mab, d) 20.5 mab and 2.5 mab. Positive values indicate the Northward direction.

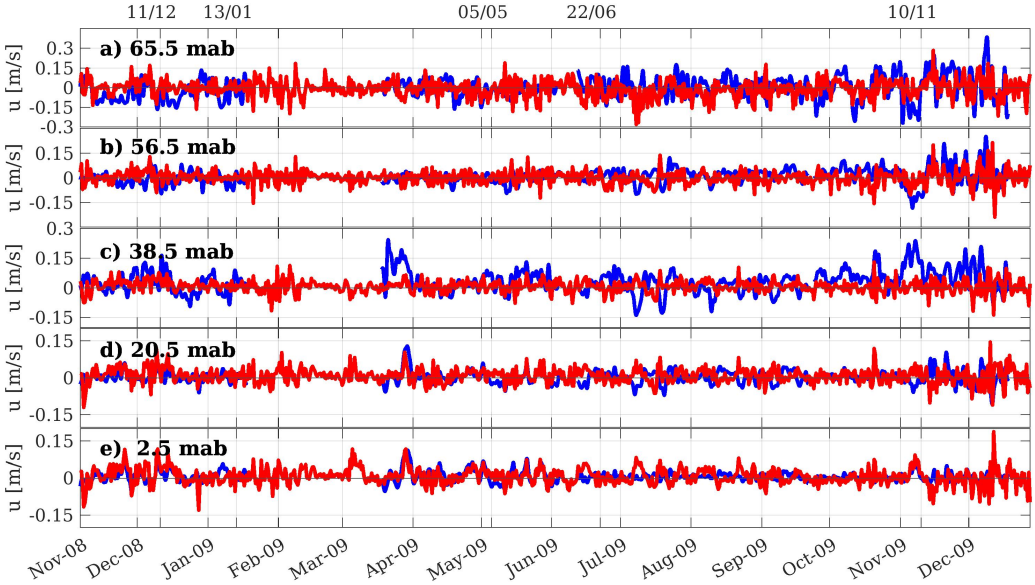

FIGURE 4.6: Zonal current component (u) obtained with the ADCP (blue) and the model (red) at various depths along the water column: a) 65.5 mab, b) 56,5 mab, c) 38.5 mab, d) 20.5 mab and 2.5 mab. Positive values indicate the Eastward direction.

Additionally, the simulated temperature at 2.5 mab, showed a very good agreement with the observational data (Figure 4.7). An increase in the temperature can be observed

in the measurement data at the beginning of October 2009, which was underestimated by the model. Nevertheless, the fluctuations in November and December 2009 were relatively well captured. A correlation coefficient of 0.85, a model skill of 0.90 and an RMSE of half degrees indicate a good performance of the model (Table 4.1). The q-q plot demonstrated that temperatures below 13 °C were simulated with greater accuracy at the bottom layers. Temperatures between 13-15 °C tend to be lower in the model simulation, whereas higher temperatures were overestimated (Figure 4.4 e)).

The statistical analysis of the current velocity components and temperature compares very well with similar studies (*Cordeiro*, 2018).

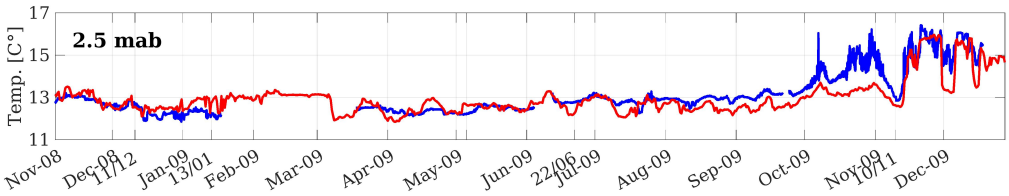

FIGURE 4.7: The temperature at 2.5 mab obtained with the ADCP (blue) and modelled (red)

.

The point measurements gave a comparatively good idea about the modelling system performance and the margin of error, which should be taken into account when interpreting the results. To understand how skillfully the model simulates different seasonal events, the results were compared to the temperature and salinity profiles obtained from the hydrographic surveys (Figure 2.1 shows location). Detailed descriptions of the following events can be found in *Villacieros-Robineau et al.* (2019) and *Cordeiro et al.* (2021).

Pre-storm upwelling event on December 11, 2008 The Northerly winds which preceded the event (Figure 4.9) promoted upwelling-driven circulation patterns, creating strong Southward flowing currents across the whole water column, presenting maximums close to -0.46 m/s and -0.36 m/s in the surface and bottom layers, respectively (Figure 4.5). At the same time, the significant wave height decreased by half, to 2 m, in wave buoy Cabo Silleiro (Figure 4.2).

The temperature and salinity distributions recorded during the hydrographic survey reflected a well-established upwelling profile (Figures 4.8 a), b)). A clear distinction between the warm and salty surface waters moving oceanwards and colder waters being transported through the bottom layers towards the coast could be seen. Peaks in the runoff from Rías were observed a day before the event, e.g. Lerez 95 m^3/s, Ulla 83 m^3/s (Figure 4.10), and the freshwater patch extended out to the shelf (Figures 4.8 b)). The simulation depicted these conditions fairly well, demonstrating very similar profiles of temperature and salinity, although the waters from the river did not extend as far out to the shelf (Figures 4.8 c) and d)). These conditions were followed by brief relaxation in the circulation regime, only to pick up again and succeed with a peak of a very strong storm 4 days later, described in the Chapter 5 section 5.3.

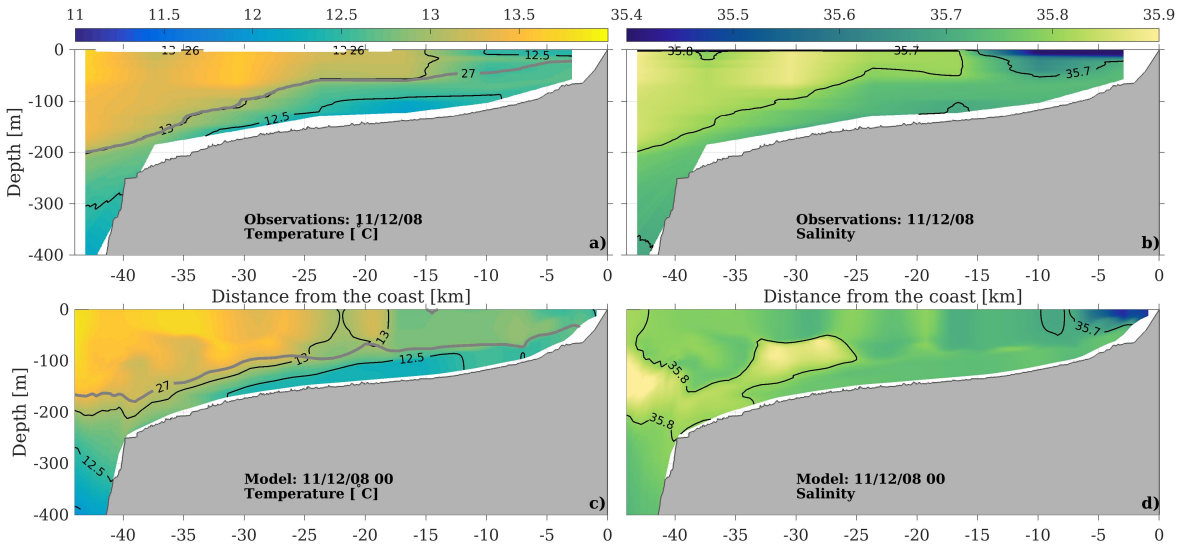

FIGURE 4.8: Pre-storm upwelling event. On December 11, 2008, a), b) temperature and salinity were obtained along a cross-section between −8.93° W to −9.44° W during the hydrographic survey, and c), d) simulated with the model. The temperature graphs show isopycnal 27.0 kg/m^3 (grey).

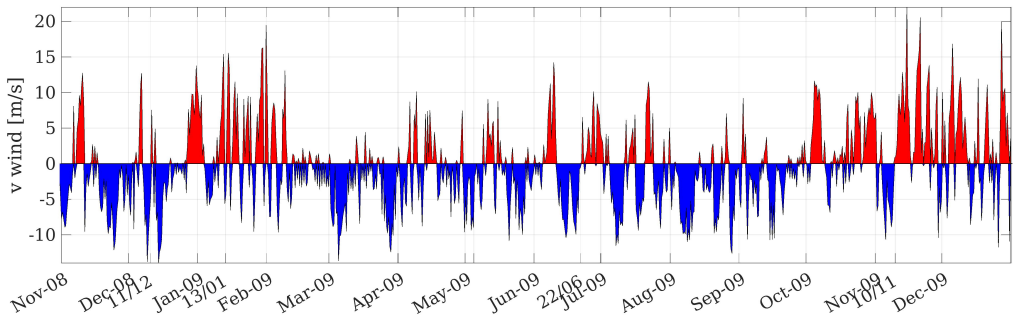

FIGURE 4.9: The evolution and variation of kinematic wind speed alongshore component (v) in the ADCP location (Figure 4.1), where positive and negative values are represented by red and blue colour schemes, respectively.

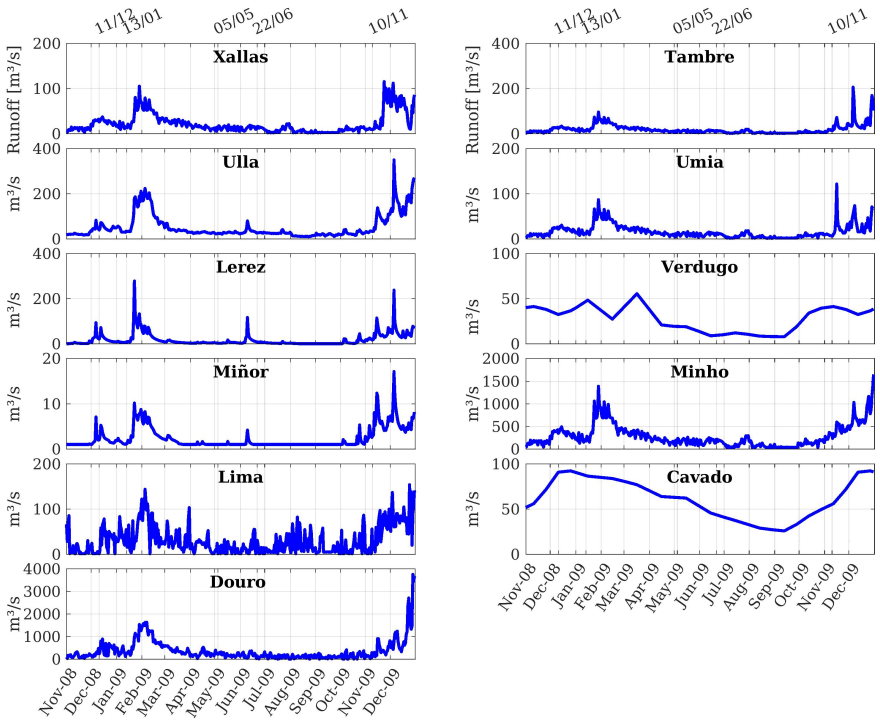

FIGURE 4.10: Runoff of the rivers considered in the model local grid (Figure 4.1).

Winter mixing on January 13, 2009 On this cruise, a downwelling-favourable circulation regime was detected (Northward directed alongshore component, Figure 4.5, Southerly winds, Figure 4.9), with strong waves close to 5 m (Figure 4.2) and high river runoff before the event from Douro and Minho, 585 m^3/s and 322 m^3/s, respectively, (Figure 4.10). These conditions determined the water column stratified structure in the inner shelf. The temperature and salinity profiles demonstrate a clear front between the fresh waters from the rivers and saline ocean waters, with a difference in salinity of 0.5 (Figure 4.11 a), b)). The model replicated these conditions fairly well while indicating a lesser intrusion of the river waters and maintaining the thermohaline front closer to the coast (Figure 4.11 c), d)).

Spring time upwelling, on May 5th, 2009 During the event the wave energy was low (Hs $\leq$ 2 m in Leixões and Cabo Silleiro, Figure 4.2), while the river discharged remained $\leq$ 200 m^3/s from Minho and Douro rivers Figure 4.10. An upwelling-driven circulation was observed, resulting from the Southward wind regime (Figure 4.9). The colder subsurface oceanic waters moved towards the coast, where the isotherms and isohalines were shifted closer to the surface (Figure 4.12 a), b)). On the other hand, in the model simulations, there could be seen more mixing in the surface layers, which positioned the isotherms deeper in the water column and saline oceanic water propagated further toward the coast in the mid-layers (Figure 4.12 c)).

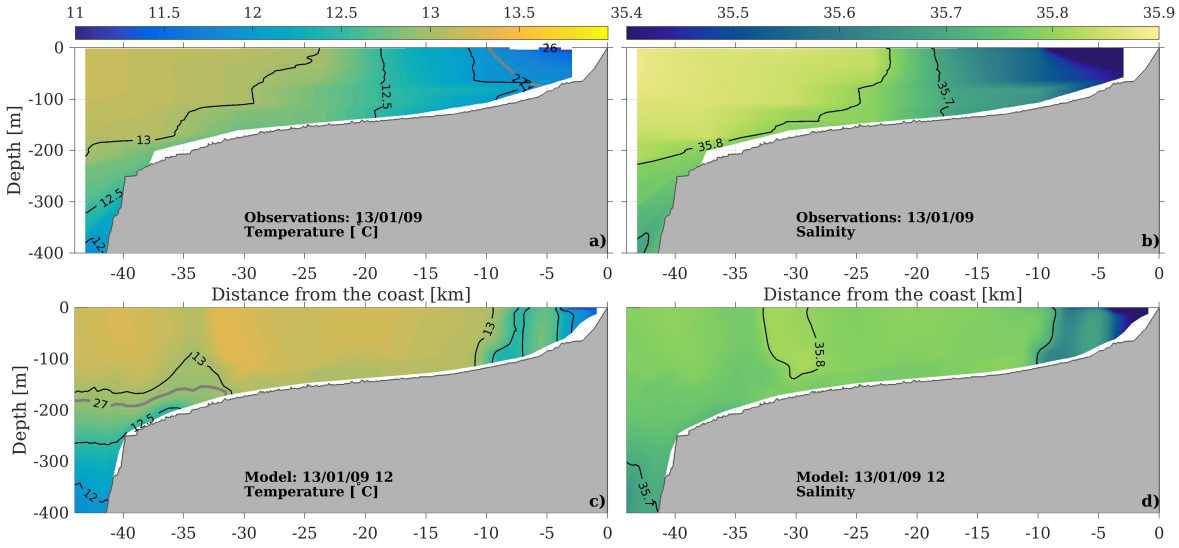

FIGURE 4.11: Winter mixing. On January 13, 2009, a), b) temperature and salinity were obtained along a cross-section between $-8.93°$ W to $-9.44°$ W during the hydrographic survey, and c), d) simulated with the model. The temperature graphs show isopycnal 27.0 kg/m^3 (grey).

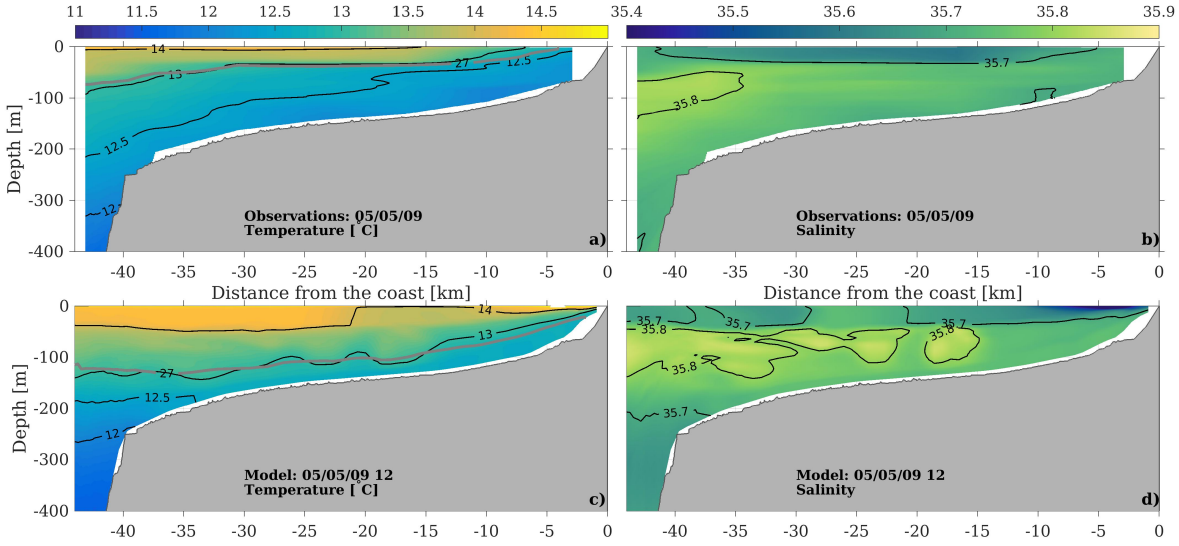

FIGURE 4.12: Springtime upwelling. On May 5th, 2009, a), b) temperature and salinity were obtained along a cross-section between $-8.93°$ W to $-9.44°$ W during the hydrographic survey, and c), d) simulated with the model. The temperature graphs show isopycnal 27.0 kg/m^3 (grey).

Summer stratification, on June 22, 2009 Highly stratified surface layers resulted from very mild wave conditions, minimum river runoff (Figure 4.10) and a relaxation period in the circulation regime from upwelling (Figure 4.9). Temperature profiles of measurements and the model (Figure 4.13 a), c)) demonstrate maximums over 16 C° at the upper 30 m and 60 m, respectively. Intense stratification in the salinity profiles was very similar in both cross-sections (Figure 4.13 b), d)). Traces from the preceding upwelling event could be observed both in the observational data and model results, with temperature and salinity minimums of 12.5°C and 35.75 - 35.7, respectively.

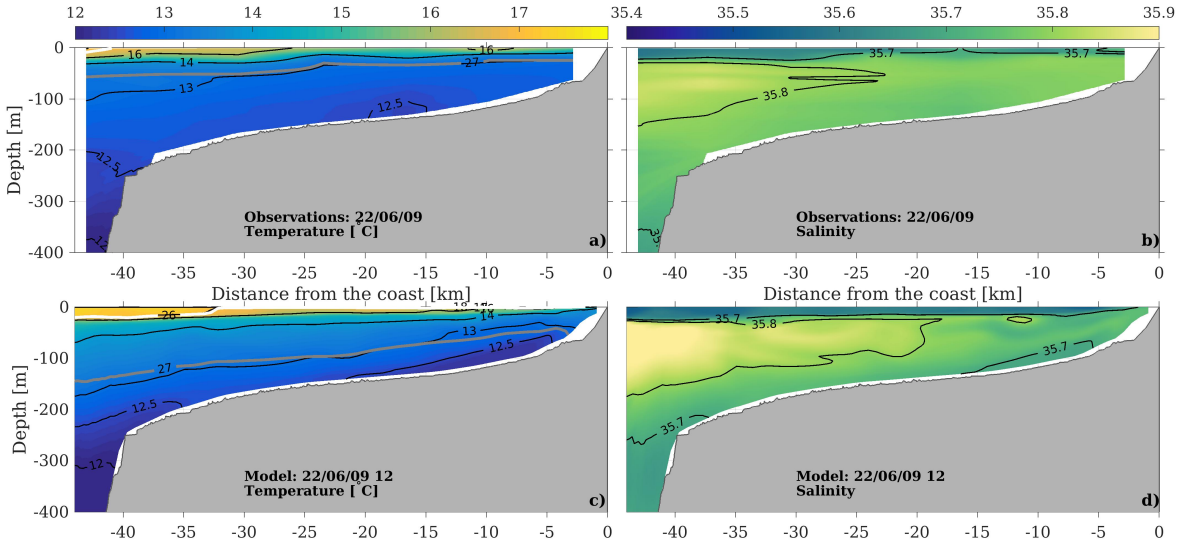

FIGURE 4.13: Summer stratification. On June 20th, 2009, a), b) temperature and salinity were obtained along a cross-section between −8.93° W to −9.44° W during the hydrographic survey, and c), d) simulated with the model. The temperature graphs show isopycnal 27.0 kg/m^3 (grey).

Post-storm winter upwelling, November 10, 2009 Two days before the hydrographic survey a storm peak had passed. During which the significant wave height reached 8 m at the Cabo Silleiro wave buoy (Figure 4.2), the river discharge was weak (Figure 4.10) and strong bottom currents were directed coast-ward and oceanward at the surface layers (Figure 4.5 and 4.6). The post-storm conditions were registered during the cruise, presenting upwelling enforced thermohaline structure, with surface currents transporting the low salinity water toward the ocean and intrusion of saline water tongue in the mid-layers (Figure 4.14 a), b)). The model demonstrated a relatively similar state of the temperature and salinity profiles, with slight differences in the location of the isotherms and isohalines (Figure 4.14 c), d)).

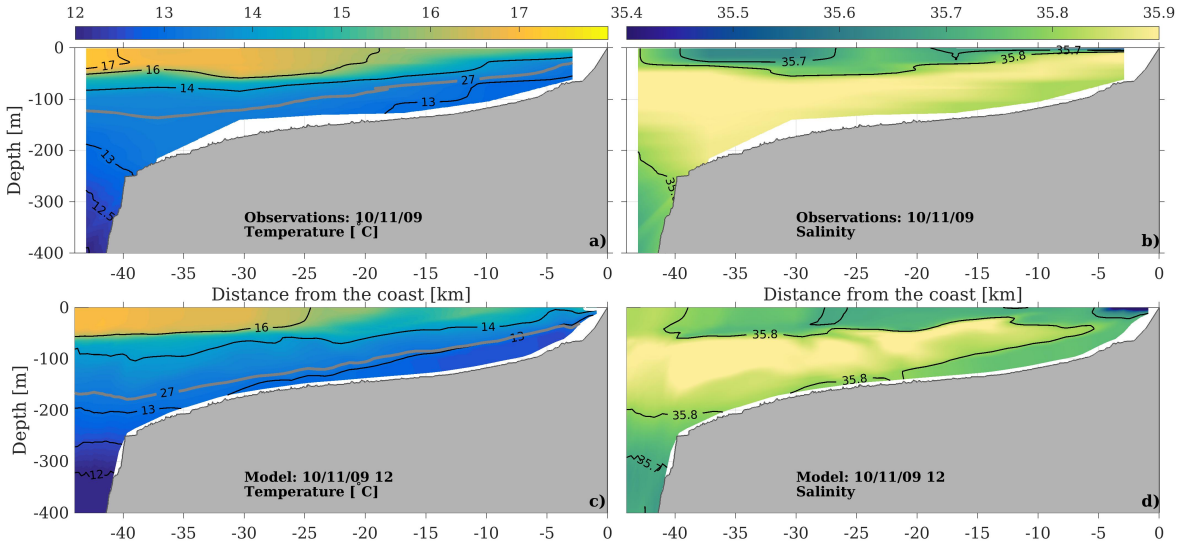

FIGURE 4.14: Post-storm conditions of winter upwelling. On November 10th, 2009, a), b) temperature and salinity were obtained along a cross-section between −8.93° W to −9.44° W during the hydrographic survey, and c), d) simulated with the model. The temperature graphs show isopycnal 27.0 kg/m^3 (grey).

4.3.3 Sediment transport model

A countless number of tests were performed to study and understand the model sensitivity to different coefficients and formulations related to sediment transport. It was concluded that in the current application, the maximum wave-current-induced shear stress was highly sensitive to bottom roughness length. Initially, the mean bottom roughness length Z_0 = 0.5x10^{-3} m (0.5 mm) was considered, with bottom roughness k_s= 1.5 cm, assuming that the bed is sandy and unrippled (*Soulsby et al.*, 1993). In the following simulations, different roughness components (k_s, k_t, k_f) were included one by one, such as the only grain-related component (k_s), the transport-related term (k_t) and the effect of ripples (k_f) (see Chapter 2 section 2.4.3 for more detailed description).

Throughout the 2 month test period, from November to December 2008, the highest values of the maximum wave-current shear stress were obtained with constant value of k_s= 1.5 cm and the lowest values considering only the grain-related component of the bottom roughness ($k_0 = k_s$) (Figure 4.15 grey line marked as discontinuous and with asterisks, respectively). Similar results were obtained, using the grain-related component and the transport-related term together ($k_0 = k_s + k_t$), while also adding the influence of ripples ($k_0 = k_s + k_t + k_f$)(continuous grey and red lines in Figure 4.15, respectively).

Comparing the results with the shear stress estimates of *Villacieros-Robineau et al.* (2019), the constant bottom roughness (k_s= 1.5 cm) overestimated notably the stress, while generally a slight underestimation could be seen with all of the rest of the simulations. It

was concluded, that in the present application, the most suitable results were obtained while considering all three components of the roughness. This allows different physical processes to be represented in the model simulations.

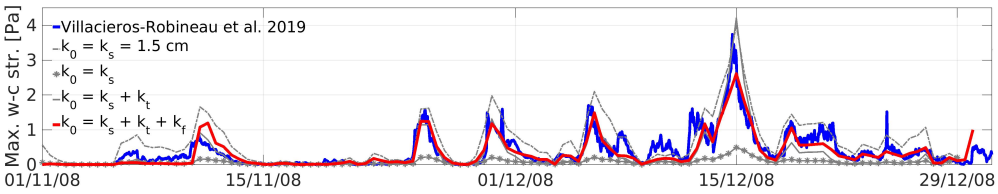

FIGURE 4.15: The maximum wave-current induced shear stress calculated by the model at the ADCP location (42.08° N, −8.93° W) while using different bottom roughness definitions, with local depth 74 m. Additionally, the estimates of the shear stress based on the study of *Villacieros-Robineau et al.* (2019), with a local depth of 75 m.

The evolution of the combined shear stress at the bottom correlated well with the backscatter signal of the ADCP at the lower layers, from November 2008 till December 2009 (Figure 4.16 a), b)). A correlation coefficient of 0.65 was obtained for the 3 mab backscatter time series and the maximum wave-current shear stress at the bottom, which was in the same order of magnitude as estimated in *Villacieros-Robineau et al.* (2019) for a similar period. A very high concordance was found between the referred work and the current study, with a correlation of 0.90 (Table 4.1). The q-q plot demonstrated a high concordance between backscatter values below 80 dB and modelled maximum wave-current shear stress till 0.5 Pa (Figure 4.17 a)). For higher values, the distributions diverged. The discrepancy was also revealed in the maximums of the shear stress, while identical peaks did not always have the same response in the backscatter signal, for instance, the storm peak on December 15, 2008, and November 21, 2009 (Figure 4.16 b)). Most likely this was linked to the origin of the sediment source. The higher backscatter signal values at the bottom layers could be due to the entrance of siliciclastic particles from the river plumes. Also, possibly transported by bottom bedload or saltation from other areas of the shelf. On the other hand, the maximum wave-current shear stress estimated by *Villacieros-Robineau et al.* (2019) and obtained in this study, demonstrated relatively similar behaviors (Figure 4.17 b)). The max. wave-current shear stress up to 1 Pa correlates comparatively well and for greater values, the CROCO model estimates were higher than those of *Villacieros-Robineau et al.* (2019).

The concentration of sediments at the bottom-most layer of the model, approximately 1.5 m from the sea bed, strongly followed the maximum wave-current shear stress (Figure 4.16 c)). The observed total mass flux in the sediment trap demonstrated strong seasonal influences (Figure 4.16 d)). The correlation between the backscatter data and the maximum wave current shear stress, with the sediment mass flux, was most evident during winter seasons, associated with strong re-suspension of surface sediments (*Villacieros-Robineau et al.*, 2019). On the other hand, during summer and spring, the backscatter signal also reflects biological production processes in the upper photic zone (*Zúñiga et al.*, 2016). The

mean suspended sediment concentration, for the same time intervals across the whole water column, indicates a similar temporal variability as the sediment mass flux captured by the sediment trap, especially throughout October-December 2009 (Figure 4.16 e) red bars). While looking at the 1 m thick layer 35-34 m from the sea surface, where the sediment trap was situated (Figure 4.16 e) magenta bars), the model results demonstrate the proportion of re-suspended material from the sea bed during the autumn-winter periods (December 2008 – January 2009 and November 2009).

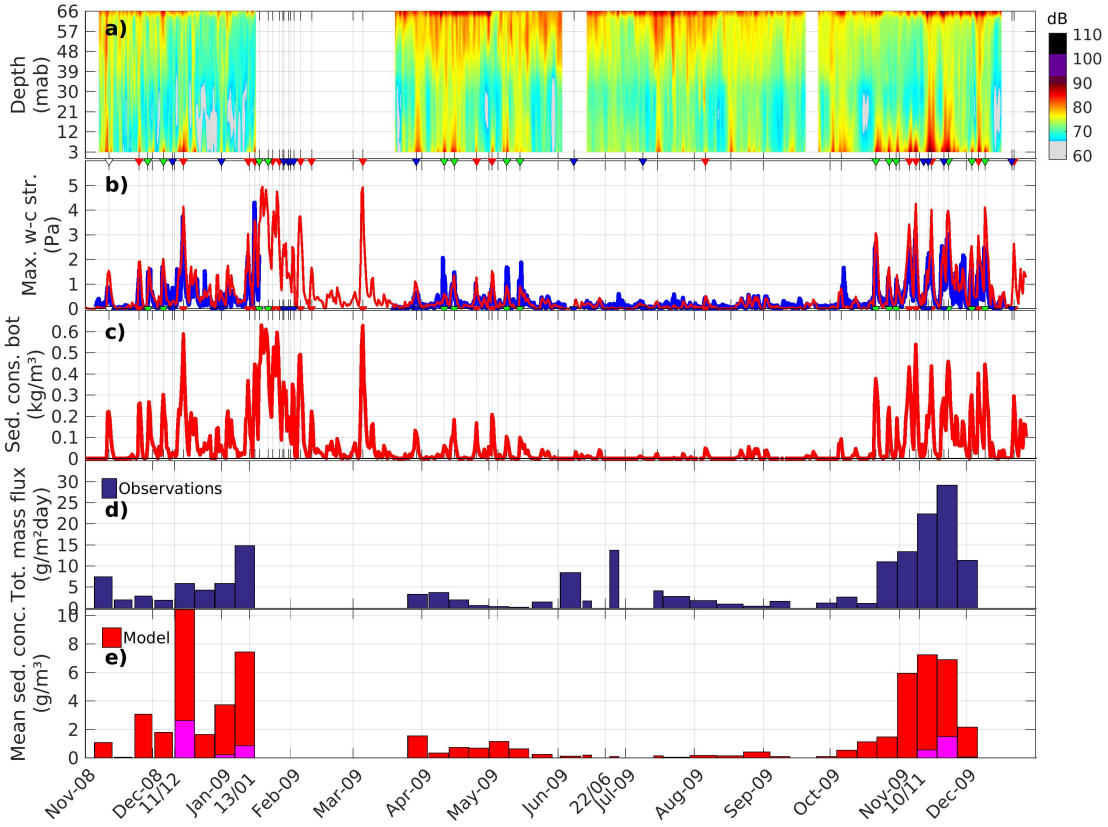

FIGURE 4.16: The information was captured in the ADCP measurements location, with local depth 75 m and in the model 74 m (42.08°N, −8.93°W): a) backscatter signal, the blue, green and red triangles represent the current, wave or co-dominance events, respectively. b) Maximum wave-current shear stress obtained by *Villacieros-Robineau et al.* (2019) (blue) and modelled (red), c) sediment concentration at the bottom-most grid cell. d) Total mass flux from the sediment trap, e) mean suspended sediment concentration across the water column (red) and in a 1 m thick layer between 35-34 m from the surface (magenta).

.

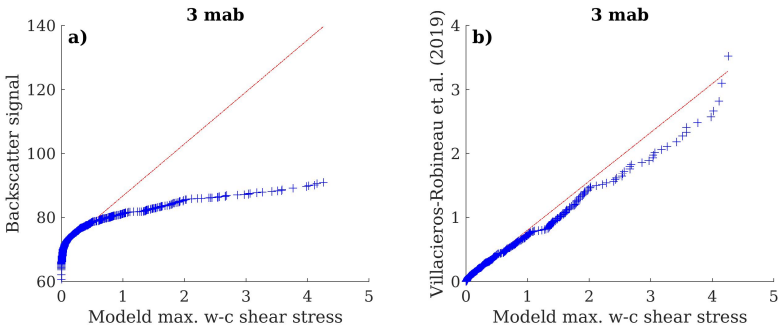

FIGURE 4.17: Comparison of the distributions using q-q plot: a) backscatter signal at 3 mab, b) *Villacieros-Robineau et al.* (2019).

The turbidity and fluorescence data on each of the seasonal events, previously discussed, were compared with the sediment concentration values in suspension. Turbidity can give an insight into the presence of suspended particles scattered in the water column, while fluorescence depicts the processes related to biological productivity.

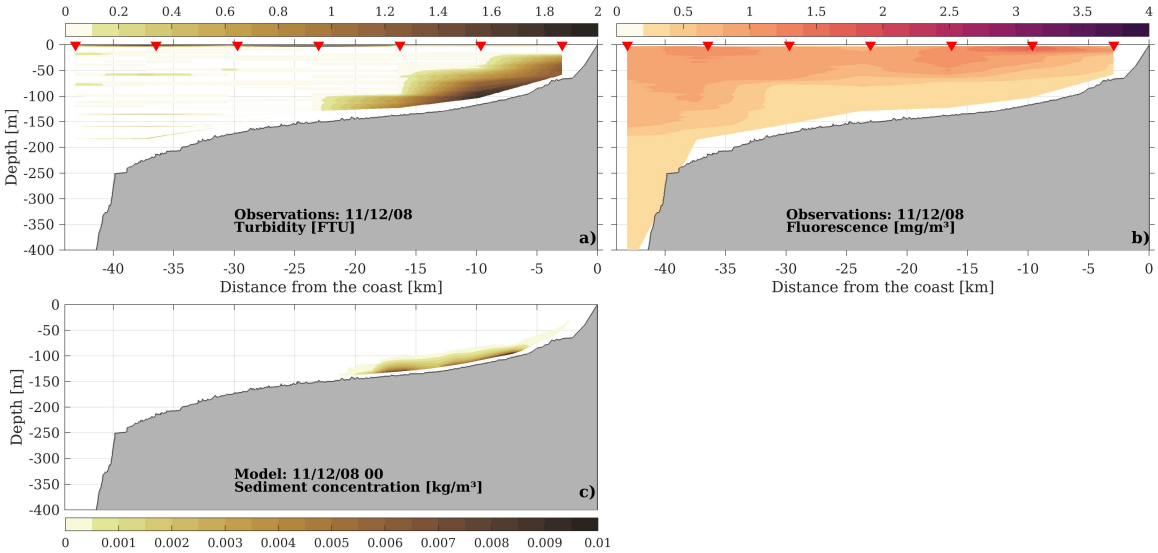

FIGURE 4.18: Pre-storm upwelling event on December 11, 2008, a), b) turbidity and fluorescence obtained along a cross-section between −8.93° W to −9.44° W during the hydrographic survey, and c) modelled sediment concentration.

On December 11 2008, the turbidity measurements indicated the presence of a thick nepheloid layer from the coast up to approximately 23 km offshore (Figure 4.18 a)). Its thickness was reduced from 40 m to 25 m while moving away from the shore. A very low concentration of sediment $< 0.01\ kg/m^3$ was observed from the model results nearly to the same extent across the shelf (Figure 4.18 c)). The maximum thickness of the bottom

nepheloid layer was roughly 20 m. The fluorescence values were below 0.5 mg/m^3, referring to low biological productivity close to the sea bed (Figure 4.18 b)).

The profiles obtained on January 13, showed a clear bottom nepheloid layer that extended out to the shelf (Figure 4.19 a)) coinciding with the outward limit of the salinity front (Figure 4.11 b)). The turbidity and fluorescence sections also indicated the presence of a surface nepheloid layer (Figure 4.19 b)). From the model results, only the bottom nepheloid layer can be observed, which did not extend as far offshore as seen in the observational data (Figure 4.19 c)). The highest sediment concentration values were close to the bottom, around 0.1 kg/m^3, while with increasing distance, the concentration reduced to below 0.005 kg/m^3 at higher levels of the water column.

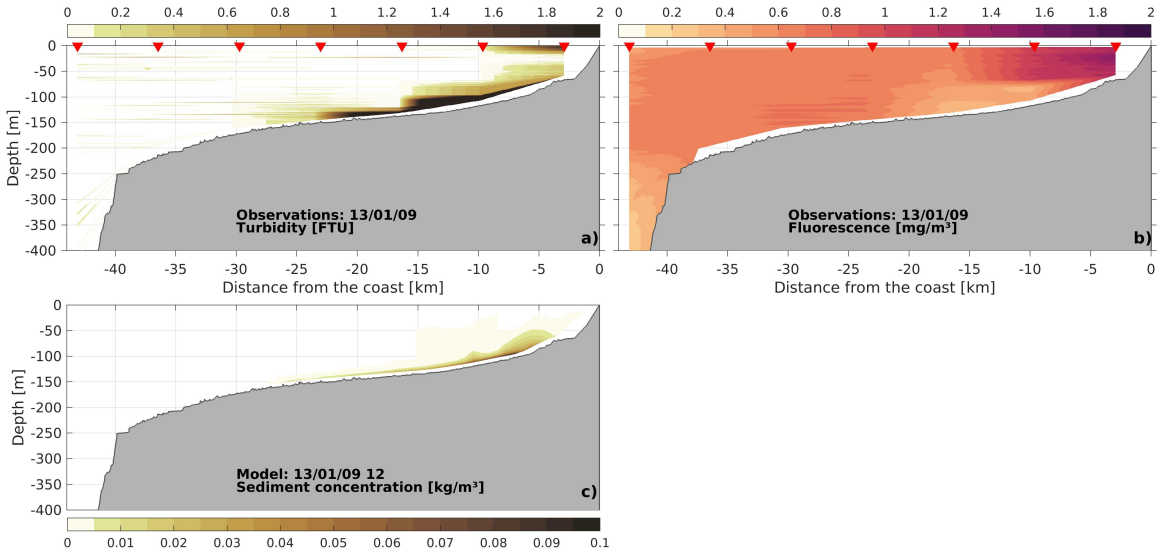

FIGURE 4.19: Winter mixing on January 13, 2009, a), b) turbidity and fluorescence obtained along a cross-section between −8.93° W to −9.44° W during the hydrographic survey, and c) modelled sediment concentration.

On May 5th, there can be seen surface nepheloid layer from the turbidity and fluorescence data (Figure 4.20 a), b)), but turbidity also shows a low intensity bottom nepheloid layer. In the model, no sediments could be observed in the water column (Figure 4.20 c)). Although, 2 days before, on the 3rd of May, a brief storm reached a peak with a significant wave height of around 3 m (Figure 4.2) and upwelling favourable circulation (Figure 4.9). This created a relatively thin sediment concentration layer at the bottom seen from the simulations (Figure 4.20 d)).

In the summer event, June 22nd, no sediments in suspension could be observed from the model results, although the observations showed the presence of both bottom and surface nepheloid layers (Figure 4.21).

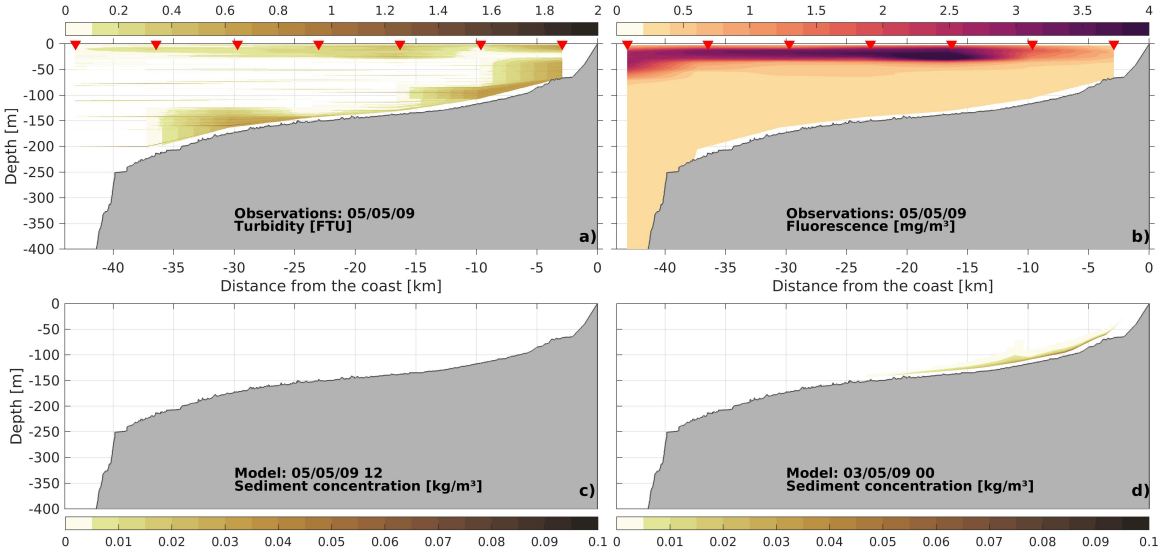

FIGURE 4.20: Spring time upwelling on May 5th, 2009, a), b) turbidity and transmittance obtained along a cross-section between −8.93° W to −9.44° W during the hydrographic survey, and c), d) modelled sediment concentration on 5th and 3rd of May, respectively.

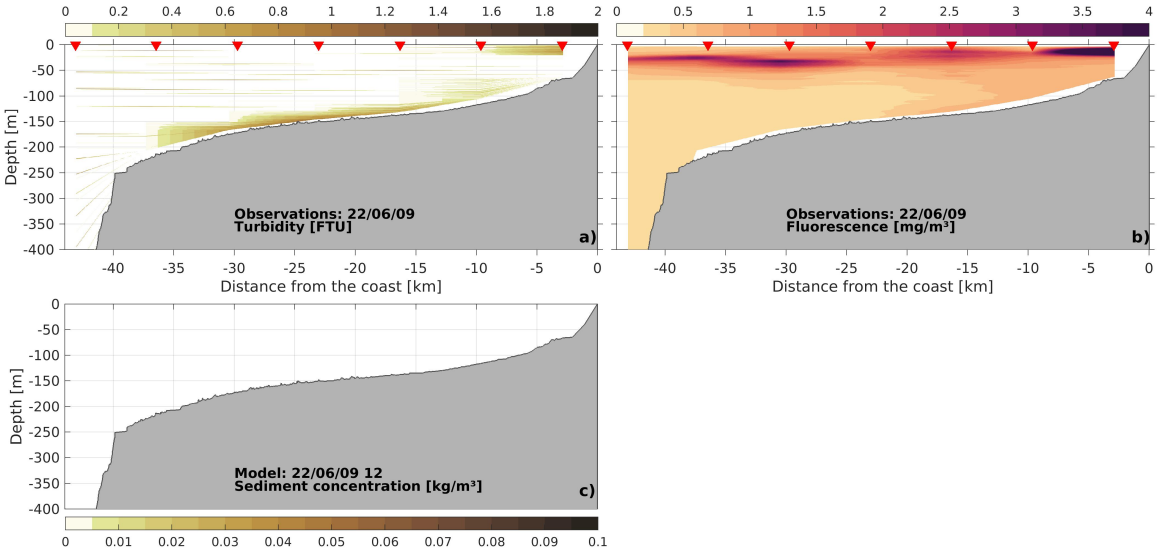

FIGURE 4.21: Summer stratification on June 22, 2009, a), b) turbidity and transmittance obtained along a cross-section between −8.93° W to −9.44° W during the hydrographic survey, and c) modelled sediment concentration on 22nd of June.

.

The turbidity data from November 10th showed a strong signal up to 10 km from the coast, decreasing from there on, and another bottom nepheloid layer in the deeper part of the slope (Figure 4.22 a)). A strong surface nepheloid layer signal was only captured by the fluorescence data (Figure 4.22 b)). On the cruise day, the model shows no sediments in suspension (Figure 4.22 c)). Although, 2 days before, a storm had passed and the simulations indicated the presence of the bottom nepheloid layer during that time (Figure 4.22 d)). During the storm, the significant wave height was between 5-8 m across the shelf (Figure 4.2) and bottom currents were directed southward at the bottom layers, reaching over -0.25 m/s at the ADCP location, according to the model (Figure 4.5).

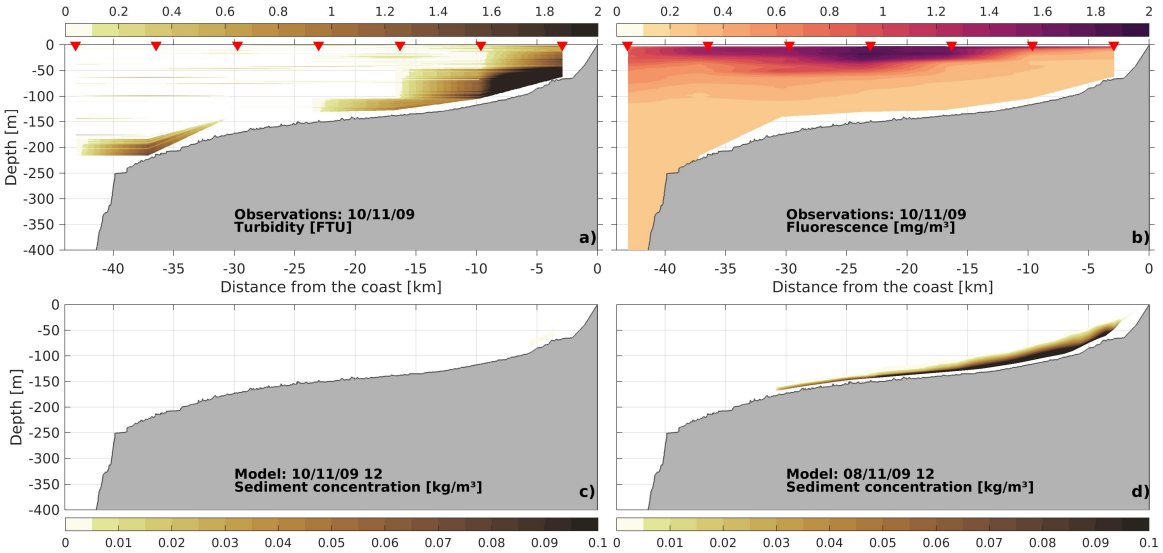

FIGURE 4.22: Winter upwelling post-storm conditions on November 10, 2009, a), b) turbidity and transmittance obtained along a cross-section between −8.93° W to −9.44° W during the hydrographic survey, and c), d) modelled sediment concentration on 10th and 8th of November, respectively.

.

4.4 Discussion

Waves and hydrodynamics A good agreement between the observational data from wave buoys and model results demonstrated the wave model's capability to represent adequately the wave field. The comparison revealed the wave model's tendency to slightly underestimate the significant wave height, peak wave period and direction during strong storm conditions with high energy. From the point of view of sediment transport modelling, the model-estimated maximum wave-current shear stress acting on the seafloor sediments is probably lower than reality. On the other hand, the meridional current component v

was slightly overestimated by the model at the ADCP location, whereas the zonal component u was underestimated at the bottom layers. Overall these differences between the measured and simulated current velocities will have a minimum impact on the shear stress calculations (*Oberle et al.*, 2014).

The seasonal events comparisons showed that the ocean model was able to simulate the dynamics of each of the events, with slight dislocation of the observed structures. The mixed surface layer during spring and summer reached greater depth within the model. The same tendencies have been observed by other studies (*Cordeiro et al.*, 2021). This may be due to the choice of the oceanic boundary layer mixing scheme, which most of the time produces relatively satisfactory results, but in some specific conditions leads to greater mixing. The plumes from the rivers advected less offshore than observed in the monthly cruise data. This may be related to the model configuration, where the salinity and temperature values were fixed at the mouth of the rivers. But also could be influenced by the fact that the comparison was made with the model snapshot. Nevertheless, the representation of rivers was considered reasonable taking into account the objectives of the current application.

Sediments The model results reflected the backscatter signal at the bottom layers. During autumn and winter periods, the ADCP measured high backscatter values, and this was also seen in the modelled suspended sediment concentration values. During spring and summer seasons, the backscatter signal was significantly weaker in the bottom layers and the simulations also indicated low sediment concentration values.

The total mass flux obtained through the sediment trap, located at the surface layers, demonstrated a clear seasonal variability. The same could be observed for the mean sediment concentration values across the water column. The re-suspended sediments from the seabed reached the upper layer of the water column only in winter months: December 2008, January 2009 and November 2009. This demonstrated the model's capability to reproduce the sediment dynamics at the bottom layers during high energy conditions on the shelf.

While looking at a vertical section across the water column, from the turbidity data, it was possible to observe both the bottom and surface nepheloid layers. The surface layers were mostly generated by the local biological activity and influenced by the river blooms, giving a stronger signal to the fluorescence data. These phenomena were not simulated by the model, as the biology module was not activated and rivers did not transport sediments in this simulation. Therefore, no surface nepheloid layers could be observed from the simulations. On the other hand, the bottom nepheloid layers were influenced much more by the wave and current activity that stirred up the sediments from the seabed, also observed in the model results. While the winter event on January 13, was represented well by the model, as the hydrographic conditions during the cruise permitted recording the re-suspension of sandy sediments. In other events, the sandy fraction had already been deposited, as the storms had passed a few days before the cruise, leaving behind the flocks and silt/clay fractions of the sediments that were not represented by the model.

The suspended sediment concentration at the ADCP location, where the first vertical level of the model stayed at 1.5 mab, demonstrated values in the same range in similar conditions as measured in the study of *Zhang et al.* (2016) with a lander deployed at 73 m depth in a sandy site off the river Douro. In 2014 during 55 hours from 16 of September, the significant wave height varied between 3-4 m with maximum heights around 6 m and current at 1.5 m above the bed presenting maximum values of up to 0.5 m/s, although remained generally under 0.2 m/s. The SPM demonstrated 4 peaks with the highest values approximating 0.4 kg/m^3. The observed particles belonged to silt and very fine sand classes, from which in the current study, the latter class was represented with two-size bins. The sediment concentration values obtained by the model in this study reached 0.6 kg/m^3 with wave conditions exceeding 7 m at the Cabo Silleiro wave buoy.

Another study by *Zhang et al.* (2019) recorded the SPM during intra- and post-storm periods in September 2014. Their findings showed a maximum SPM of 8 g/m^3 during post-storm conditions close to the outer extent of the Galician mud patch at approximately 9 m above the seafloor. Whereas, recordings with LISST100 at the Galician mud patch 30 cm above the seafloor, demonstrated SPM maximums close to 100 g/m^3 composed mostly of coarse silt and fine sands (50-200 μm). Based on the observational data covering the same period as the current study, (Castro per. comm.), showed the highest SPM between mid-November 2008 and January 2009, with a maximum of 10 g/m^3 across the water column. Similar values were observed in the mean suspended sediment concentration across the water column (Figure 4.16 e)). These maximum values represented in the current study, range in the same order of magnitude as found by several other studies referred to above, reinforcing the degree of confidence in the results.

4.5 Conclusion

Numerical simulations were conducted using a wave and ocean model with a sediment transport module to reproduce the suspended sediment transport of a sandy fraction on the NW Iberian continental shelf. The results obtained were compared against various *in situ* observational data sources. The statistical and quantitative analysis demonstrated that all the models were in relatively good agreement with the measured data while presenting some shortcomings.

The wave model SWAN tended to underestimate the wave energy in storm conditions. However, the evolution of the wave field in time, at various locations on the shelf, was represented comparatively well. The accuracy of the model outcome was at the same level compared to similar studies conducted or even slightly higher.

The ocean model demonstrated slight differences in the hydrographic parameters, but the statistical analysis demonstrated a reasonable error range that compared well with studies alike. The two-step validation process, considering point measurements and the extended salinity/temperature profiles across the shelf obtained through a hydrographic survey, demonstrated the reliable capabilities of the model to simulate shelf circulation.

The sediment transport model, with its limitations and simplifications, simulated skillfully the fundamental sediment transport processes and the seasonal variations on the shelf. The results obtained by the model were in agreement with similar studies, demonstrating results in the same order of magnitude. However, this study emphasizes the need for long-term sediment data sets, for better site-specific calibration.

Chapter 5

The role of driving forces in sediment transport processes

5.1 Introduction

A wide range of issues in the coastal ocean, such as long-term changes in the sea floor, the depiction of its habitants and the effects of contaminants, is related to the transport of sediments and the fate of the particles.

Sediment re-suspension, transport and deposition are determined by various hydrodynamic processes, sediment properties and characters of the seabed. Studies show that wind-driven currents are most effective in redistributing the sediments. An important factor for sediment re-suspension is wind-driven surface waves, which induce strong bottom shear stresses through bottom orbital motion (*Vitorino et al.*, 2002a; *Oberle et al.*, 2014). Although it has been found that generally, the tidal current alone isn't strong enough to resuspend sediments in the continental shelf (*Oberle et al.*, 2014; *Zhang et al.*, 2016), in specific conditions it may add to the sub-inertial flow to re-suspend the fine-grained sediments (*Vitorino et al.*, 2002a; *Xing and Davies*, 2003b). Close to river estuaries and inner-shelf areas, the tidal currents may contribute to the suspension of sediments, in particular during spring tides (*Villacieros-Robineau et al.*, 2013). *Oliveira et al.* (2023) pointed out the importance of internal waves in generating additional turbulence throughout the water column, supporting the formation of suspended material "pockets" in mid-layers (mostly very fine silt, clay) and reinforcing the suspension close to the seabed. *Zhang et al.* (2019) illustrated the role of internal solitary waves in the mid-shelf mud depocenters sediment dynamics.

The biggest sediment sources for the continental shelf areas are rivers. During winter, extremely high values of river run-off in the NW Iberian continental shelf can be observed, particularly from Douro (*Vitorino et al.*, 2002b) and Minho (*Otero et al.*, 2010) Rivers. The coarser fractions are deposited near the river's mouth and transported by the littoral currents driven by waves breaking (littoral drift). The fine sand fractions and silt/clay are transported further offshore as suspended load and can be re-suspended through the action of storm waves, and wind-induced currents. These physical processes induce a differential transport of sand fractions which promotes patches with different sediment particle dimensions along the continental shelf (*Bosnic*, 2017).

The low gradient of the continental shelf off from the Douro estuary facilitates the transport of fine sediments to the deeper areas. Toward the slope a tectonic origin barrier is present, prohibiting the further advection of fine sediment to the deeper part of the ocean and therefore supporting the formation of the Douro mud patch (*Dias et al.*, 2002b). A large amount of sediments from the Douro mud patch and adjacent shelf areas is remobilized and carried Northwards by bottom currents to the Galician mud patch. There occurs three to nine storm in a year (2-13 days per year) that can generate current velocities high enough to re-suspend material within the Douro mud patch (*Vitorino et al.*, 2000). Probably the mean original sediment source for the Galician mud patch was the Minho river. Due to the incentive modification of river regimes, mainly because of the construction of dams, the sediment supply from rivers has reduced significantly during this century (*Dias et al.*, 1980; *Oliveira et al.*, 1982). Fine-grained sediment input from the Galician Rías is small (*Rey*, 1993) due to the morphological features of this area. Rocky outcrops and small islands protect the Rias from large storm events and as they are relatively deep (up to 50 m) they tend to act as sediment traps (*Dias et al.*, 2002b; *Jouanneau et al.*, 2002). Probably the sediments that can reach the shelf are deposited directly into the Galician mud patch. This scenario is supported by the mineralogical data (*Oliveira et al.*, 2002b). Sediment transport further North of the Ría Arosa is greatly reduced due to the presence of rocky outcrops that extend onto the shelf. The morphological features close to the Galician mud patch area are a little bit different than those of the Douro mud patch. There are no physical barriers but the outer slope is much more regular and softer. The sediments re-suspended from the Galician mud patch are probably advected off the shelf to the adjacent oceans. *Dias et al.* (2002a) also compared the different mud patches on the Western European Atlantic Margin and found that the large-scale forcing (storms, swell, bottom currents), common to this area, largely determines the location, as well as the deposition and erosion mechanisms of these mud patches.

Jouanneau et al. (2002) also noted that, in addition to the morphological features influence, the general and seasonal circulation patterns are a big influence on the transport patterns of sediments. In water depths shallower than 100 m frequent mixing and reworking of sediments occurs. With increasing depth the forces acting on the seabed diminish. To re-suspend sediments in greater depths, only less frequently occurring extreme storms can create enough energy onto the seabed (*Vitorino et al.*, 2000; *Jouanneau et al.*, 2002; *Vitorino et al.*, 2002b,b; *Oberle et al.*, 2014; *Villacieros-Robineau*, 2017). These large storm events act as a sorting mechanism leaving behind the coarser factions of sediments (*Dias et al.*, 1980; *Bosnic*, 2017). During autumn and winter seasons downwelling conditions are more frequent promoting sediment transport to the North (*Fiúza et al.*, 1982; *Fiúza*, 1983; *Vitorino*, 1989; *McCave and Omex II partners*, 2000). Whereas summer upwelling periods favour fresh organic input from the ocean to the shelf. In addition, it provokes sediment transport to the South and the ancient ocean through eddies and filaments (*Jouanneau et al.*, 2002).

Villacieros-Robineau (2017) recorded the BBL dynamics during the entire annual cycle from November 2009 to Abril 2010 with a high spatio-temporal resolution at the inner

Galician Shelf. It was found that the wave orbital velocity is the primary mechanism controlling the surface sediment distribution along the margin and the location of the Galician mud patch. Similar conclusions were drawn by the study of *Oberle et al.* (2014). *Zhang et al.* (2016) and *Villacieros-Robineau et al.* (2019) both found that during downwelling season there was little to no export of re-suspended material across the shore to the adjacent ocean. The front created by IPC advected waters and WIBP low saline water, was the key factor determining the extent of cross-shore transport of sediments during energetic events and the location of the mud patch, favouring the sinking of particular matter during low energetic conditions. Re-suspended material was transported northward within the inshore coastal current.

Vitorino et al. (2002a) studied during the spring and winter period the BBL of the Douro mud patch, based on wave buoy and current measurements. For the northern Portuguese shelf, they found that the mean erosion mechanism was wave action. Whereas *Villacieros-Robineau* (2017) and *Zhang et al.* (2016) observed that the co-dominance situations were common and no clear dominance of waves or currents was distinguished.

In the current study, a numerical modelling system was run to simulate a period from November 2008 until December 2009, covering an annual cycle and two distinct winters. The mean goal was to examine the dynamics of current and wave forcing in the sediment re-suspension processes. In addition, to understand the importance of shelf, meso- and submesoscale circulation in the sediment transport processes and mean patterns.

5.2 Methods and data

To study the sediment transport mechanism in the continental shelf of the NW Iberian Peninsula, a three-dimensional free-surface, split-explicit, terrain following Coastal and Regional Ocean COmmunity model (CROCO, v1.0 [1]) was implemented. The model is capable of resolving the coastal dynamics while interacting with a larger oceanic scale. The atmospheric and wave forcing were included using offline sources. The river discharge of the current configuration does not contain sediments. The hydrodynamic model includes a sediment transport module that calculates the movement of sediments through several processes like erosion, suspended load and deposition. It takes into account multiple grain-size classes and includes some of the properties of cohesiveness within the very fine-size classes. In most cases, the bottom-most grid cell is situated too high up from the seafloor to properly resolve the wave boundary layer and here comes to play the BBL module (see section 2.4.3 in Chapter 2). This is to bridge a gap between the different computational needs to characterize hydrodynamics and sediment transport processes. The BBL module is responsible for the calculation of critical shear stresses at the bottom for sediment purposes.

A detailed overview of the numerical models and their set-up for this specific application is presented in Chapter 2. The configuration and validation processes are described in Chapter 4, including a description of the observational data sets in section 4.2.3.

[1] https://www.croco-ocean.org

5.3 Results

5.3.1 Sediment movement along a vertical cross-section

A cross-section on a shelf through a latitude of 42.08°N, close to Cabo Silleiro, will be analyzed, which coincides with the measurement's location (Figure 4.1 in Chapter 4). A brief overview of the time series will be presented highlighting specific events, with certain characteristics that could be observed repetitively. Various large-impact re-suspension events occurred mostly during the winter months of 2008 and 2009. Around 44 events were identified and the role of the currents and waves was analyzed (Figure 5.1).

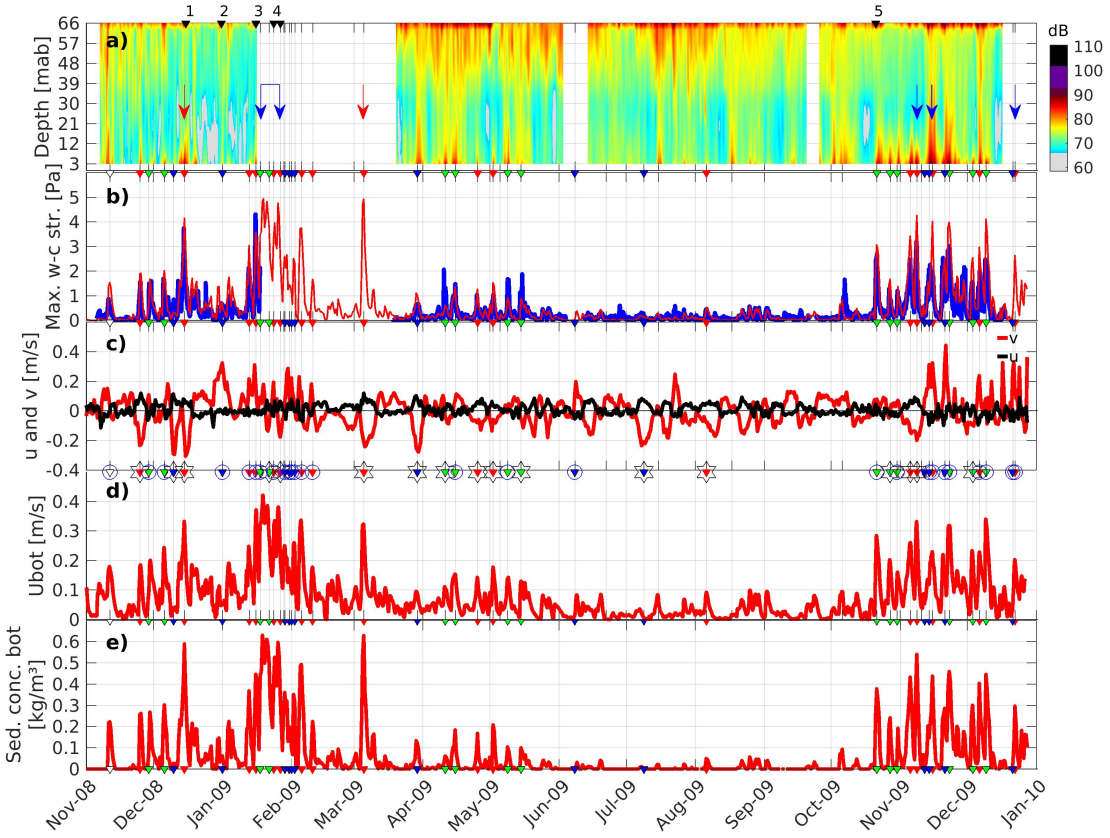

FIGURE 5.1: The information was captured in the ADCP measurements location, with local depth 75 m and in the model 74 m (42.08° N, −8.93° W): a) backscatter signal, red and blue arrows mark the events, where sediment transport rates presented maximums of 0.4 kg/ms and 0.3 kg/ms, respectively; black triangles with numbers indicate the peaks of the events discussed in the results. b) Maximum wave-current shear stress obtained by *Villacieros-Robineau et al.* (2019) (blue) and modelled (red). c) Bottom current velocity components in the alongshore direction v (red) and across-shore direction u (black), hexagram and circle sign the well-developed upwelling or downwelling regime, respectively. d) Wave orbital velocity and e) sediment concentration at the bottom-most grid cell. The blue, green and red triangles represent the current, wave or co-dominance events, respectively.

In this section, there can be found in the initial sediment bed, three types of particle size classes: silt ($< 0.063mm$), very fine ($0.063 - 0.125mm$) and fine sand ($0.125 - 0.250mm$) (Figure 2.2 in Chapter 2).

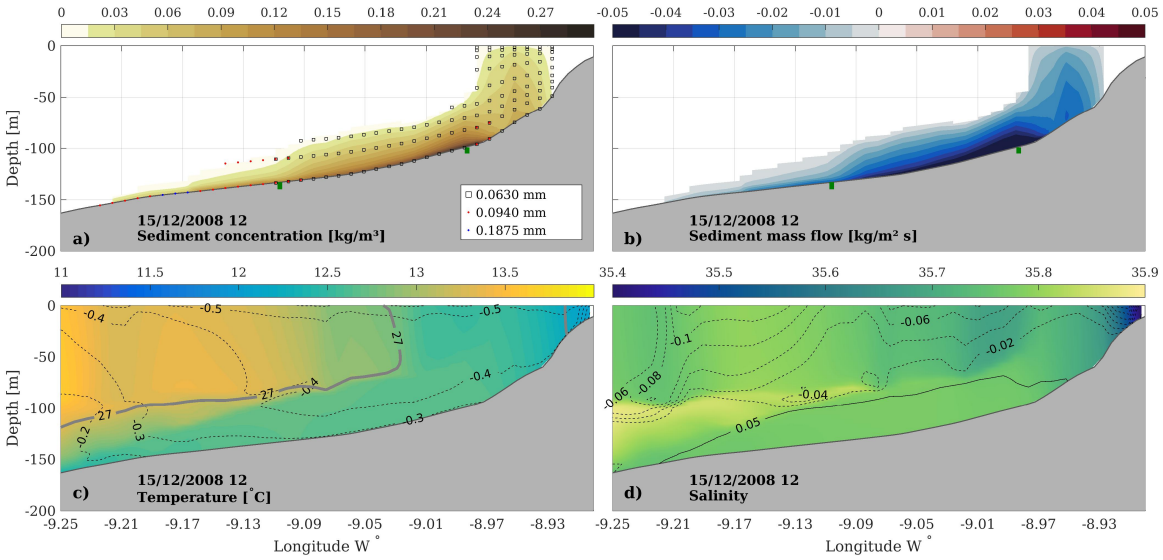

FIGURE 5.2: Co-dominant event and upwelling, December 15th, 2008. The vertical cross view in the Northern area of a) sediment concentration in suspension with scattered particle size information (only concentrations $> 0.001\ kg/m^3$ are shown) and b) sediment mass flow rate in alongshore direction. Green ticks indicate the positions of the finest sediments in the initial surface sediment distribution map. c) Temperature, with contoured alongshore current velocity components in m/s (black), and when possible isopycnal 27.0 kg/m^3 (grey) and 26.0 kg/m^3 (white). d) Salinity, with contoured cross-shore current velocity components in m/s (black). The dotted or continuous black contours on c) and d) represent the negative and positive velocity values relative to the x and y-axis, respectively. Thick continuous black lines show the isotherms and isohalines when needed.

Co-dominant event and upwelling In 2008, the most significant change in the seabed sediments was produced by a co-dominance event, that had its peak on 15 December 2008 with maximum wave-current shear stress around 4 Pa acting on the surface sediments (Figure 5.1 b), event 1). The high bottom shear stress was the product of increasing current and surface wave activity. The bottom currents started to intensify on the night of 14 December, with prevailing direction from North to South, reaching over 0.3 m/s (Figure 5.1 c)), generating upwelling favourable circulation. An intensification could also be seen in the wave field. The simulated significant wave height was 7 m in the wave buoy Cabo Silleiro location (Figure 4.2 Chapter 4). During the peak of the event, wave orbital velocity at the bottom exceeded more than 0.3 m/s at the ADCP measurements location (Figure 5.1 d)).

The silt fraction of sediments was re-suspended high up in the water column along a cross-shore transect off Cabo Silleiro until 100 m water depth (Figure 5.2 a), b)). Very high concentration values at the bottom layers could be observed presenting maximums close to 0.6 kg/m^3 at the bottom-most grid cell (Figure 5.1 e)). Across the whole section transport was directed Southwards, with the highest flow rates close to the seabed, exceeding -0.04 kg/m^2s (Figure 5.2 b)). The temperature and salinity sections (Figure 5.2 c), d)) confirm an upwelling favourable circulation pattern. The 27 kg/m^3 isopycnal (Figure 5.2 c)) separates the deep cold oceanic waters, moving coast-wards with cross-shore current velocity as high as 0.05 m/s, from the warm surface and mid-layer waters, transported oceanward (Figure 5.2 d)). The passing of the storm allowed the sediments to be deposited again, 2 days later, as the concentration levels in the water column reduced close to zero (Figure 5.1 e)).

Current dominant event and downwelling Mainly current-dominated event occurred between 28 December and 2nd of January (Figure 5.1, event 2). Approximately 5 days the currents were strong, with near bottom velocities over 0.2 m/s, flowing Northwards (Figure 5.1 c)). During this period the wave orbital velocity stayed mostly under or close to 0.1 m/s (Figure 5.1 d)). The sediment concentration values at the bottom-most grid cell seem to follow the wave energy impulses, creating peaks of 0.15 kg/m^3 (Figure 5.1 e)).

The section of suspended sediment concentration on 30th December 2008 indicated a presence of a bottom nepheloid layer. The maximum concentration values reach approximately 0.06 kg/m^3 and it was possible to verify the very fine sediment size class in the upper water column (Figure 5.3 a)). The temperature and salinity sections showed a clear downwelling circulation pattern, where the surface warm and saline waters moved towards the coast and cold fresh waters from the rivers entered the shelf (Figure 5.3 c), d)). These conditions created two fronts indicated, with the 27 kg/m^3 isopycnal, that largely seemed to coincide with the limits of the sediments in suspension (Figure 5.3 a), c)). Subsequently, 12 hours later, the fronts had moved further offshore from the coast (Figure 5.4 c)), and the sediment profile continued to be limited by the fronts (Figure 5.4 a)). Decrease in the wave energy, promoted settling of the sediments (Figure 5.1 d)), but, low concentration of sediments $< 0.015 kg/m^3$ continues to be dispersed by the currents (Figure 5.4 a), b)).

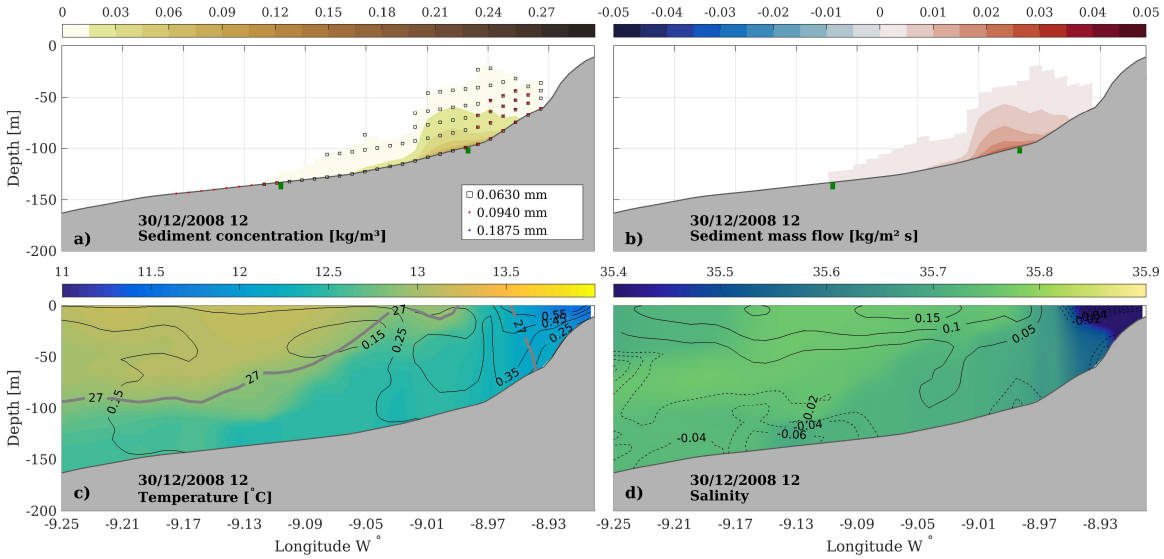

FIGURE 5.3: Current dominant event and downwelling, December 30, 2008. The vertical cross views in the North. Panels explained in Figure 5.2.

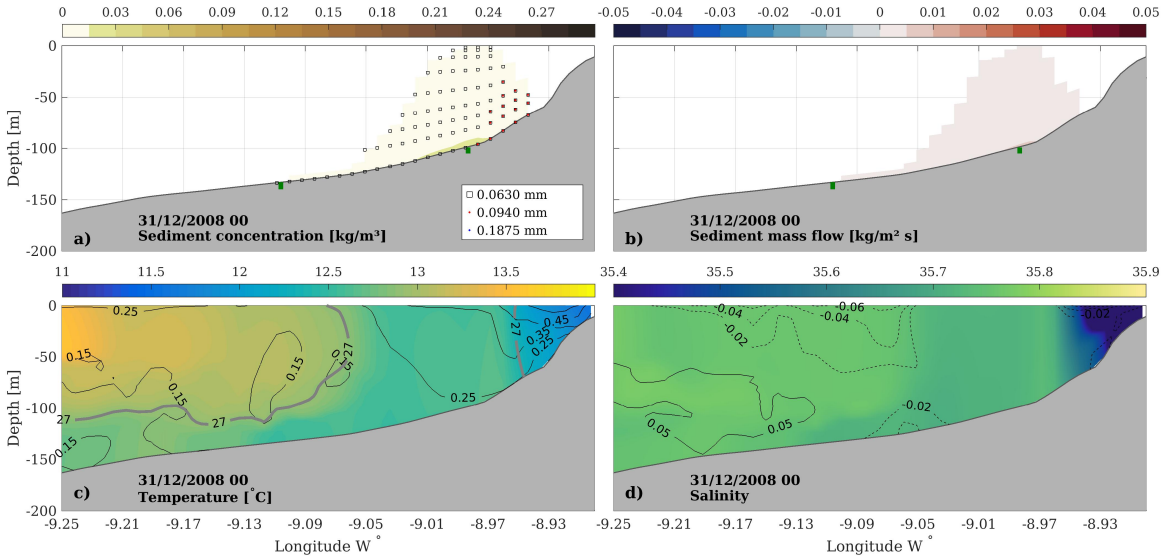

FIGURE 5.4: Current dominant event and downwelling, December 31, 2008. The vertical cross views in the North. Panels explained in Figure 5.2.

At the beginning of 2009, from 13 January until 10th of February, the maximum wave-current induced bottom stress was constantly over 2 *Pa* on the ADCP location (Figure

5.1 b)). This produced a series of re-suspension processes altering between co-, wave or current dominance.

CO-dominant event during downwelling, with a mismatch in the current and wave peaks The third event occurred on January 2009, with the intensification of bottom currents flowing Northward, reaching as high as 0.35 m/s on the 15th at 12 hours (Figure 5.1 c), event 3). On the other hand, wave energy peaked 12 hours later, on the 16th, producing a wave orbital velocity over 0.37 m/s (Figure 5.1 d)), while the bottom currents had reduced to 0.2 m/s at that moment. This mismatch in the peaks of the magnitude of currents and waves had an impact on the profile of sediments in suspension (Figure 5.5 and 5.6 a)). When the current speed was the highest, re-suspended sediments were dispersed along the observed vertical section reaching the surface layers, while concentration values in the upper layers did not exceed 0.015 kg/m^3 at that moment (Figure 5.5 a)). When the wave energy peaked on the 16 of January 00 hour, the sediment concentration at the bottom-most layers increased significantly, from 0.09 kg/m^3 up to 0.3 kg/m^3, while the sediments at the surface layers started to settle (Figure 5.6 a)). Larger sediment mass flow rate values could be observed at the peak of the current along the entire water column, and intensification in the bottom layers during wave peak, due to the higher sediment concentration values (Figure 5.5 and 5.6 b)).

The temperature and salinity sections demonstrated clear downwelling circulation patterns on the 15th, reinforcing the sediment transport to the North and through the bottom nepheloid layer offshore (Figure 5.5 c) and d)). On the 16th, there could be seen a relaxation in the circulation patterns, as the front between the ocean and river waters had dislocated oceanward from its original location and the currents along the water column reduced the intensity (Figure 5.6 c) and d)).

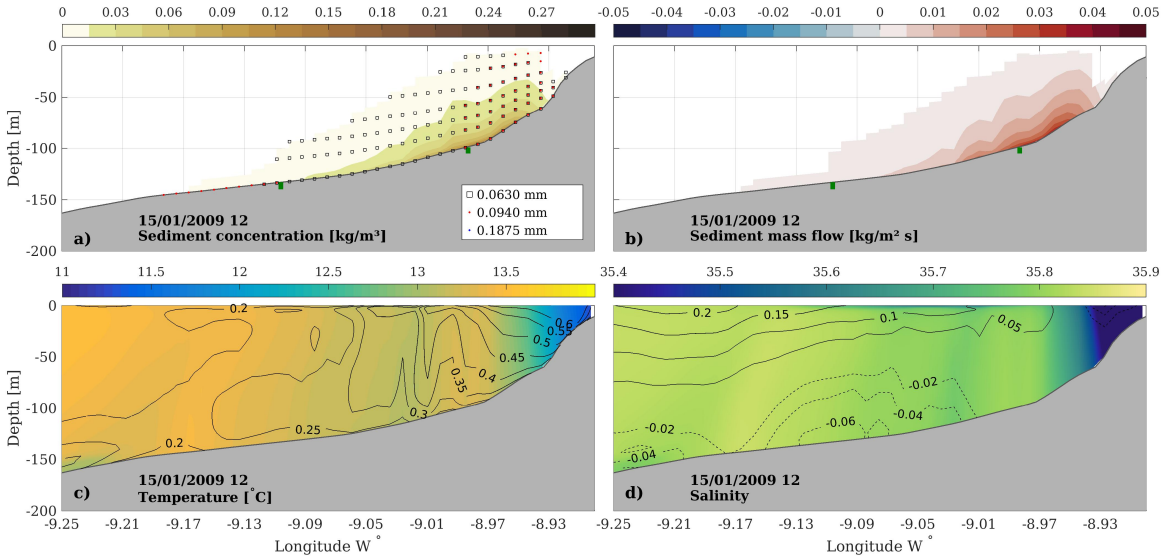

FIGURE 5.5: CO-dominant event during downwelling, with a mismatch in the current and wave peaks, January 15th, 2009. The vertical cross views in the Northern area. Panels explained in Figure 5.2.

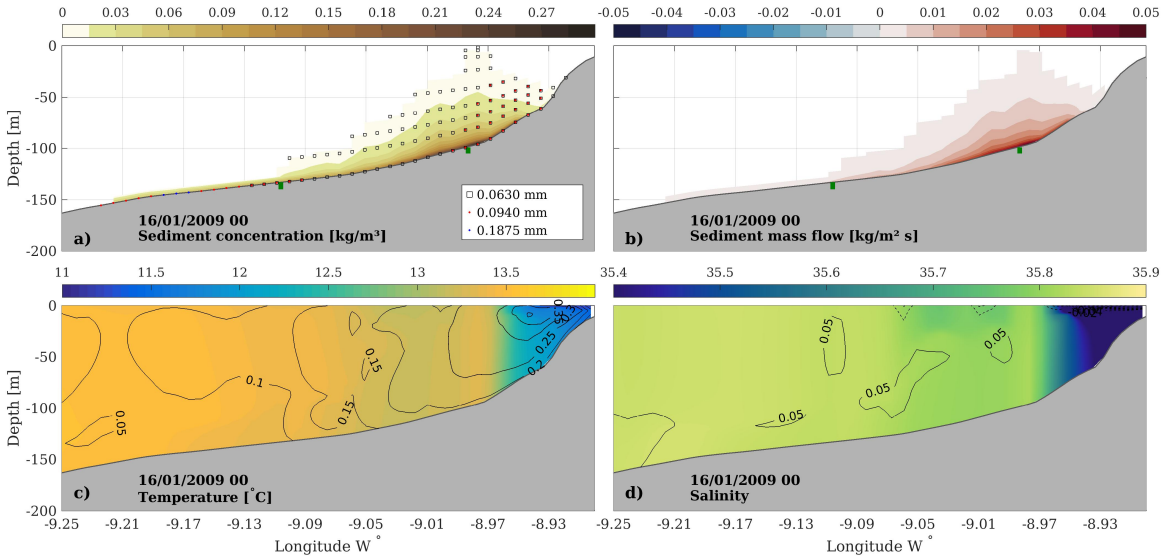

FIGURE 5.6: CO-dominant event during downwelling, with a mismatch in the current and wave peaks, January 16th, 2009. The vertical cross views in the Northern area. Panels explained in Figure 5.2.

Co-dominant event, with a shift in the circulation patterns from downwelling to upwelling Various co-dominance events occurred between 24-27 of January 2009 (Figure 5.1, event 4). On the first day, there could be observed well-established downwelling circulation patterns (Figure 5.7 c) and d)). The flow in the surface layers was directed onshore and at the bottom layers offshore, with maximum values of the cross-shore component reaching -0.08 m/s. The wave orbital velocity had been constantly over 0.2 m/s since the 13 of December and exceeded 0.3 m/s on the 24th. These hydrographic conditions favoured the transport of low concentration of sediments, less than $0.015 kg/m^3$, high up in the water column and their dispersion over a significant area, along the observed section (Figure 5.7 a) and b)). Concentrations above the sediment bed were less than 0.09 kg/m^3, presenting maximums of 0.2 kg/m^3 directly above the bed (Figure 5.1 e)). On the 25th there could be observed a start of a shift in the circulation regime, as the currents weakened and the sediment flow indicated that the currents offshore had already turned Southward, while the sediments in the rest of the water column continued to be transported Northwards (Figure 5.8 b), c) and d)). The next days, wave energy continued to grow, peaking in the ADCP location at 0.37 m/s on the 26th (Figure 5.1 d)), creating a high concentration area of sediment at the bottom-most layers (Figure 5.9 a)). By that time, the alongshore component of current velocity had turned Southward and intensified, demonstrating an upwelling regime. There could be observed a clear correlation between the concentration of suspended sediments, sediment mass flow and current velocity alongshore component v (Figure 5.9 a), b) and c)). An increase in the freshwater input from the rivers can be observed in the salinity field (Figure 5.9 d)), while the front of the WIBP was pushed further in the offshore direction, coinciding largely with the coastward limit of the sediments in re-suspension. On 27/01 00, the post-storm relaxation started and sediments were rapidly settling down and deposited at the seabed.

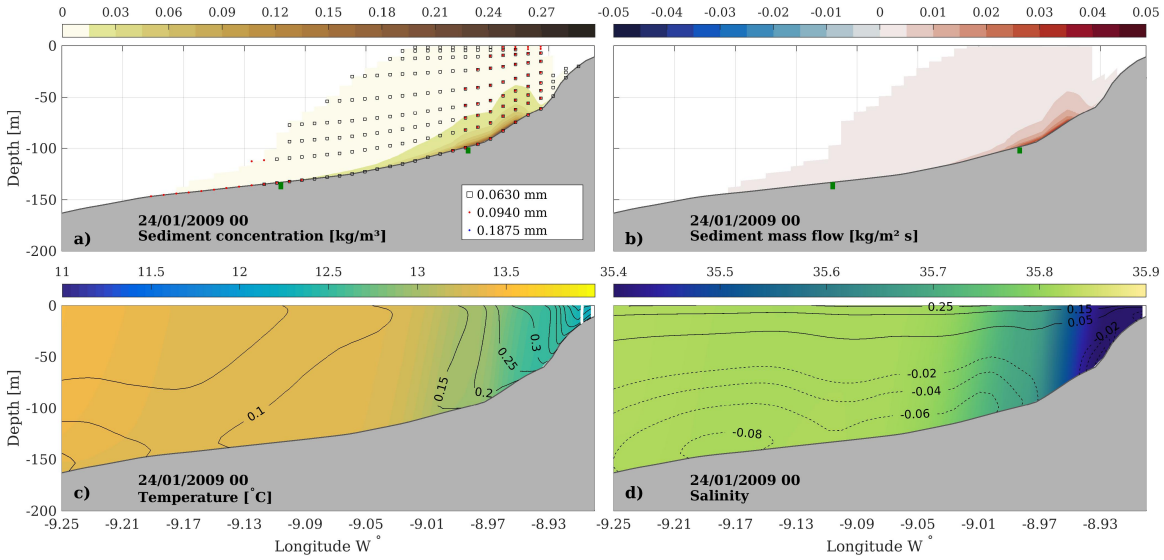

FIGURE 5.7: Co-dominant event, with a shift in the circulation patterns from downwelling to upwelling, January 24th, 2009. The vertical cross views in the Northern area. Panels explained in Figure 5.2.

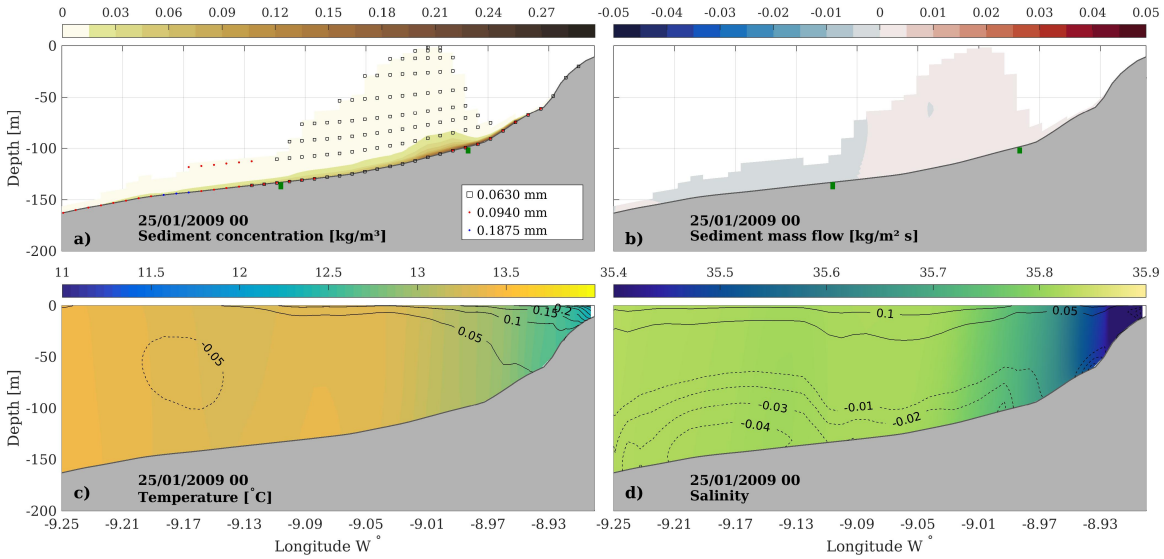

FIGURE 5.8: Co-dominant event, with a shift in the circulation patterns from downwelling to upwelling, January 25th, 2009. The vertical cross views in the Northern area. Panels explained in Figure 5.2.

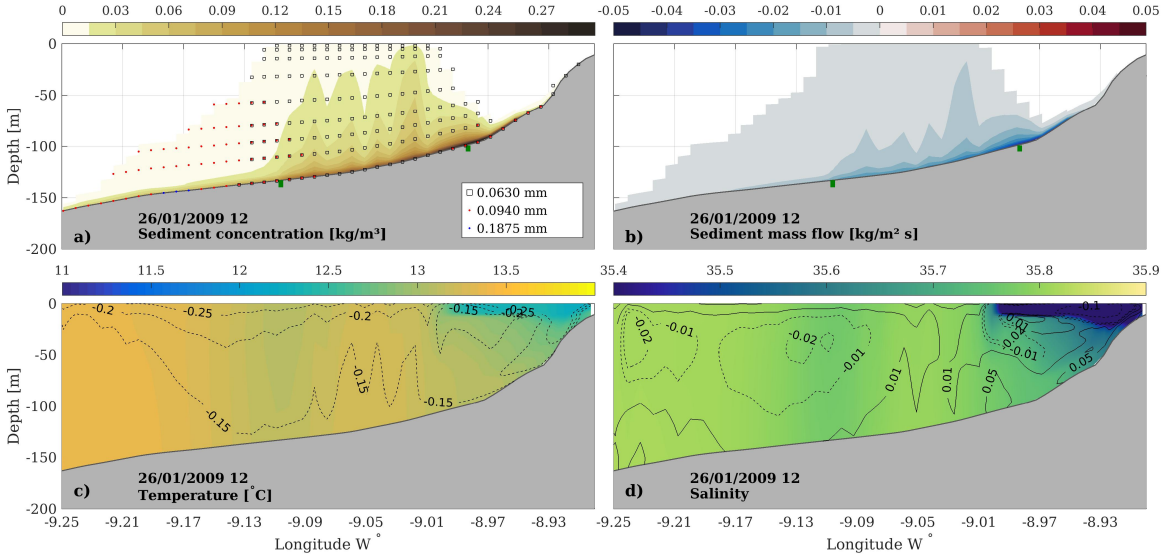

FIGURE 5.9: Co-dominant event, with a shift in the circulation patterns from downwelling to upwelling, January 26th, 2009 at 12 hours. The vertical cross views in the Northern area. Panels are explained in Figure 5.2.

In April and May 2009, there could be observed some sediment movement close to the bottom layers that reduced to a minimum in the summer months, with very rare events re-suspending the sediments more than a few meters above the bed. This continued throughout the early autumn until the middle of October when there could be seen an increase in wave energy.

Wave dominated event During the autumn of 2009, several wave-dominated events occurred. The strongest one happened on 21 of October at 12 hours (Figure 5.1, event 5). The currents were weak, below 0.05 m/s and wave orbital velocity reached 0.3 m/s at the ADCP location (Figure 5.1 c), d)). This created a thin layer of sediment in suspension at the bottom with concentrations maximum close to 0.24 kg/m^3 near the seabed sediments (Figure 5.10 a)). The transport of sediments was principally to the North (Figure 5.10 b)). This event occurred during downwelling, while the water column was strongly stratified at the surface layers. Warm surface waters mixed with fresh water from the rivers were confined to the first 30 m from the surface, separated by the 26 kg/m^3 isopycnal from the colder and more saline waters below (Figure 5.10 c) and d)).

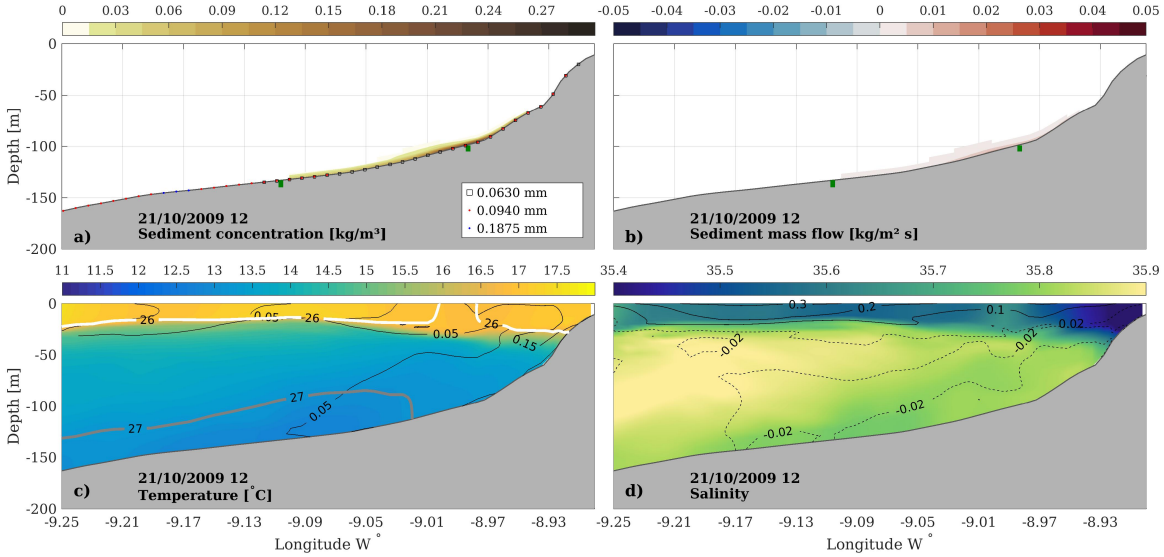

FIGURE 5.10: Wave dominated event, October 21st, 2009. The vertical cross views in the Northern area. Panels explained in Figure 5.2.

5.3.2 The transport of sediment in the water column in North and South of the study domain

The Northern area of the study domain is characterized by a relatively narrow continental shelf and steep slope. The Southern part, on the other hand, has a significantly wider shelf area and a series of narrow steps leading from the shelf break to the adjacent ocean. A vertical profile of a cross-section between $-9.30°W$ and $-8.74°W$ along a latitude of $41.28°N$ was examined (Figure 4.1 in Chapter 4) and its dynamics is compared to the movement in the Northern section, discussed above. In the South, all the sediment size classes are represented in the initial surface sediment distribution map. The coarser fraction dominates in the shallower waters, and with increasing depth, the fine fraction becomes dominant. Rocky outcrops can be found surrounding the Douro mud patch on the outer extent. On the other hand, in the Northern section, only three size classes of the finer fraction are present and rocky outcrops extend from the shore to approximately 60 m depth (Figure 2.2 in Chapter 2).

Comparing several variables of each section approximately in the same water depth (74 m) reveals a similar behaviour in terms of hydrodynamics and sediment response. In the Northern location, the maximum wave-current bottom stress and current velocity components were slightly higher than in the South (Figure 5.11 a), b)). The wave-induced bottom velocity on the other hand was in the same order for both locations (Figure 5.11 c)). A small increase in the sediment concentration values at the bottom-most grid cell could be observed in the Southern point (Figure 5.11 d)).

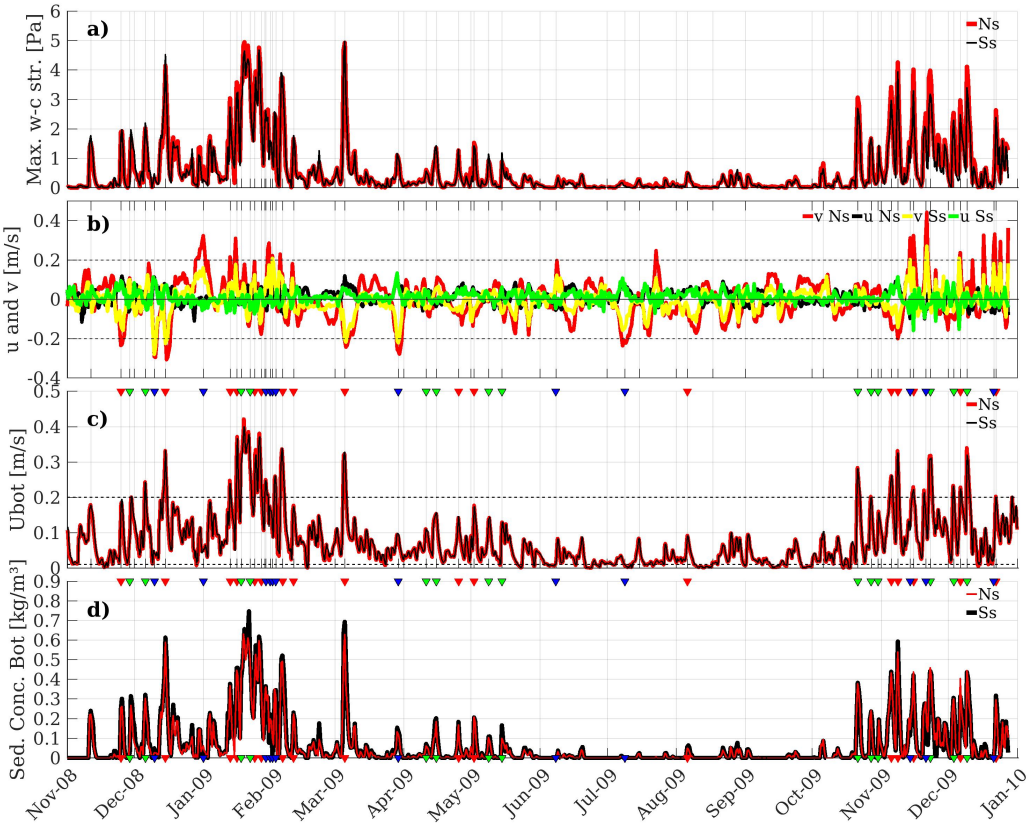

FIGURE 5.11: Time series were obtained from the Northern (Ns) and Southern (Ss) areas of the study site at 74 m depth retrieved from the model (location in Figure 4.1). The following variables were retained: a) maximum wave-current shear stress (red (Ns), black (Ss)), b) near bottom current velocity components v (red (Ns), yellow (Ss)) and u (black (Ns), green (Ss)), c) wave orbital velocity (red (Ns), black (Ss)) and d) sediment concentration at the bottom-most grid cell (red (Ns), black (Ss)). The blue, green and red triangles represent the current, wave or co-dominance events, respectively.

Further analysis demonstrated that in the North the dominant sediment size class in suspension was 0.094 mm and in the South 0.063 mm, presenting similar maximum concentration values, while in some moments a slight enhancement in the Southern section could be observed. Lower concentrations of 0.063 mm and 0.094 mm were present in both locations, respectively, exhibiting slightly higher values in the South (Figure 5.12). In other words, the maximum wave-current bottom stress was slightly higher in the Northern area than in the South, but due to the characteristics of the sediment bed in the observed location, this resulted in higher concentration values in the South.

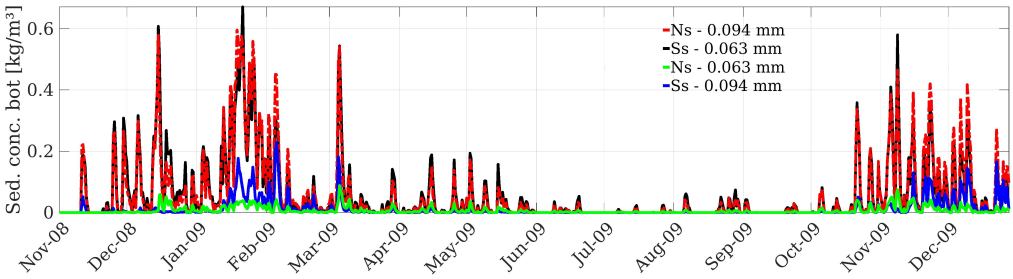

FIGURE 5.12: The sediment size class concentrations for Ns and Ss (location in Figure 4.1) at the bottom-most grid cell.

The strongest re-suspension events observed along the Southern section were aligned with the ones that occurred in the Northern one (Figure 5.11). The area in the vertical section, where sediments can be seen in suspension, was significantly broader on the South compared to the North, as can be seen from the co-dominance event on 15 December 2008 at 12 hours (Figure 5.13). This has to do with the differences in the bathymetric forms of each section. Due to the steep shelf in the North, sediments were re-suspended in an area up to 8 km offshore ($-9.00°W$), where the depth varies from 5 to 104 m in the model, although in rare cases also beyond these limits. In some of the events the sediments also reached the surface layers, but in most cases, the transport occurred in the bottom layers. On the other hand, in the South, the seabed slopes more gradually and sediments were moved along in a much wider area until 26 km offshore ($-9.10°W$) from the coast. In this section, depth varies from 5 to 120 m.

During summer months it could be observed that, along the Southern section, at the bottom-most layers the sediments were re-suspended from time to time whereas the same was not observed for the North.

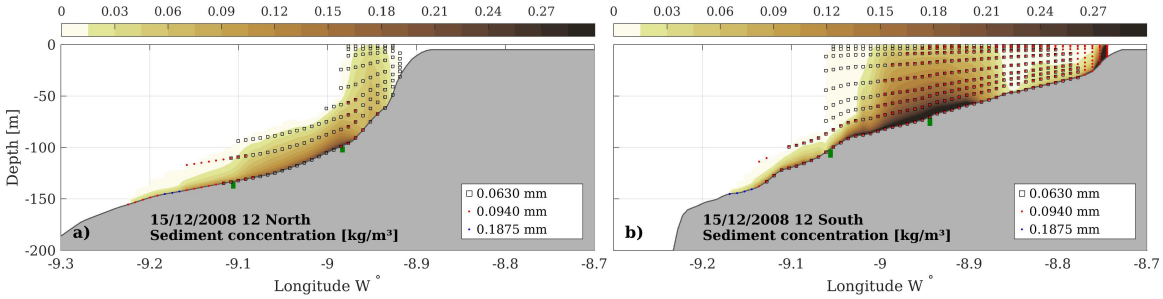

FIGURE 5.13: a) Cross-sections in North and b) South, on December 15th, 2008. The vertical cross view of sediment concentration in suspension with scattered particle size information (only concentrations $> 0.1 mg/l$ are shown). Green lines indicate the positions of the finest sediments in the initial surface sediment distribution map.

5.3.3 Sediment transport on the shelf

Events with very high sediment transport rates

During the modelled period, there occurred 6 events where the transport flux exceeded 0.3 kg/ms in some areas of the shelf (Figure 5.1 a), indicates the incident dates). Two of the events happened during upwelling in the first half of the observed period (14-16 December 2008, 05-06 March 2009), creating very high sediment transport rates, exceeding 0.4 kg/ms. The remaining events (20-27 January 2009, 8 and 15 November 2009, and 22 December 2009) demonstrated transport rates close to 0.3 kg/ms, during which there could be observed both upwelling and downwelling. In all the cases a co-dominance of waves and currents was identified.

The meso- and submesoscale circulation

Of the 44 previously identified events, 17 of them occurred during downwelling and 27 during upwelling conditions.

Upwelling driven sediment transport On the 4th of March 2009 at 12, the height of the waves started to increase and reached a peak on the 5th with 6-8 m waves from NW, approaching the coast in depths > 70 m (Figure 5.14 a)). The wave orbital velocity exceeded 0.14 m/s well beyond 90 m depth and a significant amount of sediments were re-suspended from the seafloor all across the shelf (Figure 5.15 a)). At the same time, also currents intensified at the bottom layers, presenting the highest velocities in the inner and mid-shelf, and in the outer shelf North from 42.2 °N, with maximums over 0.2 m/s, flowing Southward (Figure 5.14 b)). An increased sediment transport flow could be seen in the mid-shelf below 70 m depth across the layer 5 mab, reaching over 0.8 kg/ms (Figure 5.15 b)).

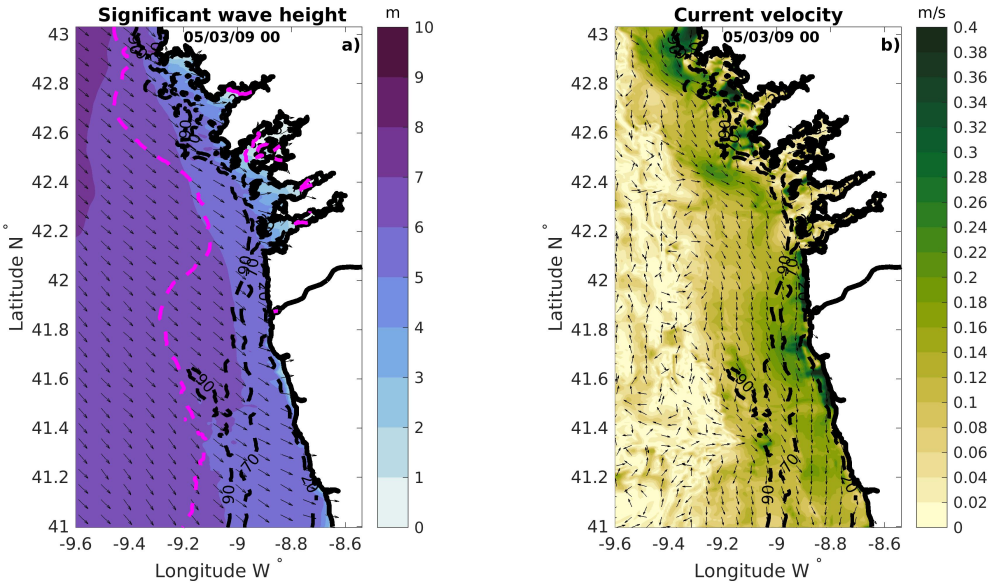

FIGURE 5.14: March 5th, 2009. a) The significant wave height and wave peak direction. The dis-continued magenta line represents the 0.14 m/s isopleth of the bottom wave orbital velocity. b) The current velocity and direction at the bottom layers.

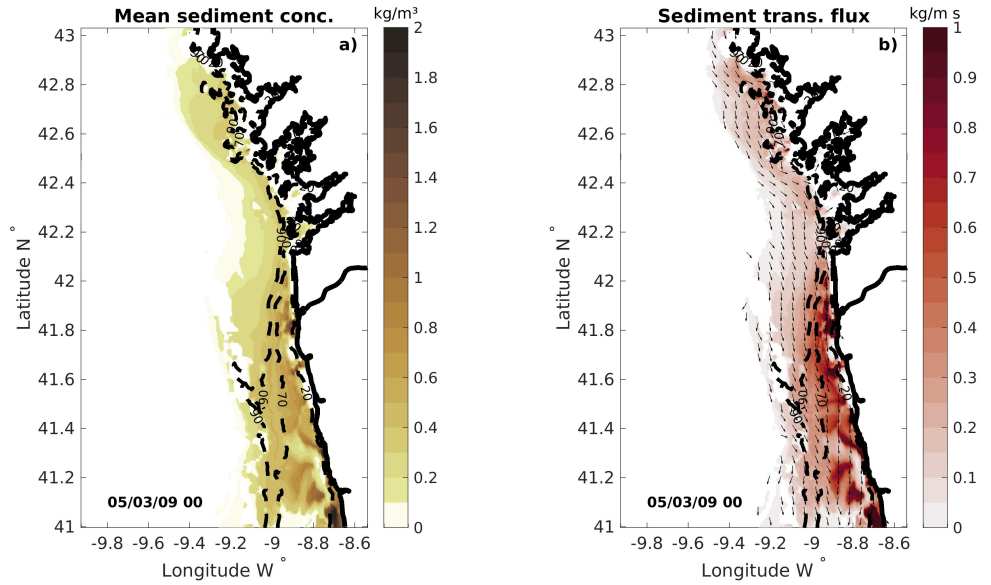

FIGURE 5.15: March 5th, 2009. a) The mean concentration of suspended sediments across a layer with a thickness of 5 mab. b) Sediment transport flux in the bottom-most 5 m.

Sediments along the Northern and Southern cross-sections were carried high up to the water column and even reached the surface layers (Figures 5.16 a) and 5.17 a)). There could be observed a strong Southward movement of sediments across the whole water column in both locations (Figures 5.16 b) and 5.17 b)). The temperature and salinity sections confirm the upwelling circulation patterns across the shelf, indicating propagation of colder and more saline water coastward along the bottom layers (Figures 5.16 and 5.17, c), d)). There could be observed an increased freshwater input from the Xallas, Tambre, Ulla, and Umia rivers in the North and from Minho and Douro in the South, on the 3rd of March. With upwelling favourable winds, these waters were pushed Southward, giving an origin to these freshwater patches in the surface layers reaching up to 50 m depth, seen from the salinity section (Figures 5.16 and 5.17 d)). Well-defined fronts developed between the saline oceanic water and the fresh water at the surface layers, marked with 37.5 isohaline in the Southern section (Figure 5.17 d)), seem to confine and restrict the suspended sediment dispersion in the water column. The fronts also coincide largely with the borders of the areas where sediments could be seen in suspension in the water column (5.17 a), b)).

With a decreasing wave height, after the peak of the storm, the deposition patterns started to dominate as confirmed by the decreasing sediment concentration values at the bottom (Figure 5.1 d), e)). The upwelling-driven circulation continued to stay relatively strong, promoting the transport of previously re-suspended sediments Southwards (Figure 5.1 c)). Even 4 days later, after the peak of the storm, there could be observed a sediment transport at the bottom layers. A similar event occurred on December 15 2008, but the sediment settled to the bed after 2 days due to the difference in the circulation intensity.

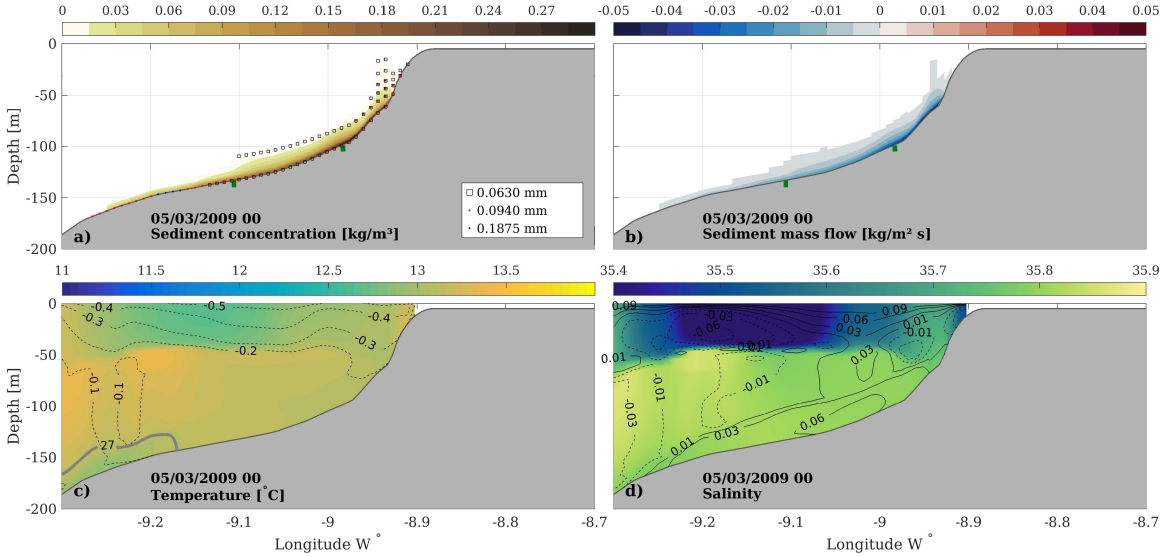

FIGURE 5.16: Cross-sections in North, on March 5th, 2009. Panels explained in Figure 5.2.

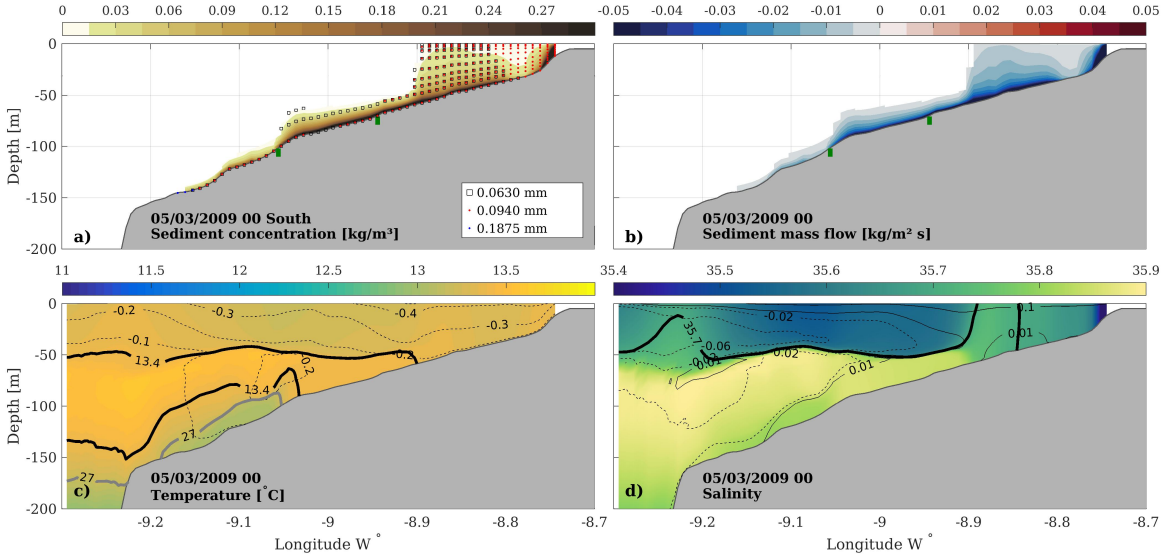

FIGURE 5.17: March 5, 2009, cross-sections in South, on March 5th, 2009. Panels explained in Figure 5.2.

Downwelling driven sediment transport On the 12th of November 2009, the ocean circulation shifted from upwelling to downwelling and the currents at the bottom layers intensified, reaching the first peak on the 14th and the second peak on the 15th of November. In both dates, the current velocity along-shore component v exceeded 0.3 m/s (Figure 5.1 c)). At the same time, waves started to grow, travelling from SW and the maximum significant wave height varied between 5-6 m (Figure 5.18 a)), which coincided with the current second peak. Across a large part of the shelf, the current velocity at the bottom layers exceeded 0.2 m/s, presenting maximums over 0.3 m/s. These oceanographic settings lead to high mean sediment concentration values in a layer of 5 m from the sediment bed, exceeding 1 kg/m^3 in the mid-shelf and reached up to 0.2 kg/m^3 in the outer shelf (Figure 5.19 a)). Elevated sediment transport flow rates were seen all over the shelf, reaching in some areas over 1 kg/ms (Figure 5.19 b)).

The cross-section in North and South demonstrated clear downwelling-driven circulation patterns. The along-shore current component v was directed Northwards across the entire water column up to approximately 150 m water depth, with a counter-current in the surface layers deepest area (Figure 5.20 and 5.21 c)). Cross-shore current component u indicated a coastward flow of warmer and less saline water in the surface layers, and an oceanward flow of colder and more saline water at the bottom (Figure 5.20 and 5.21 d)). The sediment concentration and sediment mass flow profiles indicate a strong influence of the fronts on the propagation of the sediments, both in the Northern and Southern regions (Figure 5.20 and 5.21 a), b)). Water mass in the bottom layers, separated by the 13.7 $°C$ and 15 $°C$ isotherms, and 35.7 and 35.8 isohalines in the Northern and Southern sections, respectively (Figures 5.20 and 5.21 c), d)), limit the sediment movement in the mid-shelf.

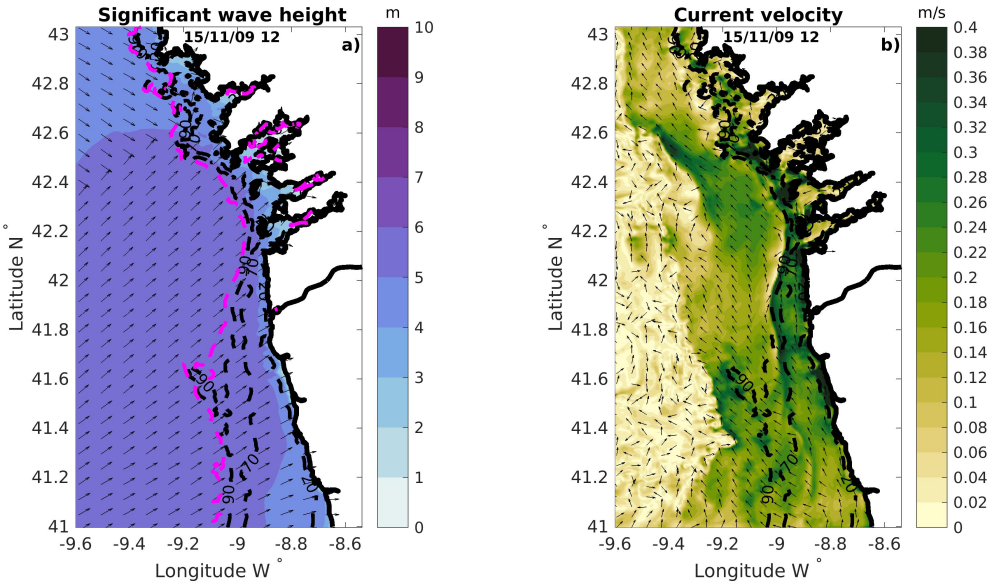

FIGURE 5.18: November 15th, 2009. a) Significant wave height and wave peak direction. The dis-continued magenta line shows the 0.14 m/s isopleth of the bottom wave orbital velocity. b) Current velocity and direction at the bottom layers.

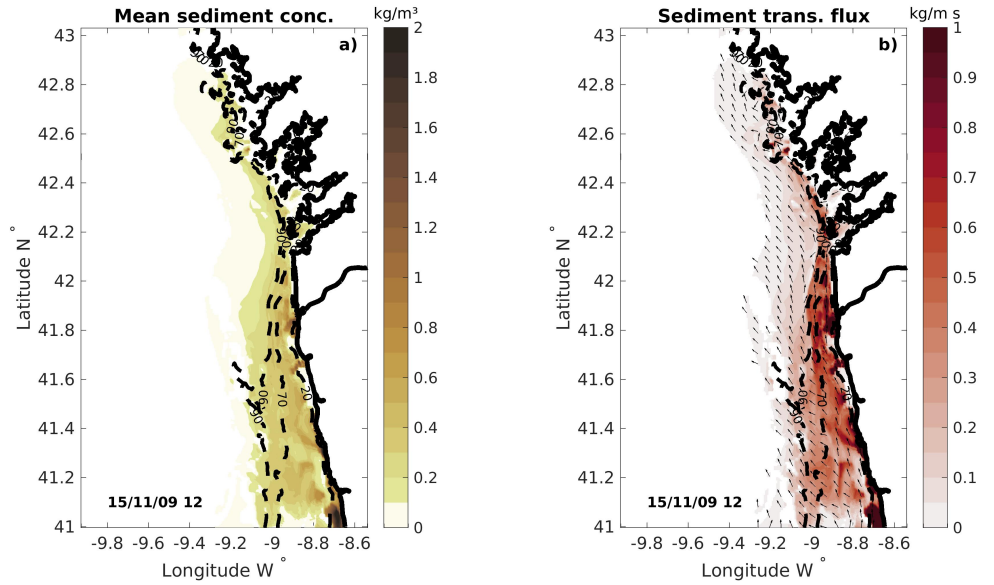

FIGURE 5.19: November 15, 2009. a) Mean concentration of suspended sediments across a layer with a thickness of 5 mab. b) Sediment transport flux in the bottom-most 5 m.

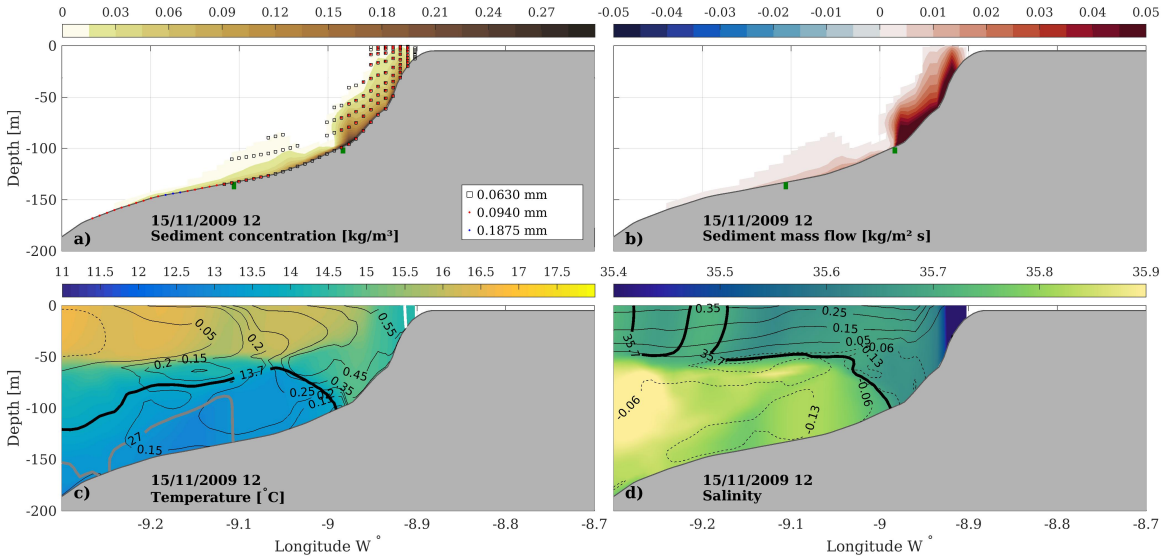

FIGURE 5.20: Cross-sections in North, on November 15th, 2009. Panels are explained in Figure 5.2.

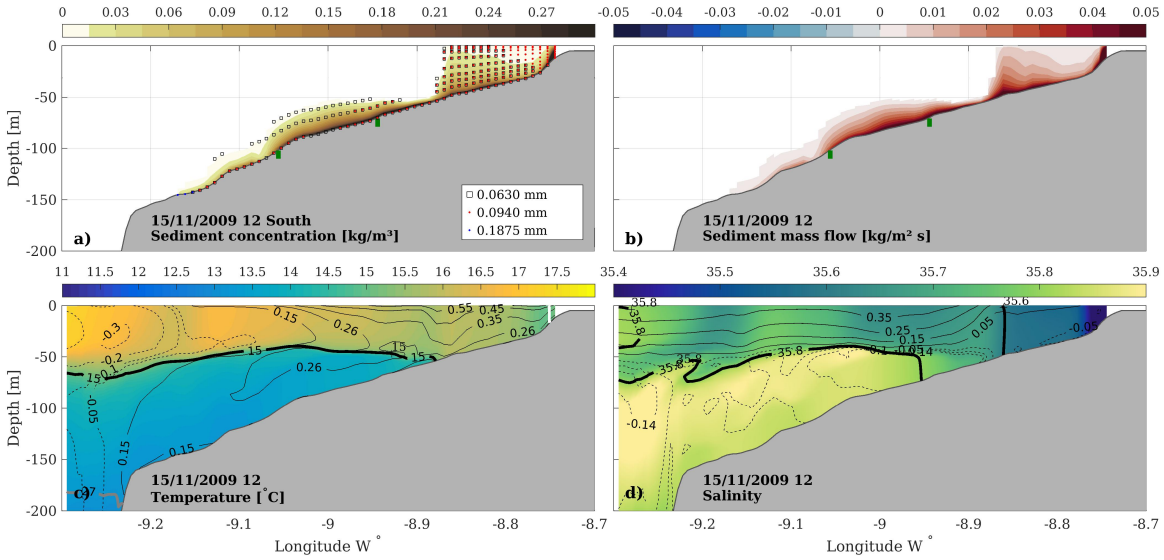

FIGURE 5.21: Cross-sections in South, on November 15th, 2009. Panels are explained in Figure 5.2.

Changes in the seabed sediments

The most significant changes in the seafloor sediments were particularly evident in the large-impact events, marked on Figure 5.1 a) with arrows. However, when significant wave height approached 5 m on the outer or middle shelf and currents at the bottom exceeded 0.1 m/s, there could be observed changes at the sediment bed over 1 mm. With less energetic conditions the bed remained almost unchanged or the changes produced were below 1 mm. Clear tendencies of erosion or deposition patterns were present with the evolution of the storms. The sediments were removed from the seabed while the storms reached their peaks and deposited again afterwards.

The highest sediment transport rates, associated with upwelling events, occurred on 15 December 2008 and 5th of March 2009, demonstrating relatively similar tendencies when it came to changes in the sediment bed (Figure 5.22). The erosion patterns were mainly evident in depths greater than 90 m in the Galician mud patch region and greater than 70 m in the Douro mud patch area. The deposition occurred in areas shallower than 70 m and South from 41.2°N. The duration and the amplitudes of the peaks of both of the events were comparatively alike (Figure Figure 5.1 b)), resulting in deposition and erosion maximums of 6 cm and -10 cm in some areas on the shelf seabed.

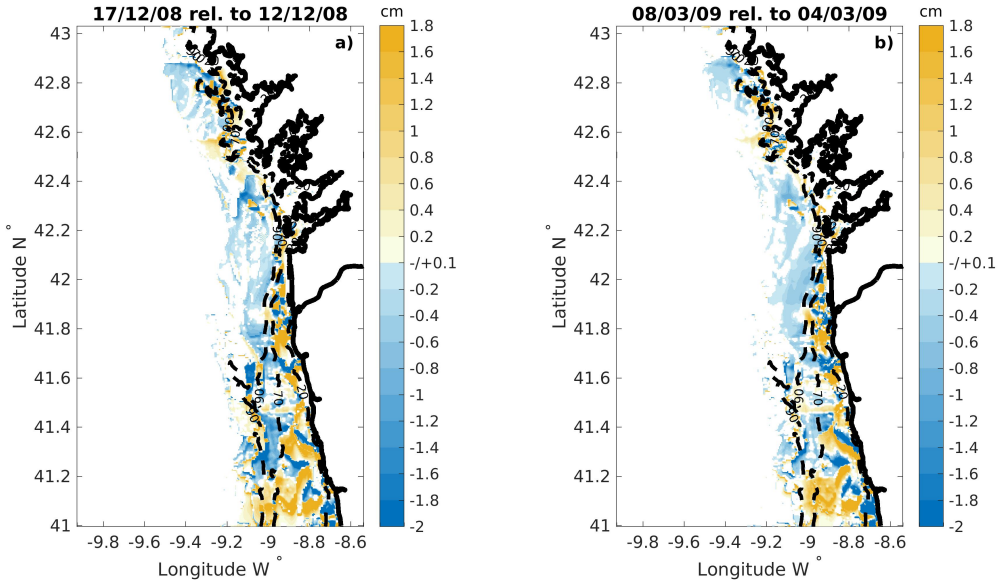

FIGURE 5.22: Changes in the seabed sediments after the a) 15th of December 2008 and b) 5th of March 2009 event.

Changes caused by the downwelling events were more notable during the last two months, at the end of 2009. Frequent downwelling favourable circulation could be seen on the shelf (Figure 5.1 c)). During this period, various energetic wave episodes took place and the collective oceanographic settings produced notable changes in the seabed sediments. These were most evident on the 15 of November and on the 22 of December. By the end

of the November event (Figure 5.23 a)), the sediments were deposited in the outer shelf beyond or close to 90 m depth contour North from the 41.6°N latitude line. South from there, the deposition could also be observed in depths in the region of 70 m. Erosion took place mostly in depths below 70 m. In December (Figure 5.23 b)), the deposition and erosion patterns created patches across the shelf up to 90 m depth. During both of these events the common denominators were the well-established downwelling circulation regime, the amplitudes of the peaks of the current along-shore component at the bottom layers and wave orbital velocity (Figure 5.1 c), d)), demonstrating very close values, approximately 0.33 m/s and 0.2 m/s, respectively. A considerable difference was in the duration of the events. The November event lasted roughly 6 days, maintaining the peak values for a day and a half. On the other hand, the December event endured for 3 days and the peak of the velocity of the bottom currents was 12 hours before the wave peak. This produced significant differences in the maximum values of the bed changes, with accumulation rates of 4.5 cm and erosion rates of -5 cm in the November event. In December the maximums of deposition varied between 4.5 cm below 20 m depth and 1.5 cm beyond, and erosion rates up to -2 cm. Nevertheless, some similar tendencies in the deposition and erosion patterns could be seen during both events.

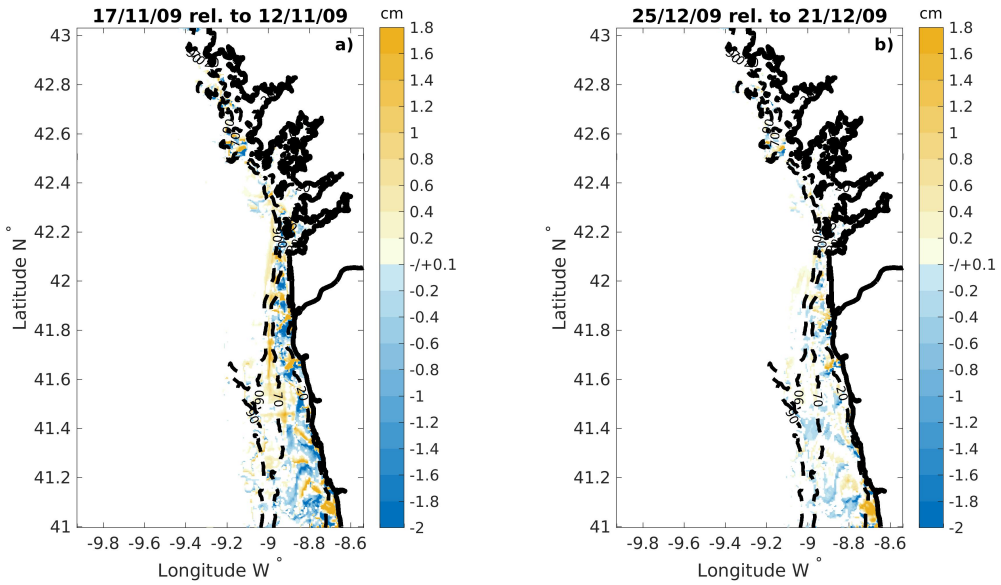

FIGURE 5.23: Changes in the seabed sediments after the a) 15th of November 2009 and b) 22th of December 2009 event.

5.4 Discussion

5.4.1 Sediment dynamics in the inner, middle and outer shelf

The continental shelf margin can be divided into three distinct zones: inner-, middle- and outer shelf, based on the grain size distribution and the hydrodynamic regime. The inner shelf most landward area covers the wave-breaking zone and it is characterized by frequent exchange of littoral sediments with a sub-aerial beach which translates into measurable morphological changes. The seaward inner shelf limit can be determined by the presence of finer littoral sediments, that are frequently mobilized but mostly transported under highly energetic events. The middle shelf feels less wave energy at the bottom and constituents of medium and coarse sand fractions. In this zone the re-mobilization of sediments is dominant, but the net transport is relatively low. The muddy sediments mark the end of the middle and the beginning of the outer shelf. Here the hydrodynamic regime is milder and the finer fraction can settle (*Bosnic*, 2017).

Based on the initial grain size distribution of sediment in the study area, the approximate depth distribution is as follows. The inner shelf lies between 0-20 meters, the middle shelf from 20 to 70-90 meters and the outer shelf starts from 70 meters in the Douro mud patch location and at 90 meters in the Galician mud patch.

The model results indeed showed that in the inner shelf area, the sediments were most frequently in suspension and with the highest mean transport rates in a 5 m layer above the bed. In the middle shelf, a frequent re-mobilization of sediments could be observed, but the mean transport rates stayed mostly very low, less than 0.02 kg/ms. Only, in the presence of currents sufficiently strong to transport sediments, can there be seen an increase in the transport rates. Nevertheless, during energetic events, the transport rates in the middle shelf exceeded 0.3 kg/ms in some locations.

On the outer shelf, the sediments were re-mobilized and transported the least. This only happened with certain hydrodynamic conditions. Sediments were re-suspended and presented mean concentration values higher than 0.15 kg/m^3 in a 5 m layer above the bed when wave orbital velocity reached 0.14 m/s or higher. *Villacieros-Robineau et al.* (2019) found this to be the threshold of hydrodynamic stability for muddy sediments. A statistical value characterizing the average impact of all the storms during the observed period, with a percentile of 95 %. The model simulations of the present study demonstrated that in a single event with wave orbital values as low as 0.06 m/s, the waves were able to re-mobilize the finest fractions of sediments in the deeper end of the shelf. Generally, waves with a significant wave height of 4-5 m were able to create sufficient shear stress at the bottom to re-suspend sediments on the outer shelf. During the modelled period, there were several episodes where the sediments were re-suspended from the bottom due to the high energetic wave event, but the transport flux were minimum (less than 0.02 kg/ms) as the currents in the bottom layers were weak (smaller than 0.1 m/s). Also, opposite situations could be observed, where the current speed exceeded 0.4 m/s, but waves did not have enough energy to suspend sediments in the outer shelf, again resulting in low transport rates.

Due to the sediment size differences in the continental shelf, the current speed necessary to transport sediments was smaller on the outer shelf compared to the mid-shelf.

5.4.2 The key forcing factors of sediment transport

Across the whole shelf, most commonly co-dominance situations occurred presenting approximately 39 % of the 44 distinguished events during the observed period. Followed by wave dominance, with 32 % and also not unusual were current dominated events, with 29 %. Current dominated events always coincided with notable wave activity with lower energy and *vice versa*. It was not possible to distinguish any differences in the roles of waves and currents for the Northern and Southern areas of the study site. Similar conclusions were drawn by *Zhang et al.* (2016) and *Villacieros-Robineau* (2017).

The sediments' movement along a cross-shore section demonstrated well the effects of currents and waves in the re-suspension and transport of sediments. With only current-dominated events, the suspended sediment concentration values at the bottom layers were notably smaller than with only wave or co-dominance situations. Therefore, the wave action promoted the re-suspension of sediments from the seabed and currents moved the sediments further off from the source. The timing and intensity of oceanographic settings had a great impact on the sediment movement dynamics. A mismatch in the intensity peaks of waves and currents reduced the co-dominance impact and therefore the action of each was less effective. In the presence of suspended sediments in the water column, low current velocity, with a constant change in the flow direction, allowed to continue to transport sediments and slowed down the settling processes. Possibly, the turbulence that was created from the shifts in the circulation regime enhanced the transport mechanisms.

As noted by other authors e.g. *Dias et al.* (2002a); *Vitorino et al.* (2002a) morphological features greatly influence the fine-grained sediment movement and accumulation on the shelf. This was also seen from the model results when observing the Northern and Southern areas of the shelf. Due to the difference in shelf-slope gradients, in the South, sediments were transported in a wider area than in the North. Consequently, a more frequent re-mobilization of sediment in the Douro mud patch could be observed compared to the Galician one.

Throughout the 14 months, there occurred 6 storms which had a remarkable impact in redistributing the sediments on the shelf. The effect of this was also seen in the Douro and Galician mud patches. All of these large-scale storms took place during winter months, except one early spring storm. A frequent reworking of sediments was observed between the mud depocenters and the coast, depths below 90 m. Among others, similar observations were also done by *Vitorino et al.* (2000); *Jouanneau et al.* (2002); *Vitorino et al.* (2002a,b); *Oberle et al.* (2014); *Villacieros-Robineau* (2017), about the impact of storms on the surface sediments.

5.4.3 Suspended sediment transport patterns

Seasonal influence

The seasonal impact on the movement of sediments indicates a major impact of large-scale forcing like storms, waves and bottom currents in shaping the sediment transport patterns. During late spring, summer and early autumn, there was little to no movement in the seabed sediments. Whereas, with the increase in the intensity of the waves and currents, significant mixing and reworking of sediments could be observed.

Shelf circulation

Upwelling and biogenic input to the shelf are favoured during the summer period (*Jouanneau et al.*, 2002) and stormy periods promote downwelling, with the mean direction of transport of the sediments to the North (*McCave and Omex II partners*, 2000). During the observed period, the events highlighted in this study that took place during storm seasons were mainly upwelling-dominated, constituting 61 % of the total occurrences. While the sediments were re-suspended from the seabed to the water column, and in the presence of strong downwelling conditions, the sediment transport was mostly Northward directed (limited to the NW sector) and promoting the offshore transport of sediments in the BBL (Figure 5.19 b)). On the other hand, with upwelling, the transport was mainly Southwards (limited to the SE sector) and associated with an onshore transport through the BBL (Figure 5.15 b)).

The impacts on the sediment bed in the event of upwelling or downwelling were distinct. While sediments were mostly removed from the outer shelf areas and accumulated onto the mid-shelf during upwelling, the opposite occurred during downwelling. Erosion was largely dominant in the mid-self, although in some cases also in the Douro mud patch location. Deposition of sediments was predominant in the outer shelf areas. The duration of a particular storm, and also the timing of the wave and current energy peaks created a significant difference in the long-lasting impact of a particular event. The seasonal circulation patterns give an insight into the mean sediment transport patterns (e.g. winter downwelling, summer upwelling). On the other hand, a large-scale storm may generate a significant change in the sediment bed, reworking the sediment bed and leaving a lasting signature of the event.

In the study conducted by *Zhang et al.* (2016), during a downwelling event, there could be seen a significant deposition of mud patches on the outer shelf. Although very similar patterns were observed in the current study, deposition of sediment beyond the shoreward boundary of the Galician mud patch was not detected. This may be largely due to the characteristics of the seafloor surface sediments described in the model. Only the sand fractions were considered and the aggregate-forming properties of clay and silt fractions were for the most part neglected. Another contributing factor may be the unavailability of observational data sets to calibrate more efficiently the sediment model.

In winter periods, a well-established circulation regime could change fast and be replaced by another well-developed one. During these rapid shifts, the sediments were transported toward the coast when downwelling changed to upwelling and towards the slope with a change from upwelling to downwelling. While there was sediment in suspension, the shifts in the circulation seemed to enhance the turbulence in the water column, promoting the levitation of sediments.

Bottom eddies and density fronts

Often there could be observed bottom eddies form across the shelf, more frequently and clearer off from the Galician rivers in depths greater than 90 m. During a well-established circulation regime (upwelling or downwelling), that frequently coincided with a strong wave energy event in the winter period, the eddies that were formed, mostly transported the sediments to the direction of the mean circulation, South- or Northward on the shelf. This was due to the positioning of the eddy in terms of depth distribution. A part of the eddy that was located in the shallower area, where sediments were in suspension, followed the circulation patterns. On the other hand, the counter-current of the eddy was in the deeper part of the shelf, with a limited supply of sediments in the water column (Figure 5.24). When the circulation patterns were not fully developed or the shift from one well-established regime to another was progressive, the circulation in the near-bottom eddies generally tended to be weaker in strength. If there existed sediments in suspension in the water column, these eddies would form the pathways of transport toward the adjacent oceans (Figure 5.25).

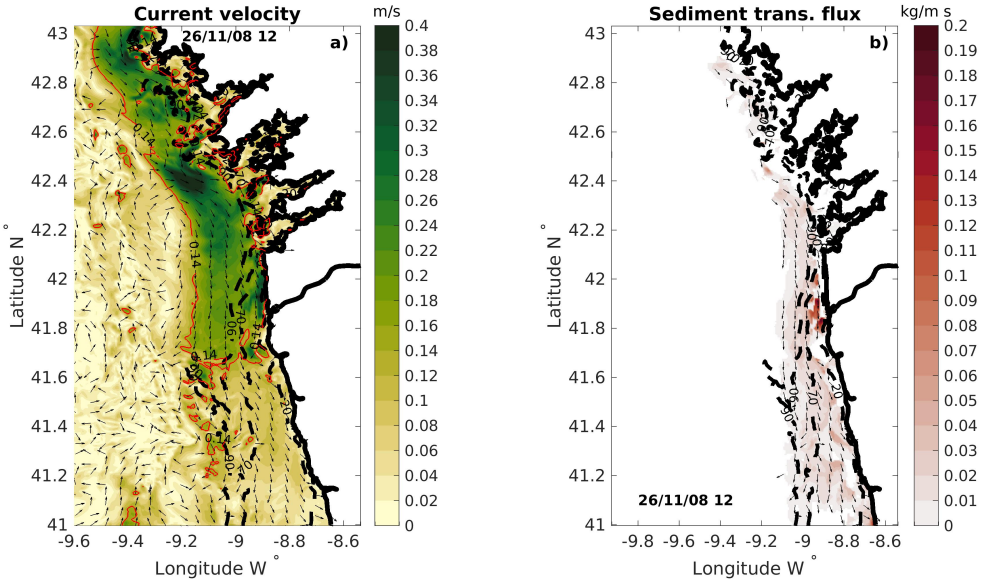

FIGURE 5.24: November 26th, 2008, a well-established upwelling event. a) The current velocity and direction at the bottom layers. b) Sediment transport flux in the bottom-most 5 m.

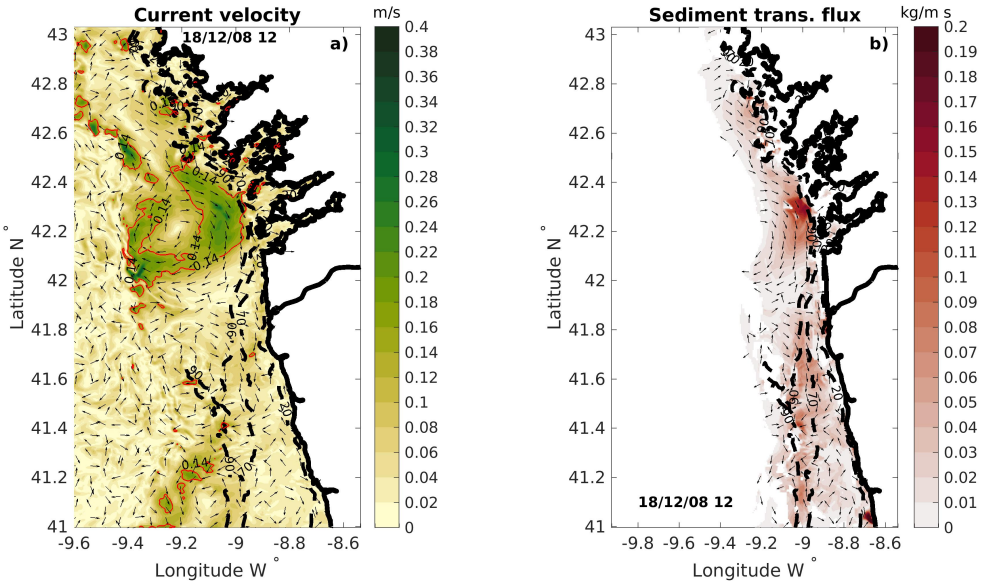

FIGURE 5.25: December 18th, a shift from upwelling to downwelling. a) The current velocity and direction at the bottom layers. b) Sediment transport flux in the bottom-most 5 m.

Density fronts between the fresh water from the rivers and saline oceanic waters creating the WIBP can restrict the sediment movement in the shoreward end of the shelf. It was also possible to observe this restrictive nature of the surface layers front in the mid-shelf, impeding the suspended sediments from being suspended higher up to the water column. The storm-generated downwelling fronts observed during this period coincided largely with the shoreward boundary of both of the mud patches found in the study area, confirming the conclusion drawn in the *Zhang et al.* (2016) study.

5.5 Conclusion

The fundamental processes in the seasonal dynamics of sediment movement in the continental shelf were reasonably presented in this study. While considering the simplification and generalizations made by the numerical models, the influence of morphological features, the effect of seasonal and general circulation, and the impact of waves and storms on sediment transport patterns were all described.

It was found that suspended sediment transport in the NW Iberian shelf was largely controlled by the combination of the current and wave co-dominance effects. While the shelf circulation patterns, influenced by the seasonality, determine the mean direction of the transport. The magnitude of wave energy acting onto the seabed sediments regulated the amount of sediment mass that would be re-suspended.

The storm-driven upwelling and downwelling events promote the Southward and Northward transport of sediments. Big storms were able to erode sediments in the outer shelf

and upwelling favoured the deposition of sediments in the mid- and inner shelf. On the other hand, downwelling favoured the accumulation of sediments close to or on the outer shelf. Single large-scale storms observed mainly during the winter periods, had a great impact in re-distributing the seafloor sediments compared to the potential of the mean transport tendencies of a particular season (upwelling or downwelling).

The density fronts in the water column limited and controlled the horizontal and vertical movement of sediment in the water column. The fronts created during storm-driven downwelling coincided largely with the shoreward limits of the mud patches. Restricting the movement beyond its shoreward and eventually supporting the formation of these depocenters.

The cross-shore transport of suspended sediments in the Southern part of the study site was bound by the morphological characters of the seabed. Whereas, in the Northern area there could be seen forming large-scale bottom eddies, and open pathways to the re-suspended sediment transport to the open ocean.

Chapter 6

The fate of sediments coming from the river systems

6.1 Introduction

The origin of sediment basin and bed features of the NW Iberian continental shelf date back to the last glacial maximum. Since then, the mean sea level has increased drastically, leaving a part of the continent under the water. Additionally, the changing climate and oceanographic settings, laid the foundation to form the seabed as we know it today (*Dias et al.*, 1997). There are presently two large deposits of fine sediments in the study site, the Douro one in the South and the Galicia one in the North (Chapter 2 Figure 2.2, areas with the finest fraction). Douro mud patch has been deposited over strata of Paleocene and Eocene age (*Dias et al.*, 2002a) and the observations indicate that the sediments at 3.1 m depth date back to 1400 B.P. Similarly to Douro, Galician mud patch is considered a recent sedimentary feature (*Drago et al.*, 1994) and consists of 2 to 6 m thick sandy and muddy Quaternary sediments (*Rey*, 1993; *González-Álvarez et al.*, 2005).

Both mud patches are orientated from North to South (*Jouanneau et al.*, 2002). The Douro mud patch is about 8-18 km wide and 42 km long and located at a depth of 90-120 m Northwest at the mouth of the Douro River. The Galicia mud patch is about 2-3 km wide to 50 km long, located at a depth of 110-120 m further North of the Minho estuary. For the most part, the sediments within these patches are fine-grained, though slightly coarser in the Galicia patch (*Dias et al.*, 2002a).

The N-S and W-E directional variations in both of the mud patches are described in detail in *Jouanneau et al.* (2002). Around 100 m depth contour the N-S directional variations in the sedimentation rates were found to be higher off the Douro Estuary in the Southern sector and near the Galician Rias to the North.

According to *Jouanneau et al.* (2002) the sedimentation rates vary between 0.17-0.58 cm/yr in different locations in the Douro mud patch and Galicia between 0.06 and 0.21 cm/yr. Nevertheless, the outer reaches of the Southern region of the shelf are relatively poor in recent sediments. There can be seen features related to the ancient coastlines and river mouth, as well as relict sediments. The Northern area, on the other hand, is covered with a thin layer of fine-grained material (*Dias et al.*, 2002b). These differences can be explained by the mechanism controlling the development of these mud patches, including

the terrestrial supply of sediments to the shelf, favourable hydrodynamic conditions and morphological features promoting the accumulation of sediments. During this century, the anthropological influence and construction of dams have significantly reduced the mean input of river sediment supply (*Dias et al.*, 1980; *Oliveira et al.*, 1982). The most relevant rivers in this region, providing the terrestrial sediments to the shelf, are Minho and Douro. During flood events, fine sediments are transported to the inner and sometimes to the mid-shelf, staying relatively close to their source. The coarser fraction stays behind, and it is transported Southwards through littoral drift. The finer fractions from different rivers become mixed. Most often, the re-suspended finer fraction gets trapped by the poleward current on the continental shelf (*Villacieros-Robineau*, 2017; *Jouanneau et al.*, 2002; *Vitorino et al.*, 2002b,a).

The morphology plays a crucial role in the dispersal and deposition of fine sediment onto the shelf. The continental shelf in the Northern area of the study site has rocky outcrops and small islands in the shallower region of the shelf (*Dias et al.*, 2002a). These features shelter the Rias, which are quite deep, up to 50 m, capturing the sediments coming from this region's river systems (*Jouanneau et al.*, 2002). A strong depth gradient leads to the outer shelf, where the Galician mud patch is located. The outer shelf is relatively soft and regular, without any physical barriers, so sediments may be transported into the ocean. In the Southern location, the shelf is gentle. A tectonic origin barrier is present at the far end of it, restricting further movement of sediments to the adjacent ocean (*Dias et al.*, 2002b).

The studies about the formation and development of the seabed, along with the movement of fine-grained sediments on the shelf, have further raised questions about the suspended sediment transport and the evolution of the mud patches on the shelf under the current climate. The fate of the sediment entering the shelf from the river systems is still poorly understood. This is due to the lack of long-term observational data sets, regarding the quantity and the specific characters of the particulate matter. So, this is the first attempt to understand the course of action of the material coming from the river systems exploiting numerical models and universal formulations.

6.2 Methods and data

6.2.1 Set-up of the modelling system

A three-dimensional numerical model CROCO (v1.0) was used to simulate the transport of the particulate matter coming from the rivers. The configuration of the model was based on the previous study, presented in Chapter 5, about the role of driving forces in sediment transport processes. The model set-up is described in great detail in Chapter 2 and the validation process in Chapter 4. In the present study, further modifications to the source code of CROCO were done. So, the model would also consider sediment concentration information along with the river discharge. For more details about the changes in the source code, consult Appendix B.

In general, there exists little to no information about the sediment concentration values transported by the various rivers in the NW Iberian region. Therefore estimates of sediment flow were calculated following the formulation presented in *Franz et al.* (2014).

$$Q_s = 0.0043 \times Q^{1.45} \tag{6.1}$$

where Q_s (kg/s) is the total suspended sediment flow and Q (m^3/s) the river discharge. A concentration was found as:

$$Q_s = Q \times C => C = \frac{Q_s}{Q} \tag{6.2}$$

In terms of river flow capacities, the most important rivers in the study area are Minho and Douro. The properties of the sediments entering the ocean from these river systems are not very well known. There are limited observational data available, covering very short periods. According to the study of *Santos* (2021), the sediments belong to a silt fraction class, varying between 0.016 - 0.032 mm, and are mostly transported in the upper layer of the water column when the river discharge is strong. Based on the estimates in the previously mentioned study, the model is set up in a way that all 11 rivers in the study area carry sediments only when the river discharge exceeds 100 m^3/s. While this limit was set even higher for the Douro, > 500 m^3/s, as with lower values, due to the shape of the estuary and its inner circulation, sediments get trapped. All the names and locations of the rivers can be seen in Figure 6.1 a).

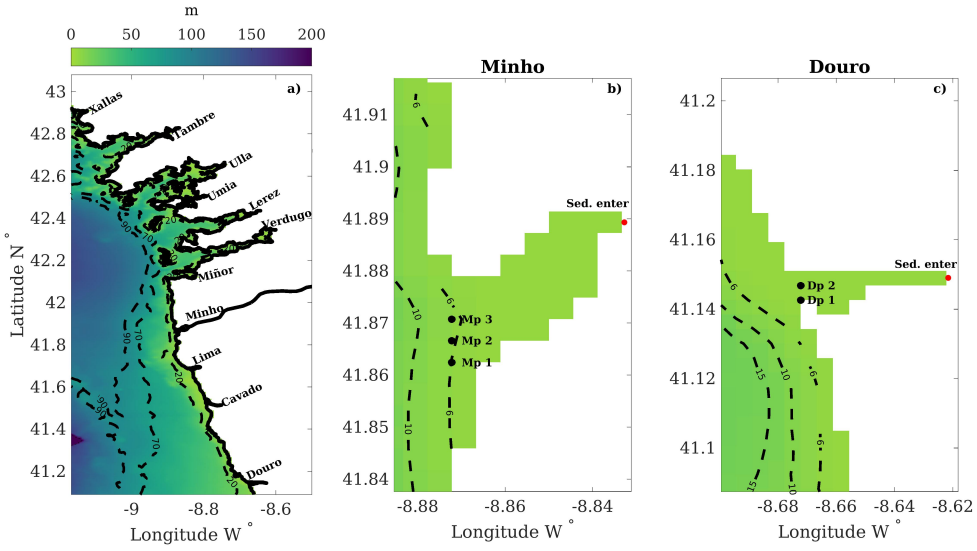

FIGURE 6.1: a) Locations and names of all the rivers included in the simulation. b), c) Estuaries of Minho and Douro, respectively, with Mp 1-3 and Dp 1-2 indicating the points, where the mean sediment concentrations were estimated in Figure 6.2 c) and e). The red dots represent the sediment concentration entry point.

Based on the mean daily river flow and the net sediment flux data presented in *Santos* (2021) for 9 March 2006 in Minho and 7 March 2006 in the Douro, estimates of sediment concentration were calculated closest to the river inlets (Equation 6.2). For Minho, the approximate sediment concentration value was 4 mg/l, with a daily mean river flow of 557.4 m^3/s and sediment flux 100x10$^3 kg$ during 12.6 h. For Douro 8 mg/l, with a daily mean river flow of 569.25 m^3/s and sediment flux 200x10$^3 kg$ during 12.4 h. These values were used as rough approximations of the order of magnitude of sediment concentration while adjusting the model setup.

In the initial configuration, 8 different size classes of sediments were present, each with inherent properties (see Chapter 2 Table 2.1). At first, the rivers would transport the two finest sediment fractions, silt and very fine sand ($D_{50} < 0.063$ mm and 0.0940 mm). After various tests, it was found that the modelled concentration values at the entrance of the Douro and Minho rivers were too high compared to the above-referred estimates. Therefore, two additional size classes were added to the model configuration, with D_{50} 0.032 mm and 0.016 mm. These sediments were only transported by the rivers and not placed on the sediment bed. The settling velocity, erosion rate and critical shear stress were calculated based on the recommended formulation in the model manual (Table 6.1, information about the formulations is in Appendix A). This lowered significantly the concentration values, as the sediments moved further away from the river inlet, instead of being deposited near the entrance of the river outlet. Additionally, the point of entry on the computational grid, where the sediment concentration values were introduced, was moved more inland. Pushing the boundary point further away from the area of interest reduces the so-called boundary effect (Figure 6.1 b) and c)).

The two additional sediment classes added to the model, silt 1 and silt 2, demonstrated similar transport patterns. As the silt 1 fraction was with smaller D_{50}, lower settling velocity and critical stress, it could be seen dispersed further from the input source (Table 6.1). In many cases, the second fraction, silt 2, was deposited in the mouth of the estuary or stayed inside the river. Therefore, hereon, only the smaller fraction, silt 1, will be described and discussed.

TABLE 6.1: Mean grain size classes entering the shelf from the river systems, represented by D_{50}, $w_{s,m}$ - settling velocity, E_0 - erosion rate and τ_{ce} - critical shear stress for sediment motion (suspended load).

	D_{50} (mm)	$w_{s,m}$ (mm/s)	E_0 $(kg/m^2 s)$	τ_{ce} (N/m)
1) Silt 1	0.016	0.1611	6.6 10^{-05}	0.0552
2) Silt 2	0.032	0.6442	1.4 10^{-04}	0.0859

In this simulation, the properties of the sediments entering the shelf through river systems were modified according to which behaviour was expected, based on some rough estimates and the general knowledge from the literature. This is due to a lack of measurement data available and the modelling system does not have a module capable of representing the cohesive behaviour of the silt fraction. Therefore, some caution should

be taken while interpreting the results. This is considered as a first try in understanding better the kind of observational data needed and which are the technical requirements of the numerical model, to obtain satisfactory results.

6.3 Results

6.3.1 River runoff and sediments

During the observed 14-month period of simulation, the most energetic conditions on the shelf occurred from November 2008 until the beginning of March 2009 and again from October 2009. This was seen from the maximum wave-current induced shear stress (Figure 6.2 a)). Similar tendencies could be observed from the river runoff data from Minho and Douro (Figure 6.2 b), d) blue line).

Due to the set-up of the model, the Minho River transported more frequently sediments in its river flow, than the Douro. The sediment concentration values were estimated based on the river discharge (Equation 6.2) and limited to specific flow conditions that were set based on the recommendations in the literature. Minho River would only transport sediments when the discharge was equal to or higher than 100 m^3/s. These conditions were met almost always, so the sediment concentration that was imposed in the model varied between 20-60 mg/l and presented maximum values around 100 mg/l during the highest river flow (Figure 6.2 b) red circles). Douro river runoff, on the other hand, exceeded the criteria 500 m^3/s only during approximately 5 months out of the whole observed period. Within, the sediment concentration levels were always above 60 mg/l, while the highest values reached close to 160 mg/l (Figure 6.2 d) red circles). All the rest of the rivers hardly ever met the criteria of 100 m^3/s, therefore the sediment input from these can be considered trivial in the current application. The mean sediment concentration levels leaving the estuary close to the mouth of the rivers varied significantly (Figure 6.2 c) and e)). For the river Minho, at the end of January throughout February 2009, the concentration maximums rounded close to 2-3 mg/l, while the river runoff maintained over 500 m^3/s, with the maximum reaching approximately 1400 m^3/s (Figure 6.2 b) and c)). This order of magnitude was also estimated by *Santos* (2021), rounding to 4 mg/l, with a mean river flow of 569.25 m^3/s. At the end of 2009, from mid-November until December, there were two distinct peaks on 15 November and 22 December, with greater maximums of 8 and 13 mg/l, respectively. At the same time, river runoff maintained similar values compared to the previous winter, while varying around 500 m^3/s, with maximums close to 1000 m^3/s. During autumn, spring and summer the mean sediment concentration levels remained close to 0, although the river discharge continued to carry sediments.

In the case of the Douro River (Figure 6.2 d) and e)), from December 2008 until January 2009, the mean concentration varied between 1-4 mg/l. From the end of January until the beginning of March 2009, these values increased considerably, with maximum peaks around 14 mg/l. During this period, the river runoff maintained over 1000 $m^{3/s}$, with maximums around 1500 $m^{3/s}$. Thereon, the concentration levels dropped, maintaining close to 1-2

mg/l throughout spring, summer and autumn seasons, except for one event in April. Only increasing again in the middle of November 2009 until the end of the year, exhibiting peaks between 6-10 mg/l in the mean sediment concentration values. River runoff presented even higher maximums, 2700 $m^{3/s}$, compared to the beginning of the year. Mostly, these values were in the same order of magnitude as proposed by *Santos* (2021), with a mean river flow of 569.25 m^3/s and a concentration of 8 mg/l.

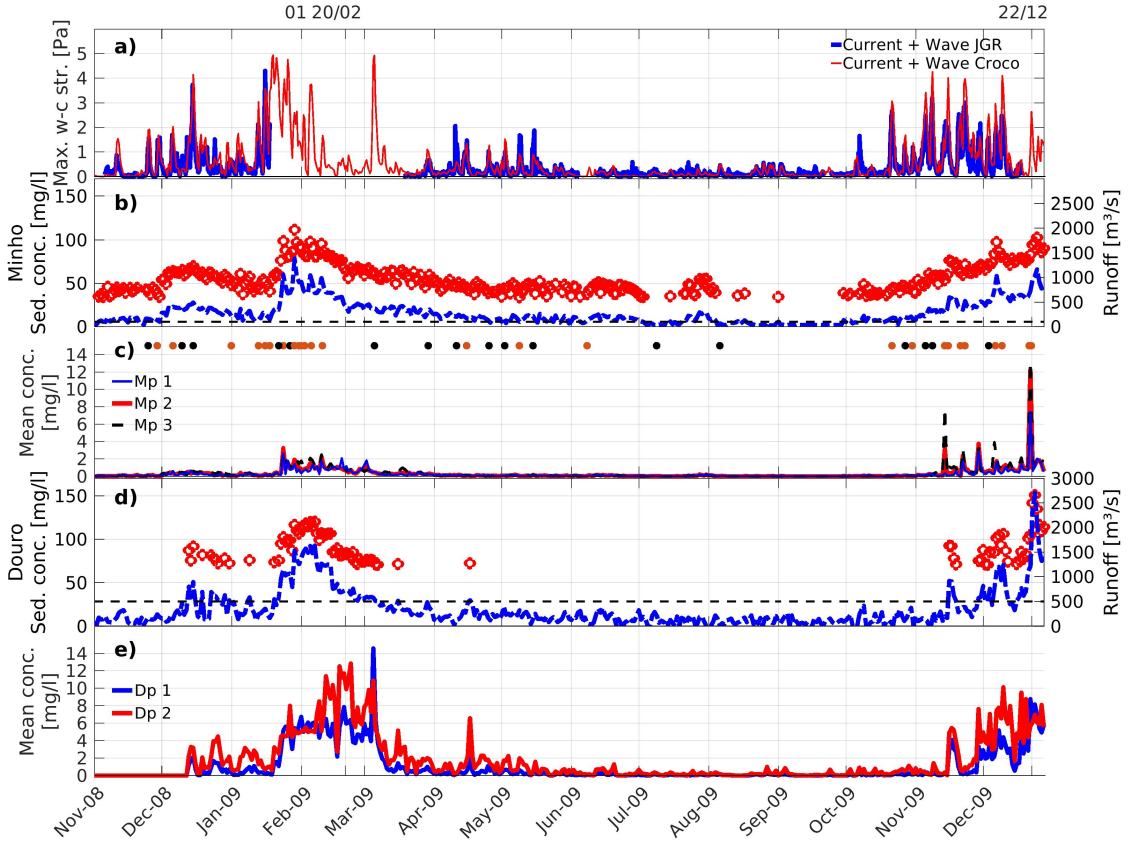

FIGURE 6.2: a) Maximum wave-current shear stress obtained by Villacieros-Robineau et al. (2019) (JGR) at the ADCP measurements location (42.08° N, −8.93° W, with local depth 75 m and simulated by the CROCO model. b), d) River runoff (blue discontinuous line) and the sediment concentration values (red circles) imposed in the intrusion point of the river estuaries of Minho and Douro, respectively. The horizontal dashed black line indicates the threshold from which sediments were released into the system. c), e) The mean sediment concentrations along the entire water column close to the river mouths of Minho and Douro, respectively. The exact locations of these points can be seen in Figure 6.1 b) and c). The black and orange dots in c) indicate an upwelling or downwelling-driven circulation on the shelf, based on the data presented in Chapter 5 Figure 5.1.

At the beginning of 2009, from January 24 until March 20, the suspended sediment concentration remained high in the mouth of the Douro estuary. While from 23/01 - 14/02 the river runoff was over 1500 m^3/s, decreasing after that and varying between 855 - 500

m^3/s from 15/02 - 07/03 (Figure 6.2 d)). The opposite could be seen in points Dp 1-2 close to the Douro River entrance. There was an increase in the sediment concentration values, while the sediment input and river runoff decreased (Figure 6.2 e)). Generally, this was more evident in the Northern point, Dp 2, though the storm event on March 5th created a strong peak in both points.

6.3.2 Oceanographic conditions

Downwelling driven storm

The end of January 2009 and February were distinguished by persistent high wave energy conditions and strong river discharge (Figure 6.2 a), b) and d)). There could be seen well-developed upwelling or downwelling-driven circulation patterns, such as the downwelling event on the 1st of February 2009. At the peak of the event, the maximum mean sediment concentration at the bottom layers, right off of the Minho River outlet, was close to 21 mg/l (Figure 6.3 a)). These values reduced significantly and fast with distance from the coast, presenting a strong concentration gradient, remaining below 5 mg/l beyond the 20 m depth contour. On the other hand, concentration remained high, in the range of 15 mg/l, in the coastal zone depths below 10 m and diminished with a distance from the river source. Very close to the coastline, North of Douro estuary, the mean suspended sediment concentration exceeded 33 mg/l. It continued high in depths below 10 m, up to river Cavado, with minimums ranging around 15 mg/l. Again, these values reduce rapidly, with increasing distance from the coast, staying below 11 mg/l beyond 20 m depth isoline, although showing higher values compared to river Minho.

In both locations, the mean bottom current direction was Northward, while it was noticeably stronger in the inner shelf area North of the river Minho, compared to the same location in river Douro (Figure 6.3 b)). The bottom current velocity exceeded 0.5 m/s in the Minho area, remaining mostly below or around 0.2 m/s in the Douro area.

In the surface layers, the suspended sediment concentration values were relatively alike to the ones described at the bottom layers and presented similar patterns (Figure 6.4 a)). On the other hand, the current velocities were remarkably higher (Figure 6.4 b)). In depths below 20 m, the maximum current velocity reached 1 m/s North of Minho, and in Douro, 0.8 m/s, with a coastal jet around 20 m depth contour, where velocities exceeded 0.9 m/s. The track of this jet can also be seen in the surface sediment concentration map.

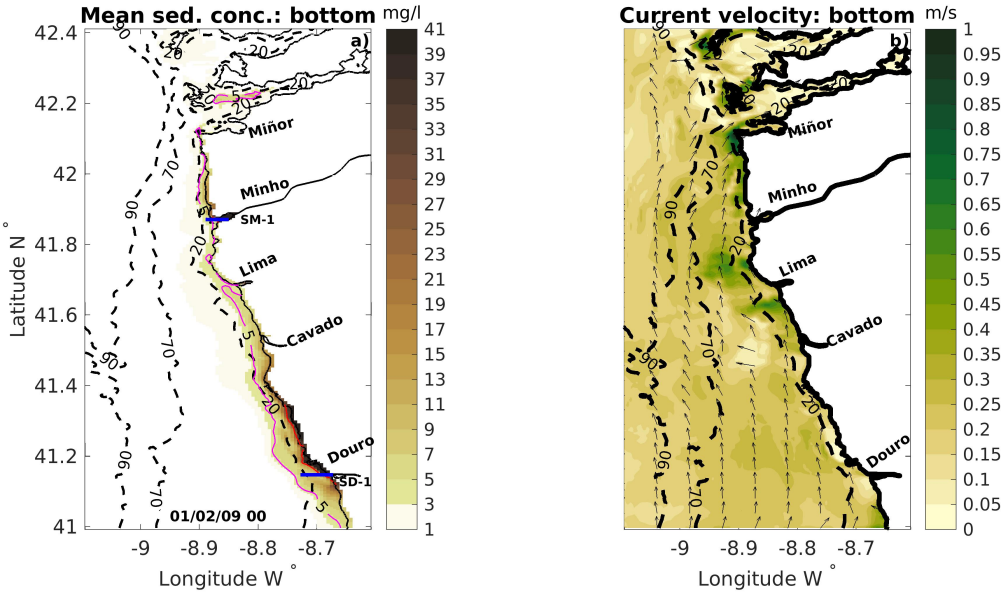

FIGURE 6.3: February 1st, 2009, a) The mean suspended sediment concentration at the bottom in a 5 m layer. The blue lines mark the locations of the vertical transects displayed in Figure 6.5. Red contour marks the 33 mg/l and magenta the 5 mg/l isopleth. b) The current velocity and direction (every 10th arrow) at the bottom.

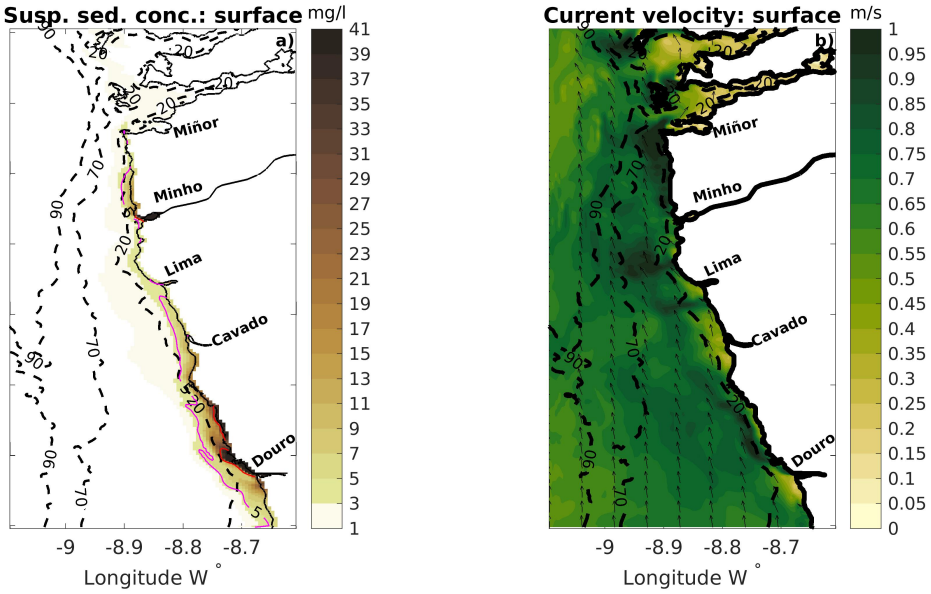

FIGURE 6.4: February 1st, 2009, a) The suspended sediment concentration at the surface layer. Red contour marks the 33 mg/l and magenta the 5 mg/l isopleth. b) The current velocity and direction (every 10th arrow) at the surface.

While observing the vertical structure of the water column of this event, the Minho transect (location in Figure 6.3 a) SM-1) shows that the suspended sediment concentration values drop drastically, with the distance from its source (Figure 6.5 a)). The 33 mg/l isoline coincides closely with the river Minho estuary entrance. The current systems indicate an oceanward flow in the surface and mid-layers, with maximums at the surface close to -0.4 m/s. Close to the bottom shoreward flow was present, with maximums around 0.1 m/s (Figure 6.5 b)). The along-shore velocity component v was Northward directed in the deeper region, and a counter-current flowed Southward close to the river Minho estuary, with maximum velocities around 0.5 m/s and -0.15 - -0.2 m/s, respectively (Figure 6.5 c)).

Similar conditions can be encountered in the Douro transect (location in Figure 6.3 a) SD-1), with greater magnitudes. Close to the entrance of the river, the suspended sediment concentration values were extremely high, approximating 105 mg/l and reducing rapidly to 80 mg/l with a distance from the source (Figure 6.5 d)). In the surface layers, the cross-shore component u was very strong, exceeding -0.7 m/s at the mouth of the river. The entire water body was moving away from the coast (Figure 6.5 e)). The along-shore velocity component v, indicated a strong Northwards flow, with higher velocities at the surface approximating 0.5 m/s (Figure 6.5 f)).

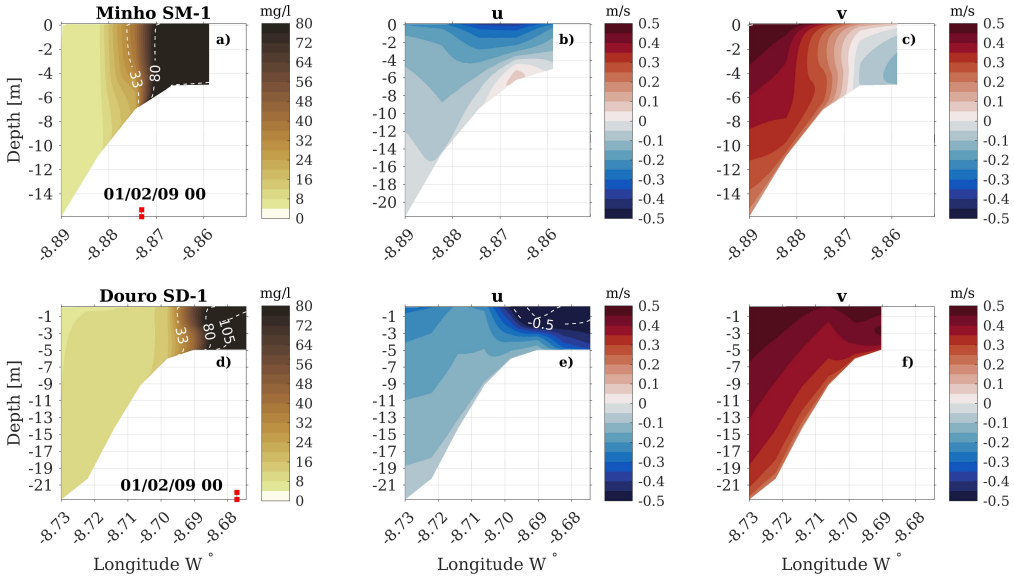

FIGURE 6.5: February 1st, 2009, vertical sections close to Minho estuary, at the SM-1 and close to river Douro, at the SD-1 locations (Figure 6.3) a), blue lines). a) and d) suspended sediment concentration. Red squares mark the location of the river mouth. b), e) and c), f) current velocity components u and v, respectively. White isopleth indicate velocities 0.5 and 0.7 m/s

Upwelling conditions on the shelf

Upwelling was seen from the 20th February 2009 event, although the sea state demonstrated calmer energy conditions. The maximum wave-current induced shear stress had reduced and river runoff decreased (Figure 6.2 a)). Sediments at the seabed were dispersed along the shelf close to the seabed, evidenced by the low levels of suspended sediments concentration in the middle and outer shelf ranging from 1-5 mg/l (Figure 6.6 a)). Near the estuaries of Minho and Douro, high sediment concentration areas were present South of the river mouths, notably larger in the Douro area. Maximum right off the coast close to Minho ranged from 51-71 mg/l, reducing to 21 mg/l at 20 m depth. Douro presented maximums between 111-151 mg/l, while the high concentration area patch right off the coast demonstrated values that exceeded 33 mg/l. The current velocity was moderate at the bottom layers, varying mostly between 0.03-0.06 m/s (Figure 6.6 b)). In line with the Ekman dynamics, predominantly directed Southeastwards.

At the surface, the suspended sediment concentration was significantly smaller compared to the concentration values at the bottom (Figure 6.7 a)). Sediments were propagating towards the ocean, with maximum values rounding close to 11 mg/l at the entrance of river Minho and 5 mg/l at the 20 m depth isoline. Two paths of sediment transport could be observed close to the Douro River. One moving ocean-wards, with maximums over 71 mg/l right off the river mouth and depleting to 33 mg/l at 20 m depth. A second one moving Southward, near the coastline, with a maximum between 61-71 mg/l. The surface currents were directed Westward (Figure 6.7 b)). Two high-velocity areas forming jet-like paths from the Minho and Douro rivers to the adjacent ocean could be seen. Velocities in these jets varied between 0.3-0.4 m/s. The higher concentration areas of suspended sediments at the surface largely correlate with the location and direction of the high-velocity areas.

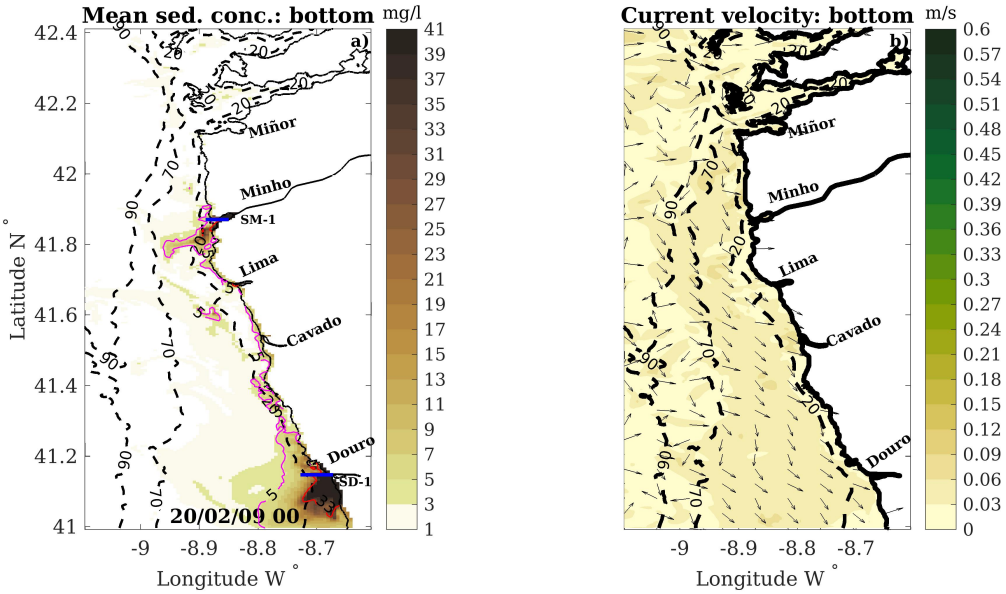

FIGURE 6.6: February 20th, 2009, a) The mean suspended sediment concentration at the bottom in a 5 m layer. The blue lines mark the locations of the vertical transects displayed in Figure 6.8. Red contour marks the 33 mg/l and magenta the 5 mg/l isopleth. b) The current velocity and direction (every 10th arrow) at the bottom.

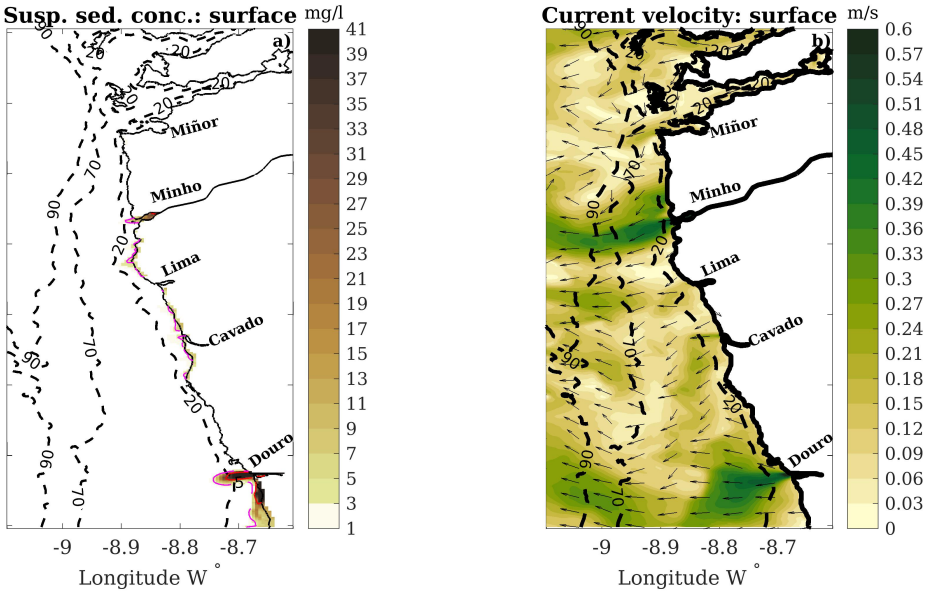

FIGURE 6.7: February 20th, 2009, a) The suspended sediment concentration at the surface layer. Red contour marks the 33 mg/l and magenta the 5 mg/l isopleth. b) The current velocity and direction (every 10th arrow) at the surface.

The suspended sediment concentration levels were significantly lower for the SM-1 transect in Minho, compared to the Douro transect SD-1 (Figure 6.8 a) and d)). In the surface layers, close to the river entrance of Minho, concentration ranged around 33-40 mg/l, while maximums at the bottom layer were between 16-20 mg/l. The velocity components u and v showed clear upwelling-driven circulation patterns (Figure 6.8 b) and c)). The cross-shore component u was mostly onshore directed in the bottom layers ranging between 0.05-0.15 m/s. A thin layer of approximately 3 m at the surface was moving the waters offshore, presenting a relatively strong velocity gradient changing from -0.05 to -0.45 m/s. The along-shore velocity component v indicates a Southwards flow, with maximums between -0.1 - -0.15 m/s.

The suspended sediment concentrations along the cross-section from Douro River exceeded 160 mg/l close to the river mouth and extended out to the shelf in the bottom layers approximately in a 2 m thick layer (Figure 6.8 d)). The suspended sediments at the surface moved away from the coast across a 3 m layer. The cross-shore velocity component u matched relatively well with the suspended sediment patterns profile (Figure 6.8 e)). The velocity at the bottom layers was 0.1-0.15 m/s, directed coastward and oceanward it in the surface layers with maximums little over -0.5 m/s. The along-shore velocity component ranges between -0.05 - -0.01 m/s, indicating a Southwards movement, with a counter-current at the surface close to the coast, with maximums around 0.15 m/s (Figure 6.8 f)).

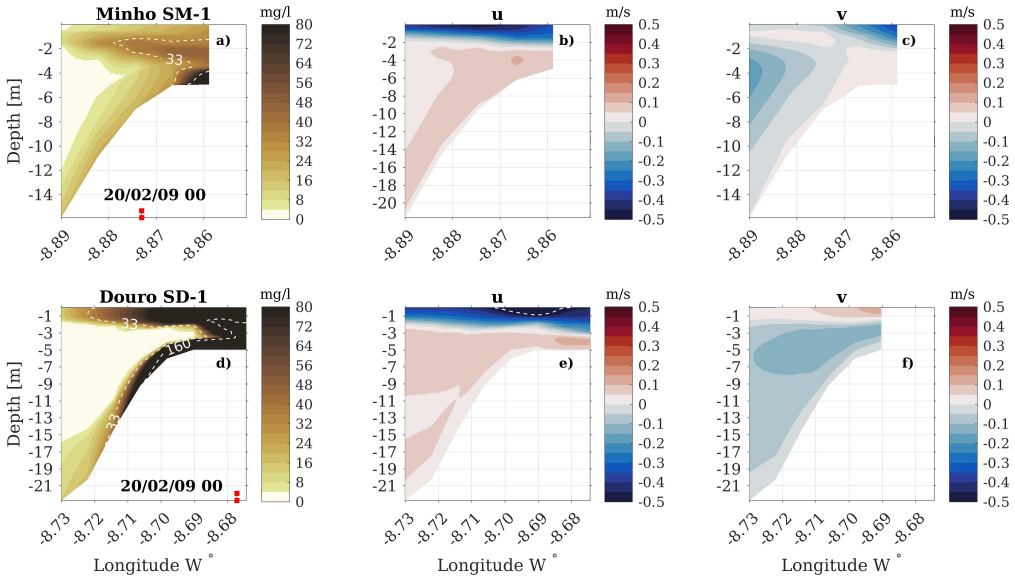

FIGURE 6.8: February 20th, 2009, vertical sections close to Minho estuary, at the SM-1 and close to river Douro, at the SD-1 locations (Figure 6.6) a), blue lines). a) and d) suspended sediment concentration. Red squares mark the location of the river mouth. b), e) and c), f) current velocity components u and v, respectively. White isopleth indicate velocities 0.5 and 0.7 m/s

Downwelling conditions on the shelf

At the end of the year 2009, several downwelling events occurred during which the mean suspended sediment concentration at the river Minho was significantly higher compared to similar events at the beginning of the year (e.g. Figure 6.2 c) e.g. 01.02 vs 22.12).

On 22nd of December 2009, the mean suspended sediment concentration close to the seabed revealed very high concentration areas close to the coast, moving Northwards from Minho and Douro (Figure 6.9 a)). These areas reached up to 20 m depth in the Douro region, with concentrations over 33 mg/l. Throughout the rest of the inner shelf, concentration levels stayed above 5-11 mg/l. The currents at the bottom were directed mainly Northwards, with maximum velocities around 0.2-0.4 m/s in different regions close to the coast (Figure 6.9 b)).

In the surface layers, the high sediment concentration areas showed similar distribution patterns as encountered at the bottom layers (Figure 6.10 a)). These areas were slightly bigger in the Douro region and significantly larger in the Minho region, extending out to the 20 m depth isoline. Transport across the inner shelf was almost non-existent. There can be encountered two high-velocity areas at the surface layers in the current field, near the 20 m depth contour directed Northwards (Figure 6.10 b)). Coastal jet North from Douro River presents velocities between 0.5-0.7 m/s, while velocities reach up to 1 m/s North from river Minho.

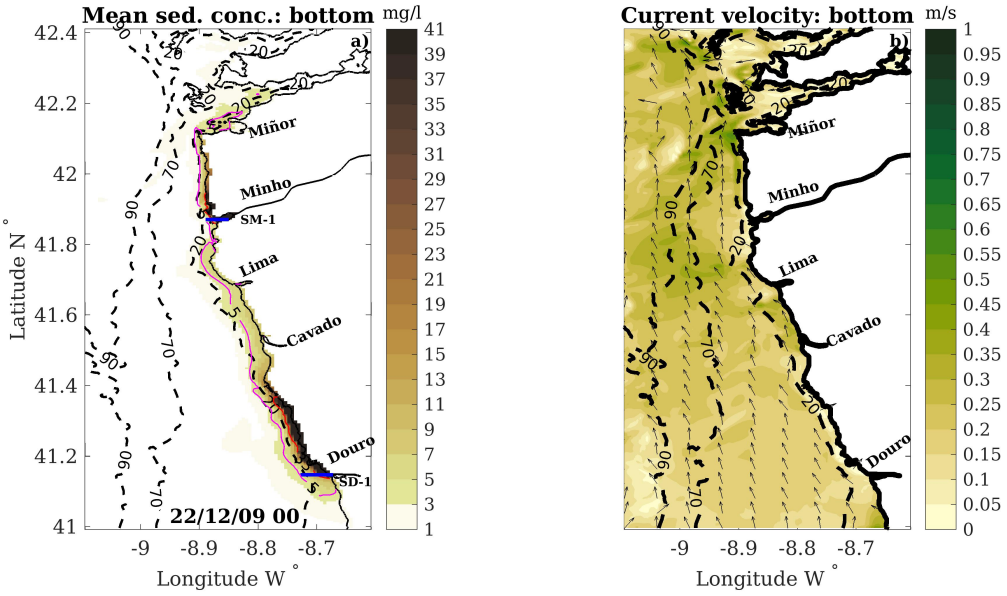

FIGURE 6.9: December 22nd, 2009, a) The mean suspended sediment concentration at the bottom in a 5 m layer. The blue lines mark the locations of the vertical transects displayed in Figure 6.11. Red contour marks the 33 mg/l and magenta the 5 mg/l isopleth. b) The current velocity and direction (every 10th arrow) at the bottom.

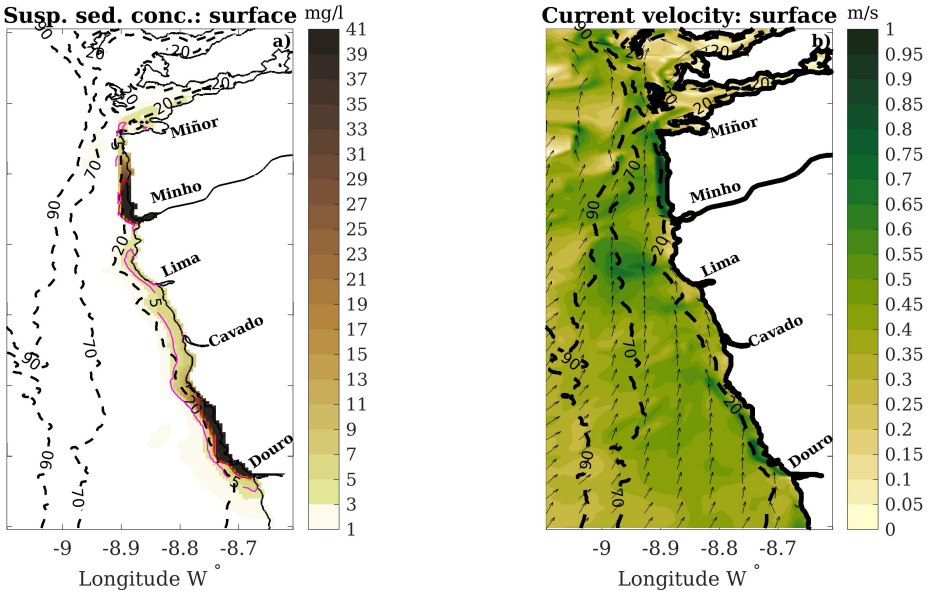

FIGURE 6.10: December 22nd, 2009, a) The suspended sediment concentration at the surface layer. Red contour marks the 33 mg/l and magenta the 5 mg/l isopleth. b) The current velocity and direction (every 10th arrow) at the bottom.

The vertical cross-section in the Minho River region indicates extremely high sediment concentration values leaving the river (Figure 6.11 a)). In the surface layers, still, inside the river estuary, the concentration levels exceed 600 mg/l. These levels decrease rapidly with the distance from its source, demonstrating a suspended sediment movement towards the shelf at the surface (Figure 6.11 b)). Significantly lower concentrations can be encountered at the bottom, with maximums ranging between 33-80 mg/l in the area out of the river entrance. Yet comparatively higher, compared to the two other events discussed previously (Figure 6.11 a)).

The cross-shore velocity component u indicates the movement of water towards the coast at the bottom layers and away at the surface (Figure 6.11 b)). The maximum at the surface was close to -0.3 m/s, much lower at the bottom, reaching only up to 0.1 m/s in the river estuary, and remaining below 0.05 m/s elsewhere. Alongshore component v was 0.3 m/s at the far side, flowing Northwards, with Southward counter-current at the mouth of the river estuary -0.15 m/s (Figure 6.11 c)).

The Douro section demonstrated similar concentration ranges compared to the previous downwelling event on February 1st (Figure 6.5 d)). Suspended sediment concentration at the bottom layers reduced from 80 mg/l to 33 mg/l in a short distance (Figure 6.11 d)), while at the surface layers the areas where concentrations exceeded 80 mg/l, extended further out from the estuary.

The current velocity component u indicated, that the water was moving away from the coast, with a high-velocity region at the surface layers reaching over -0.5 m/s. The v components showed solely Northwards flow, with the highest velocities very close to the surface varying between 0.4-0.5 m/s.

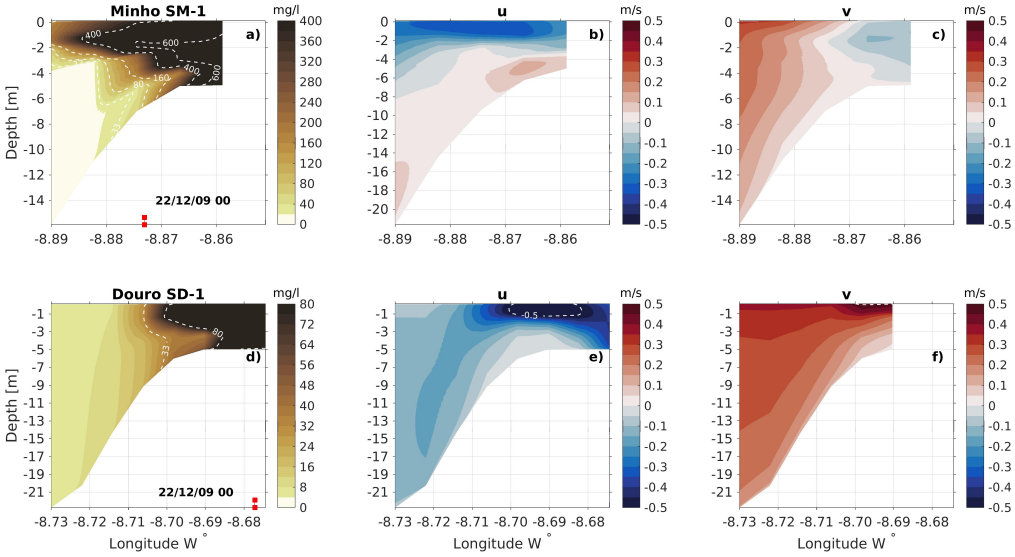

FIGURE 6.11: December 22nd, 2009, vertical sections close to Minho estuary, at the SM-1 and close to river Douro, at the SD-1 locations (Figure 6.9) a), blue lines). a) and d) suspended sediment concentration. Red squares mark the location of the river mouth. b), e) and c), f) current velocity components u and v, respectively. White isopleth indicate velocities 0.5 and 0.7 m/s

6.4 Discussion

6.4.1 Sediment input from rivers during off-storm seasons

Due to the nature of the formulations used, there was a linear correlation between the sediment input and river discharge (Equation 6.2). A higher river outflow flow carried more sediments in it. This translated into variable mean sediment concentration values at the river outlet, that did not only depend on the imposed sediment concentration levels and river discharge but also on the hydrodynamic conditions and morphology of the shelf. This was distinctly seen from the time series of river runoff, input and mean sediment concentration levels at the mouth of river Minho and Douro estuaries (Figure 6.2 b),c) and d), e)).

Although during the off-storm period, the river Minho flow continued to carry sediments, the mean concentration stayed very low. During annual terms in spring, summer and autumn, river Douro flow did not introduce any new sediment to the shelf, however, higher mean sediment concentration values were present. Most likely, this was the fluctuation of sediments released previously and deposited close to the estuary. The difference in the sediment concentration levels during the off-storm season in the two rivers was probably due to the morphological characteristics of the shelf and the river flow capacity. The sediments from river Minho were either deposited inside the river or close to the estuary, as the river flow was weak. Whereas the Southern region of the study area, with a smaller

depth gradient, was more receptive to the ocean forcing. The sediments from the seabed, close to the estuary, were re-suspended.

For the most part during the off-storm season, very low concentrations of suspended sediments can be seen on the continental shelf, principally confined to the inner shelf at the surface and, inner and mid-shelf at the bottom.

6.4.2 Shelf circulation and sediment transport

The results of the simulations depict the complex dynamics between the shelf circulation and the transport patterns of sediments introduced by the rivers to the shelf. Giving an idea, about the relation between the ocean state and river runoff, and their influence on the amount of sediment dispersed in the continental shelf.

On the whole, Douro River introduced more sediments to the shelf system, compared to Minho River, due to the higher flow capacity. During the winter season, the storm peaks were mostly accompanied by a larger river discharge. When a high river discharge coincided with a storm event, that had a well-established circulation regime, the suspended sediments leaving the river systems were rapidly transported away from their source. In case of downwelling Northwards (Figures 6.3 and 6.4) and with upwelling Southward (not shown), inside the inner shelf region in a limited and confined area. In storm conditions, no cross-shore transport occurred.

Milder oceanographic conditions along with possibly lower river sediment discharge allowed the development of sediment blooms and further transport offshore through bottom or surface layers (Figure 6.6 and 6.7, 6.11).

6.4.3 Changes in the seabed sediments

The movement of this very fine fraction of silt 1, did not translate to any significant changes in the seabed surface sediments. The order of magnitude stayed in the μm range. However, it was possible to identify areas where erosion or deposition of sediments occurred. For example during the downwelling event on 22 December 2009 (Figure 6.9, 6.10, 6.11), there could be seen accumulation and erosion of sediments across the shelf (Figure 6.12). Deposition of sediments occurred in the Galicia mud patch, in the mid-shelf area between river Douro and Cavado until approximately 70 m depth, in the inner shelf from river Minho up to the Galician Rías. Everywhere else on the shelf until approximately 90 m, erosion took place, which was the most visible in the inner shelf region South of Douro River. Similar deposition and erosion patterns were simulated in the *Zhang et al.* (2016) study during a downwelling event.

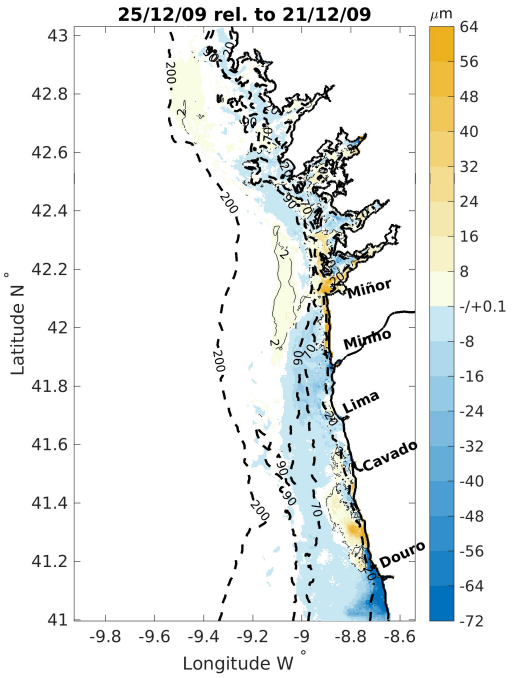

FIGURE 6.12: December 22nd, 2009, changes in the seabed considering only the finest fraction, silt 1.

6.5 Conclusion

The numerical model CROCO, together with wave model SWAN was configured and implemented specifically to understand the fate of the sediments coming from the river systems. The overall behaviour of the model was relatively satisfactory, based on the comparison with other similar studies about the subject. The simulations demonstrated comparatively well the general patterns and transport pathways of suspended sediments coming from the rivers.

For both rivers, Minho and Douro, it was clear that the relation between the sediment input from rivers, river runoff and the amount of sediments transported away from the river estuaries was not straightforward. In general, the Douro River introduced more sediment to the shelf than Minho. Most likely, this was due to the differences in the river flow capacity and characteristics of regions. When a storm and a high river runoff coincide, the majority of sediments are introduced to the shelf. The suspended sediments were rapidly transported in the inner shelf along the coast North, during downwelling or South, with upwelling-driven circulation. No cross-shore transport occurred. Less energetic conditions at the shelf, but velocities strong enough to transport suspended sediments, allowed the sediments to disperse beyond the inner shelf. The milder oceanographic environments made possible the formation of sediment transport pathways across the shelf through surface or

bottom layers. During very low energy periods on the shelf, like late spring, summer and early autumn, sediment introduced from the rivers to the shelf was extremely limited.

To increase confidence in the model results, there is an urgent need for long-term observational data sets. Information about the type of sediments and concentration levels across the river estuaries and in the inner shelf would help immensely to improve the models. It would make it possible to calibrate the numerical model's site specifically and generate valuable information about the suspended sediment movement.

Chapter 7

Conclusions and future research

The present thesis focused on studying different aspects of suspended sediment transport on the continental shelf. The outcome of this work helped to improve the understanding of the underlying physical processes affecting the fine-grained sediment transport in different time scales. Considering the impact of storm events, inter-annual and seasonal variability. Moreover, the research advanced the knowledge in comprehending the link between forcing mechanisms and sediment re-suspension and transport patterns. In addition, the first steps were made to study the fate of the materials coming from the rivers. Through the successful implementation of a numerical modelling system, supported by *in situ* data, the findings were in alignment with the existing research, while providing new insight into the continental shelf sediment dynamics.

A multidisciplinary approach was adopted to implement a modelling system. The numerical model CROCO with sediment model was used as a main tool in this study. The wind and wave forcing terms were included through offline coupling, from the atmospheric and wave models WRF and SWAN. A high-resolution configuration was built, using a nested grid system. The study site, NW Iberia continental shelf, is situated in an upwelling affected area and characterized by a highly energetic wave regime during winter. A 14-month-long period was considered, from November 2008 until December 2009, covering an annual cycle while including two distinct winter seasons. The strengths and weaknesses of the configuration were described in detail, to analyze and interpret the results accordingly.

The quality of the dynamical forcing in many ways determines the success of a modelling study. This was demonstrated distinctly, while evaluating the performance of the wave model SWAN, considering different wind data sets. The results showed the influence of wind products on various wave characteristics and the importance of accurate wind speed and direction over spatio-temporal resolution.

The validation process of the modelling system, designed to solve the sediment transport dynamics, was carried out by exploiting various types of *in situ* observations. Wave buoy data, ADCP, monthly hydrographic surveys and information from the sediment trap were used to evaluate the accuracy of the modelling system. The statistical and quantitative analysis showed a relatively good agreement between the modelled and measured data for all the models. It was possible to verify that the wave model SWAN simulated comparatively well the evolution of the wave field and the hydrodynamic model CROCO exhibited reliable capabilities to reproduce the shelf circulation. Moreover, the sediment

transport model efficiently described the fundamental sediment transport processes and simulated the seasonal variations. However, for a better site-specific calibration of the sediment model, more direct and long-term sediment data would be needed about the study site. All the numerical models considered in this thesis, had been previously successfully implemented in the site of interest and around the world, to study different problems. This allowed us to assess, compare and improve the present set-up of the modelling system, creating reliable simulations. On the other hand, further advance the skills and efficiency of these models.

The relation between the forcing mechanisms and the sediment transport patterns revealed the effect of waves, seasonal and general shelf circulation, influence of storms and morphological features. The simulations indicated that the re-suspension of sediments on the shelf was controlled by the co-dominant effect of currents and waves. At the same time, it was largely influenced by the seasonality of the circulation patterns and wave energy. During winter months, the storm-driven upwelling or downwelling favoured the Southward and Northward transport of sediments, enhanced by the wave activity. Extreme storms had a remarkable and lasting impact in re-distributing the sediments, reaching also the outer shelf. The morphology of the continental shelf limited the cross-shore transport of sediments in the Southern region of the study site while promoting the formation of bottom eddies mainly in the Northern region, forming pathways for transport of sediment to the adjacent ocean.

To understand the fate of sediment coming from the river systems, various limitations have to be overcome. The biggest challenge arises from the lack of information about the properties and amount of the sediments transported by the rivers to the shelf. Nevertheless, the modelling system produced relatively reasonable results based on the comparison made with the literature. The simulation reproduced the general patterns and transport pathways of suspended matter originating from the rivers. At the same time, demonstrating the dynamics between the sediment input, river discharge and the volume of sediments entering the shelf.

While taking account of the simplifications and generalizations made in the modelling system, the results obtained demonstrated a good level of accuracy, comparable with other similar studies or even slightly better. The present configurations allow us to fill in the gaps in the observational data sets, due to the malfunctions of the equipment or scarce sampling periods. Also, reproduces the general dynamics of sediments of this region's continental shelf during a different period, even when the measurement data available is lacking. The findings in this thesis could be useful as well in different multidisciplinary studies related to benthic habitats, aquaculture, and detection of contaminants deposition, among many others. The results could be used in the Lagrangian models to solve problems related to, for example, environmental issues (oil spills, microplastics) or marine biology (larvae transport). For future research, this work has helped to lay down the road, to further study the long-term changes of the seafloor, transport patterns of material coming from the river systems and eventually run through different climate change scenarios. The modelling system also permits the implementation of biogeochemical modules, opening up new possibilities for research topics.

Appendix A

Sediment.in

The input file sediment.in describes 14 parameters, that have to be chosen to use in the sediment module.

1. Sediment grain diameter:
   Sd $[mm]$, varies according to the surface sediment distribution map on Figure 2.2.

2. Initial concentration:
   CSED $= 0$ $[kg/m^3]$

3. Density of sediment material of size class (quartz):
   $\rho_s = 2650$ $[kg/m^3]$

4. Settling velocity:
   WSED $[mm/s]$, based on *Soulsby* (1997) equations 75 and 102.

$$w_{s,m} = \frac{10^3(\nu(\sqrt{10.36^2 + 1.049D^3} - 10.36))}{D_{50}} \tag{A.1}$$

   where $D = D_{50} * (g * (\rho_s/\rho_0 - 1)/(\nu^2))^{0.33333}$, $\rho_0 = 1025$ $[kg/m^3]$, $D_{50} = Sd10_{-3}$, $[m]$, $g = 9.8$ $[m^2/s]$, $\nu = \frac{1.310_{-3}}{\rho_0}$ $[m^2/s]$

5. Erosion rate:
   ERATE $[kg/m^2/s]$,

$$ERATE = \gamma_0 w_{s,m} \rho_0 10^{-3} \tag{A.2}$$

   where $\gamma_0 = 10^{-3} - 10^{-5}$ (*Smith and McLean*, 1977). For the current configuration $\gamma_0 = 10^{-5}$ is applied.

6. Critical shear stress for sediment motion:
   TAU_CE $[N/m^2]$, for suspended load the critical stress is calculated as

$$\tau_{ce,m} = 6.410^{-7} \rho_0 w_{s,m}^2 \tag{A.3}$$

   Oberle et al. (2014) calculated the critical stress for the mobilization of the sediment bed using the Shield parameter methodology of *Madsen and Grant* (1977). The

cohesive effects of the fine particles on the critical shear stress were incorporated into the model by applying *van Rijn* (2007) methodology that effectively adds the impact of gelling and cohesive forces to the modified Shield parameter formulation. This methodology was later on also applied in the current study for the fine particle classes (1 and 2).

Zhang et al. (2016) uses a constant threshold value (0.1 Pa) for resuspension of suspended sediments. The availability of surface sediments for resuspension was limited by consolidation and armouring effects.

7. Critical shear stress for deposition of cohesive sediments:
   TAU_CD $[N/m^2]$ - currently is not used in the model.

8. Volume fraction of each size class in each bed layer (NLAY columns):
   BED_FRAC = 100 [%]
   The implicit assumption is that sum(bed_frac) should be 100 % along the the bed layers.

9. Initial thicknesses of bed layers:
   BTHK $[m]$
   Bthk(1) active layer thickness, fixed in simulation unless $SUM(Bthk(:)) < Bthk(1)$.
   In the current configuration there are 8 bed layers, with total thickness of 6 m. The thickness distribution starting from the top layer is as fallows: 0.01; 0.01; 0.01; 0.01; 0.01; 0.95; 2; 3.

10. Initial porosity of bed layers:
    BPOR = 0.41

11. Bottom ripple height:
    Hrip = 0 $[m]$

12. Bottom ripple length:
    Lrip = 0 $[m]$

13. Bed load transport rate coefficient
    bedload_coeff = 0, currently bedload is not considered.

14. Morphological time scale factor $morph\_fac >= 1$.
    morph_fac = 1. A value 1 has no scale effect.

Appendix B

Changes to the CROCO source code

- averages.h
  - when using WKB wave model, variables whrm_avg and wfrq_avg had to be declared as real.
- ncscrum.h and ncscrum_F90.h
  - the number of characters for the file names was increased.
- param.h
  - maximum allowed number of parallel threads (NPP) was increased.
- bbl.F
  - modified to calculate *bustr, bvstr* as in get_vbc.F, when no waves are present. *Bustr, bvstr* are used in the calculation of current velocities.

MPI_master_only added to reduce the information written out in .txt:

- sediment.F - lines 2196 and 2295.
- get_initial.F - lines 355 and 374.
- get_wwave.F -
- line 313.

To add waves from offline source:

- get_wwave.F
  - possibility to add one or several points, where the variable of your choice will be written out.
  - interpolation of wave direction between 360 and 0 was corrected.

  - a flag SWAN_DIR_CONVENTION was created and added. It was activated in the ccpdefs.h to avoid the change in the direction convention (Input in deg.; Cartesian convention)
  - WAVE_OFFLINE flag added to initiate the calculation of some variables like whrm, wfrq etc.

- ncscrum.h
  - define WAVE_OFFLINE was added to declare integer indxSUP, indxUST2D, indxVST2D.

- def_his.F
  - added defined WAVE_OFFLINE to declare integer iwkb.

- forces.h
  - define WAVE_OFFLINE was added to declare real whrm(GLOBAL_2D_ARRAY), wepb, wepd, wdrx, wdre.

- read_inp.F
  - define WAVE_OFFLINE was added, so the model would go to look for forcing file.

Agrif: Currently not working correctly

- zoom.f
  - get_sediment is not called as this subroutine does not exist.
  - in the child's grid level the ana_sediment was not called so the bed_fraction was not initialized (modified by Rachid Benshila, LEGOS, CNRS, Toulouse, France).

- BUG I
  - When running CROCO in AGRIF with offline waves and idealized sediments, variables v (v-momentum component) and w (vertical momentum component) in the history and average output have a square shape areas where the values are 0. After approximately 1 day the model recuperates and presents reasonable results.

    Solution: This problem does not occur when using more than one class of sediments.

- BUG II
  - Everything related to the water column is passing well from the child's grid to the parent grid, only the information about the sediment bed is not being passed correctly, causing the erosion in the parent grid and accumulation in the child's grid.

Writing average variables (BBL)

- def_his.F
  - when asking to write out the average variables related to BBL module, the model bowed up with a following error: " DEF_HIS/AVG ERROR: Cannot find variable 'Abed' in netCDF file '/.../res/cro_avg_.nc.1'". BBL is defined (searched for indxBBL) for two cases: assigning attributes for the NetCDF file and writing the variable. When average values were calculated no attributes had been assigned in the NetCDF file, although the model tried to write the variables and that caused the above-named error. So for now, an additional condition *&& ! defined AVRH* was added to *# if defined BBL*, so the model would not try to write the average variables. Moreover, it turned out that the average values for Abed, Hripple, Lripple, Zbnot, Zbapp and bostrw are never calculated.
- read_inp.F
  - when asking to write out the average variables related to BBL module, the same error occurs as described above. In read_inp.F, where there is *define BBL* (line 1769) the average variables are assigned as history variables, although they are never calculated.

To read sediment bed from initial NetCDF file:

- get_initial.F
  - indxWrk is used instead indxHrip and indxLrip when writing messages in the information .txt file. CROCO always looks for ripple height and length values, even if ripples are not defined. This produces an error in the information .txt file, saying that bed fraction values were not found from the initial NetCDF file and the analytical values are used. This is somewhat miss leading, as actually the ripple height and length values are being looked for.
- analytical.F
  - when reading bed fraction values for the sediment bed in the initial NetCDF file, *END-IFs* were placed in a way that bed_age, bot_thick, bed_mass and some other variables were newer calculated, causing all the variables that were related to sediments to be 0.

- BEDROCK
  - there exists an assumption that sum(bed frac) along the vertical axes of the sediment bed should be 100 %. If a 0-bed fraction is set to some of the grid cells (the sum(bed frac) of the grid cell bed layers = 0), the model creates areas where the bed fraction is set to 100 % even though, there should not exist any sediments. **Solution:** Use fake sediment with unrealistically large settling velocity, critical stress etc. and distribute it to the areas with no sediments (no information). Also can be used as bedrock.

To increase the number of sediments size classes read from .nc file:

- init_scalars.F
  - if conditions were added to the variables that are read from the initial NetCDF file and that that contained *sand_* in their name. NB! Note that some of the variables that are not read or written as output with this configuration, were not changed (mud, gravel etc.). It may cause problems later on.
- put_global_atts.F
  - if conditions was added to the variables that contained *sand_* in their name.

To have stations output as -ASCII file:

- all the files modified are located in a separate folder.
  - to include or exclude these changes modify *jobcomp*.
  - keep in mind that the location inserted in the stations file will be dislocated depending on the configuration. Verify this with the script *gre_MY_sta.m*.
  - if line 486 in *wrt_sta.F (else /* defined STA_wrt_nc */)* is commented also netcdf file will be produced (keep in mind that any small disconnection between MPIs will cause the model run to stop).

Bed roughness for sediment purposes

- bbl.F
  - line 351. To calculate the maximum wave-current stress for sediment purposes *znot* is used instead of default *znotc*, as with *znotc* the maximum wave current bottom stress was demonstrating very low values.
  - When activating ripples, the maximum wave-current stress for sediment purposes will be recalculated, by default it was not done.

Rivers, waves and sediments

- nscrum.h
  - line 500. When activating rives and waves from offline source, the index of wave variable and river was the same. So the model searches for a variable in the *river_forcing.nc* file, that has to do with waves. The number of indexes in the nscrum.h was increased.
- analytical.F
  - line 1847. The following loop was relocated:
    do is=1,Nsrc Qbar0(is)=Qbar(is) enddo
  - If the model blows up on a land point or close to the river location then there are two options to resolve this issue.
    1) Increase the salinity for this river temporarily for the months when river runoff is strong
    2) Change how the river input is distributed. Three options: uniform and exponential. For exponential add a new flag to cppdef and for fine grid change cff in analytical.F to 1 or 2.
    3) Increase the time step of the finer grid

  Sediments from river system
  In croco.in file *if Lsrc is F* the values of the sediment concentrations from rivers will not be read in from the NetCDF and instead, the value that is predefined in the analytical.F will be considered. *If T*, the values will be read from the NetCDF. When needed 0 concentration, it is better to read it from the NetCDF file. Another thing to remember. When adding extra sediment types for the river input, it also has to be declared in the initial NetCDF, as non-existent but all the attributes have to be given. Otherwise, if the program does not find them and the initial distribution of the sediment bed will be considered analytic.
- get_psource_ts.F
  - line 69. Look for the new variables in the netcdffile.
  - line 498. Read the concentration values from netcdf.
- init_scalars.F
  - lines 1625 and 1642. Declare a new variable.
- analytical.F
  - line 1909. Set-up tracer (tracer units) point Sources/Sinks.

Bibliography

PO-Waves Group (1994), Final report of sub-project a. wind wave climatology of the portuguese coast, *Report PO-Waves*, *6*.

Alari, V. (2013), Multi-Scale Wind Wave Modeling in the Baltic Sea, Doctoral dissertation, Tallinn University of Technology.

Alvarez, I., M. Gomez-Gesteira, M. deCastro, and D. Carvalho (2014), Comparison of different wind products and buoy wind data with seasonality and interannual climate variability in the southern bay of biscay (2000–2009), *Deep Sea Research Part II: Topical Studies in Oceanography*, *106*, 38–48.

Álvarez-Salgado, X. A., F. Figueiras, F. F. Pérez, S. Groom, E. Nogueira, A. V. Borges, L. Chou, C. Castro, G. Moncoiffé, A. Ríos, et al. (2003), The portugal coastal counter current off nw spain: new insights on its biogeochemical variability, *Progress in Oceanography*, *56*(2), 281–321.

Alves, J., A. Peliz, R. Caldeira, and P. Miranda (2018), Atmosphere-ocean feedbacks in a coastal upwelling system, *Ocean Modelling*, *123*, 55–65.

Amante, C., and B. W. Eakins (2009), ETOPO1 1 arc-minute global relief model: Procedures, data sources and analysis, *NOAA Tech. Mem. NESDIS NGDC-24*, *10*, doi:10.1594/PANGAEA.769615.

Amoudry, L. O., and A. J. Souza (2011), Deterministic coastal morphological and sediment transport modeling: A review and discussion, *Reviews of Geophysics*, *49*(2), doi:10.1029/2010RG000341.

Appendini, C. M., A. Torres-Freyermuth, F. Oropeza, P. Salles, J. López, and E. T. Mendoza (2013), Wave modeling performance in the gulf of mexico and western caribbean: Wind reanalyses assessment, *Applied Ocean Research*, *39*, 20–30.

Ariathurai, R., and K. Arulanandan (1978), Erosion rates of cohesive soils, *Journal of the Hydraulics Division*, *104*(2), 279–283.

Barton, E. D., B. Barreiro, T. Meunier, F. de la Granda Grandoso, N. Villacieros-Robineau, F. A. Pérez, and W. Redondo (2019a), RAIA Acoustic Doppler Profiler (ADP) currents near Cape Silleiro (NW Iberia), doi:10.20350/digitalCSIC/8959.

Barton, E. D., B. Barreiro, T. Meunier, F. de la Granda Grandoso, N. Villacieros-Robineau, F. A. Pérez, D. Zúñiga, M. Froján, C. G. Castro, and W. Redondo (2019b), RAIA CTD surveys (42.1^{o}N) near Cape Silleiro (NW Iberia), doi:10.20350/digitalCSIC/8960.

Bastos, L., A. Bio, and I. Iglesias (2016), The importance of marine observatories and of raia in particular, *Frontiers in Marine Science*, *3*, 1–11.

Bauer, J. E., and E. R. Druffel (1998), Ocean margins as a significant source of organic matter to the deep open ocean, *Nature*, *392*(6675), 482–485.

Becker, J., D. Sandwell, W. Smith, J. Braud, B. Binder, J. Depner, D. Fabre, J. Factor, S. Ingalls, S. Kim, et al. (2009), Global bathymetry and elevation data at 30 arc seconds resolution: SRTM30_PLUS, *Marine Geodesy*, *32*(4), 355–371.

Benetazzo, A., S. Carniel, M. Sclavo, and A. Bergamasco (2013), Wave–current interaction: Effect on the wave field in a semi-enclosed basin, *Ocean Modelling*, *70*, 152–165.

Bever, A. J., and C. K. Harris (2014), Storm and fair-weather driven sediment-transport within Poverty Bay, New Zealand, evaluated using coupled numerical models, *Continental Shelf Research*, *85*, 34–51.

Blaas, M., C. Dong, P. Marchesiello, J. C. McWilliams, and K. D. Stolzenbach (2007), Sediment-transport modeling on Southern Californian shelves: A ROMS case study, *Continental Shelf Research*, *27*(6), 832–853, doi:10.1016/j.csr.2006.12.003.

Blumberg, A. F., and G. L. Mellor (1987), A description of a three-dimensional coastal ocean circulation model, *Three-dimensional coastal ocean models*, *4*, 1–16.

Booij, N., R. Ris, and L. H. Holthuijsen (1999), A third-generation wave model for coastal regions: 1. model description and validation, *Journal of geophysical research: Oceans*, *104*(C4), 7649–7666.

Bosnic, I. (2017), Nearshore sedimentary dynamics in a wave-dominated coast, Ph.D. thesis, University of Lisbon.

Burchard, H., and K. Bolding (2002), GETM: A General Estuarine Transport Model, Scientific Documentation, European Commission, Joint Research Centre, *Institute for Environment and Sustainability*, *12262*, 25.

C3S (2017), ERA5: Fifth generation of ECMWF atmospheric reanalyses of the global climate, Copernicus Climate Change Service Climate Data Store (CDS), 20 May 2018. https://cds.climate.copernicus.eu.

Carvalho, D., A. Rocha, and M. Gómez-Gesteira (2012), Ocean surface wind simulation forced by different reanalyses: Comparison with observed data along the Iberian Peninsula coast, *Ocean Modelling*, (56), 31–42, doi:10.1016/j.ocemod.2012.08.002.

Carvalho, D., A. Rocha, M. Gómez-Gesteira, I. Alvarez, and C. S. Santos (2013), Comparison between ccmp, quikscat and buoy winds along the iberian peninsula coast, *Remote Sensing of Environment*, *137*, 173–183.

Carvalho, D., A. Rocha, M. Gómez-Gesteira, and C. Silva Santos (2014), Comparison of reanalyzed, analyzed, satellite-retrieved and NWP modelled winds with buoy data along the Iberian Peninsula coast, *Remote Sensing of Environment*, *152*, 480–492, doi: 10.1016/j.rse.2014.07.017.

Castro, C., X. Álvarez-Salgado, F.-G. Figueiras, F. Pérez, and F. Fraga (1997), Transient hydrographic and chemical conditions affecting microplankton populations in the coastal transition zone of the Iberian upwelling system (NW Spain) in September 1986, *Journal of Marine Research*, *55*, 321–352, doi:10.1357/0022240973224436.

Castro, C. G., N. Villacieros-Robineau, F. A. Pérez, D. Zúñiga, F. de la Granda Grandoso, S. F. Bastero, R. Bañuelos, and E. Salgueiro (2020a), CALIBERIA Site V1.0, doi:10.20350/digitalCSIC/10539.

Castro, C. G., N. Villacieros-Robineau, F. A. Pérez, D. Zúñiga, F. de la Granda Grandoso, M. Froján, and E. Salgueiro (2020b), CALIBERIA Site CTD V1.0, doi:10.20350/digitalCSIC/10540.

Colella, P., and P. R. Woodward (1984), The piecewise parabolic method (ppm) for gas-dynamical simulations, *Journal of Computational Physics*, *54*(1), 174–201.

Cordeiro, N. (2018), Numerical and observational processes study of Northwestern Iberian margin circulation, Ph.D. thesis, University of Aveiro.

Cordeiro, N. G., R. Nolasco, A. Cordeiro-Pires, E. D. Barton, and J. Dubert (2015), Filaments on the Western Iberian Margin: A modeling study, *Journal of Geophysical Research: Oceans*, *120*(8), 5400–5416, doi:10.1002/2014JC010688.

Cordeiro, N. G., R. Nolasco, E. D. Barton, and J. Dubert (2021), Fixed-point time series, repeat survey and high-resolution modeling reveal event scale responses of the northwestern iberian upwelling, *Progress in Oceanography*, *190*, 102,480, doi:https://doi.org/10.1016/j.pocean.2020.102480.

Costa, M., and R. Esteves (2009), Clima de agitação marítima na costa oeste de portugal continental. in: Comunicações das xi jornadas técnicas de engenharia naval.

Csanady, G. T., and P. T. Shaw (1983), The "insulating" effect of a steep continental slope, *Journal of Geophysical Research*, *88*(C12), 7519, doi:10.1029/JC088iC12p07519.

Davies, A. M., J. Xing, J. M. Huthnance, P. Hall, and L. Thomsen (2002), Models of near-bed dynamics and sediment movement at the Iberian Margin, *Progress in Oceanography*, *52*(2-4), 373–397, doi:10.1016/S0079-6611(02)00016-2.

Debreu, L., P. Marchesiello, P. Penven, and G. Cambon (2012), Two-way nesting in split-explicit ocean models: Algorithms, implementation and validation, *Ocean Modelling*, *49*, 1–21.

Dee, D. P., S. M. Uppala, A. J. Simmons, P. Berrisford, P. Poli, S. Kobayashi, U. Andrae, M. Balmaseda, G. Balsamo, d. P. Bauer, et al. (2011), The era-interim reanalysis: Configuration and performance of the data assimilation system, *Quarterly Journal of the royal meteorological society*, *137*(656), 553–597.

Dias, J. (1987), Dinamica sedimentar e evolucao recente da plataforma continental portuguesa setrentrional, Ph.D. thesis, Lisboa.

Dias, J. A., L. C. Gaspar, and J. H. Monteiro (1980), Sedimentos recentes da plataforma continental portuguesa a norte do canhão submarino da nazaré, *Bol. Soc. Geol. Port*, *81*(22), 181–185.

Dias, J. A., A. Rodrigues, and F. Magalhães (1997), Evolução da linha de costa, em portugal, desde o último máximo glaciário até à actualidade: síntese dos conhecimentos, *Estudos do Quaternário/Quaternary Studies*, *1*(1).

Dias, J. M., J. M. Jouanneau, R. Gonzalez, M. F. Araújo, T. Drago, C. Garcia, A. Oliveira, A. Rodrigues, J. Vitorino, and O. Weber (2002a), Present day sedimentary processes on the northern Iberian shelf, *Progress in Oceanography*, *52*(2-4), 249–259, doi:10.1016/S0079-6611(02)00009-5.

Dias, J. M. A., R. Gonzalez, C. Garcia, and V. Diaz-del Rio (2002b), Sediment distribution patterns on the Galicia-Minho continental shelf, *Progress in Oceanography*, *52*(2-4), 215–231, doi:10.1016/S0079-6611(02)00007-1.

Dietrich, J., S. Bunya, J. Westerink, B. Ebersole, J. Smith, J. Atkinson, R. Jensen, D. Resio, R. Luettich, C. Dawson, V. Cardone, A. Cox, M. Powell, H. Westerink, and H. Roberts (2010), A high-resolution coupled riverine flow, tide, wind, wind wave, and storm surge model for southern louisiana and mississippi. part ii: Synoptic description and analysis of hurricanes katrina and rita, *Monthly Weather Review*, *138*(2), 378–404.

Drago, T., J. Jouanneau, J. Dias, R. Prud'Homme, S. Kuehl, and A. Soares (1994), La vasière ouest-douro et le piegeage des sédiments estuariens récents, *GAIA 9. Simpósio sobre a Margem Continental Ibérico-Atlântica*, pp. 28–30.

Faria, C. S. G. (2009), Previsão da agitação marítima na costa noroeste portuguesa: implementação do modelo swan, Master dissertation, Faculdade de Engenharia, Universidade do Porto.

Fischer, G., and G. Karakaş (2009), Sinking rates and ballast composition of particles in the Atlantic ocean: Implications for the organic carbon fluxes to the deep ocean, *Biogeosciences*, *6*(1), 85–102, doi:10.5194/bg-6-85-2009.

Fischer, G., G. Karakas, M. Blaas, V. Ratmeyer, N. Nowald, R. Schlitzer, P. Helmke, R. Davenport, B. Donner, S. Neuer, and G. Wefer (2007), Mineral ballast and particle settling rates in the coastal upwelling system off NW Africa and the South Atlantic, *International Journal of Earth Sciences*, *98*(2), 281–298, doi:10.1007/s00531-007-0234-7.

Fiúza, A. F. (1983), Upwelling patterns off portugal, in *Coastal Upwelling its sediment record*, pp. 85–98, Springer.

Fiúza, A. F. G., M. E. Macedo, and M. R. Guerreiro (1982), Climatological space and time variation of the portuguese coastal upwelling, *Oceanologica acta*, *5*, 31–50.

Franz, G., L. Pinto, I. Ascione, M. Mateus, R. Fernandes, P. Leitao, and L. Neves (2014), Modelling of cohesive sediment dynamics in tidal estuarine systems: Case study of tagus estuary, portugal, *Estuarine, Coastal and Shelf Science*, *151*, 34–44.

Frouin, R., A. Fiuza, I. Ambar, and T. Boyd (1990), Observations of a poleward surface current off the coasts of Portugal and Spain during winter, *Journal of Geophysical Research: Oceans*, *95*(C1), 679–691.

GMAO (2015), MERRA-2 tavg3_3d_udt_Np: 3d, 3-hourly, time-averaged, pressure-level, assimilation, wind Tendencies V5. 12.4, Global Modeling and Assimilation Office, Greenbelt, MD: Goddard Earth Sciences Data and Information Services Center (GES DISC).

Gómez-Gesteira, M., L. Gimeno, M. Decastro, M. Lorenzo, I. Alvarez, R. Nieto, J. Taboada, A. Crespo, A. Ramos, I. Iglesias, et al. (2011), The state of climate in nw iberia, *Climate Research*, *48*(2-3), 109–144.

Gonçalves, D. S., L. M. Pinheiro, P. A. Silva, J. Rosa, L. Rebêlo, X. Bertin, S. Braz Teixeira, and R. Esteves (2014), Morphodynamic evolution of a sand extraction excavation offshore vale do lobo, algarve, portugal, *Coastal Engineering*, *88*, 75–87, doi:10.1016/j.coastaleng.2014.02.001.

González-Álvarez, R., P. Bernárdez, L. Pena, G. Francés, R. Prego, P. Diz, and F. Vilas (2005), Paleoclimatic evolution of the galician continental shelf (nw of spain) during the last 3000 years: from a storm regime to present conditions, *Journal of Marine Systems*, *54*(1-4), 245–260.

Grant, W. D., and O. S. Madsen (1982), Movable bed roughness in unsteady oscillatory flow, *Journal of Geophysical Research*, *87*(C1), 469, doi:10.1029/JC087iC01p00469.

Gray, J., G. C. Poore, K. Ugland, R. S. Wilson, F. Olsgard, and Ø. Johannessen (1997), Coastal and deep-sea benthic diversities compared, *Marine ecology progress series*, *159*, 97–103.

Hanebuth, T. J., and H. Lantzsch (2008), A late quaternary sedimentary shelf system under hyperarid conditions: unravelling climatic, oceanographic and sea-level controls (golfe d'arguin, mauritania, nw africa), *Marine Geology*, *256*(1-4), 77–89.

Hanebuth, T. J., H. Lantzsch, and J. Nizou (2015), Mud depocenters on continental shelves—appearance, initiation times, and growth dynamics, *Geo-Marine Letters*, *35*(6), 487–503.

Harris, C. K., and P. L. Wiberg (1997), Approaches to quantifying long-term continental shelf sediment transport with an example from the northern california stress mid-shelf site, *Continental Shelf Research*, *17*(11), 1389–1418.

Haynes, R., and E. D. Barton (1990), A poleward flow along the atlantic coast of the iberian peninsula, *Journal of Geophysical Research: Oceans*, *95*(C7), 11,425–11,441.

Hersbach, H., B. Bell, P. Berrisford, S. Hirahara, A. Horányi, J. Muñoz-Sabater, J. Nicolas, C. Peubey, R. Radu, D. Schepers, et al. (2020), The era5 global reanalysis, *Quarterly Journal of the Royal Meteorological Society*, *146*(730), 1999–2049.

Huthnance, J. M., H. M. Van Aken, M. White, E. D. Barton, B. Le Cann, E. F. Coelho, E. A. Fanjul, P. Miller, and J. Vitorino (2002), Ocean margin exchange—water flux estimates, *Journal of Marine Systems*, *32*(1-3), 107–137.

Hwang, J., E. R. Druffel, and T. I. Eglinton (2010), Widespread influence of resuspended sediments on oceanic particulate organic carbon: Insights from radiocarbon and aluminum contents in sinking particles, *Global Biogeochemical Cycles*, *24*(4).

IH (2010), Surface sediments of the portuguese continental shelf chart: Sed 2-from espinho to cape mondego. sedimentological series, *Tech. rep.*

IPCC (2014), Climate change 2014: Synthesis report. contribution of working groups i, ii and iii to the fifth assessment report of the intergovernmental panel on climate change, pp. Core Writing Team, R.K. Pachauri and L.A. Meyer (eds.). IPCC, Geneva, Switzerland, 151 pp.

Janssen, P. A. (1991), Quasi-linear theory of wind-wave generation applied to wave forecasting, *Journal of physical oceanography*, *21*(11), 1631–1642.

Jouanneau, J., O. Weber, T. Drago, A. Rodrigues, A. Oliveira, J. Dias, C. Garcia, S. Schmidt, and J. Reyss (2002), Recent sedimentation and sedimentary budgets on the western Iberian shelf, *Progress in Oceanography*, *52*, 261–275.

Jullien, S., M. Caillaud, R. Benshila, L. Bordois, G. Cambon, F. Dufois, F. Dumas, J. Gula, M. Le Corre, S. Le Gentil, F. Lemarié, P. Marchesiello, G. Morvan, and S. Theetten (2022), Technical and numerical Documentation. Release 1.2, *Tech. rep.*

Kahma, K. K., and C. J. Calkoen (1992), Reconciling Discrepancies in the Observed Growth of Wind-generated Waves, *Journal of Physical Oceanography*, *22*, doi:10.1175/1520-0485(1992)022<1389:rditog>2.0.co;2.

Karakaş, G., N. Nowald, M. Blaas, P. Marchesiello, S. Frickenhaus, and R. Schlitzer (2006), High-resolution modeling of sediment erosion and particle transport across the northwest African shelf, *Journal of Geophysical Research: Ocean*, *111*(C6).

Kari, E., J. M. Beltrán-Abaunza, E. T. Harvey, and S. Kratzer (2017), Retrieval of suspended particulate matter from turbidity– model development, validation, and application to MERIS data over the Baltic Sea, *International journal of remote sensing*, *38*(7), 1983–2003, doi:10.1080/01431161.2016.1230289.

Lalbeharry, R., and H. Ritchie (2009), Wave simulation using swan in nested and unnested mode applications, in *Proceedings of the 11th Int. Workshop on Wave Hindcasting and Forecasting, Halifax, Canada*.

Large, W. G., J. C. McWilliams, and S. C. Doney (1994), Oceanic vertical mixing: A review and a model with a nonlocal boundary layer parameterization, *Reviews of geophysics*, *32*(4), 363–403.

Lávin, A., L. Valdés, F. Sanchez, P. Abaunza, A. Forest, J. Boucher, and A. Jegou (2006), The Bay of Biscay: The encoun- tering of the ocean and the shelf, *The Global Coastal Ocean: Interdisciplinary Regional Studies and Syntheses. The Sea,*, *14*, Book Chapter 24, 933–1001.

Le Hir, P., F. Cayocca, and B. Waeles (2011), Dynamics of sand and mud mixtures: A multiprocess-based modelling strategy, *Continental Shelf Research*, *31*(10), S135–S149.

Levier, B., M. Benkiran, G. Reffray, and M. García Sottilo (2014), IBIRYS: a regional high resolution reanalysis (physical and biogeochemical) over the European North East Shelf, *EGU General Assembly Conference Abstracts*, *16*.

Li, M. Z., and C. L. Amos (2001), SEDTRANS96: The upgraded and better calibrated sediment-transport model for continental shelves, *Computers and Geosciences*, *27*(6), 619–645, doi:10.1016/S0098-3004(00)00120-5.

Li, M. Z., Y. Wu, G. Han, R. H. Prescott, and C. C. Tang (2017), A modeling study of the impact of major storms on seabed shear stress and sediment transport on the Grand Banks of Newfoundland, *Journal of Geophysical Research: Oceans*, *122*(5), 4183–4216, doi:10.1002/2016JC012215.

Liu, K.-K., L. Atkinson, R. Quiñones, and L. Talaue-McManus (2010), *Carbon and nutrient fluxes in continental margins: a global synthesis*, Springer Science & Business Media.

Liu, X.-D., S. Osher, and T. Chan (1994), Weighted essentially non-oscillatory schemes, *Journal of Computational Physics*, *115*(1), 200–212.

López-Jamar, E., R. Cal, G. González, R. Hanson, J. Rey, G. Santiago, and K. Tenore (1992), Upwelling and outwelling effects on the benthic regime of the continental shelf off Galicia, NW Spain, *Journal of Marine Research*, *50*(3), 465–488, doi:10.1357/002224092784797584.

Lorente, P., M. G. Sotillo, L. Aouf, A. Amo-Baladrón, E. Barrera, A. Dalphinet, C. Toledano, R. Rainaud, M. De Alfonso, S. Piedracoba, et al. (2017), Extreme wave height events in nw spain: a combined multi-sensor and model approach, *Remote Sensing*, *10*(1), 1.

Madsen, O. S., and W. D. Grant (1977), Quantitative description of sediment transport by waves., in *15th International Conference on Coastal Engineering, 1976*, pp. 1092–1112.

Maestro, A., J. López-Martínez, E. Llave, F. Bohoyo, J. Acosta, F. J. Hernández-Molina, A. Muñoz, and G. Jané (2013), Geomorphology of the Iberian Continental Margin, *Geomorphology*, *196*, 13–35, doi:10.1016/j.geomorph.2012.08.022.

Marchesiello, P., L. Debreu, and X. Couvelard (2009), Spurious diapycnal mixing in terrain-following coordinate models: The problem and a solution, *Ocean Modelling*, *26*(3-4), 156–169.

Mason, E., S. Coombs, and P. Oliveira (2005), An overview of the literature concerning the oceanography of the eastern north atlantic region, *Relatórios Científicos e Técnicos IPIMAR série digital*, *33*, 59.

McCave, I. N., and Omex II partners (2000), Aspects of sediment transport on the northern iberian margin, in *Exchange Processes at the Ocean Margins. 32nd International Liege Colloquium on Ocean Hydrodynamics. Proceedings*, p. 45.

Mendes, R., M. C. Sousa, M. DeCastro, M. Gómez-Gesteira, and J. M. Dias (2016), New insights into the Western Iberian Buoyant Plume: Interaction between the Douro and Minho River plumes under winter conditions, *Progress in Oceanography*, *141*, 30–43, doi:10.1016/j.pocean.2015.11.006.

Miles, T., G. Seroka, J. Kohut, O. Schofield, and S. Glenn (2015), Glider observations and modeling of sediment transport in Hurricane Sandy, *Journal of Geophysical Research C: Oceans*, *120*(3), 1771–1791, doi:10.1002/2014JC010474.

Muller-Karger, F. E., R. Varela, R. Thunell, R. Luerssen, C. Hu, and J. J. Walsh (2005), The importance of continental margins in the global carbon cycle, *Geophysical research letters*, *32*(1).

Nielsen, P. (1986), Suspended sediment concentrations under waves, *Coastal Engineering Journal*, *10*(1), 23–31, doi:10.1016/0378-3839(86)90037-2.

Nielsen, P. (1992), *Coastal bottom boundary layers and sediment transport*, vol. 4, World Scientific Publishing.

Nikuradse, J. (1933), Laws for flows in rough pipes, translated from German [Strömungsgesetz in rauhren Rohen], NACA Tech. Memo. 1292, 62 pp., *Tech. rep.*, Natl. Advisory Commission for Aeronautics, Washington, D. C.

Nolasco, R., A. C. Pires, N. Cordeiro, B. Le Cann, and J. Dubert (2013), A high-resolution modeling study of the Western Iberian Margin mean and seasonal upper ocean circulation, *Ocean Dynamics*, *63*(9-10), 1041–1062, doi:10.1007/s10236-013-0647-8.

Oberle, F. K., C. D. Storlazzi, and T. J. Hanebuth (2014), Wave-driven sediment mobilization on a storm-controlled continental shelf (Northwest Iberia), *Journal of Marine Systems*, *139*, 362–372, doi:10.1016/j.jmarsys.2014.07.018.

Oliveira, A., F. Rocha, A. Rodrigues, J. Jouanneau, A. Dias, O. Weber, and C. Gomes (2002a), Nepheloid layer dynamics in the northern Portuguese shelf, *Progress in Oceanography*, *52*(2-4), 195–213, doi:10.1016/S0079-6611(02)00006-X.

Oliveira, A., F. Rocha, A. Rodrigues, J. Jouanneau, A. Dias, O. Weber, and C. Gomes (2002b), Clay minerals from the sedimentary cover from the northwest Iberian shelf, *Progress in Oceanography*, *52*(2-4), 233–247, doi:10.1016/S0079-6611(02)00008-3.

Oliveira, A., A. Santos, R. Santos, and N. Zacarias (2023), Nepheloid layer dynamics overview of the portuguese continental shelf, *Continental Shelf Research*, *261*, 105,027.

Oliveira, I., A. Valle, and F. Miranda (1982), Littoral problems in the Portuguese west coast, in *Coastal Engineering 1982 proceedings, III*, pp. 1950–1969.

Oliveira, P. B., R. Nolasco, J. Dubert, T. Moita, and Á. Peliz (2009), Surface temperature, chlorophyll and advection patterns during a summer upwelling event off central Portugal, *Continental Shelf Research*, *29*(5-6), 759–774, doi:10.1016/j.csr.2008.08.004.

Otero, P., M. Ruiz-Villarreal, Á. Peliz, and J. M. Cabanas (2010), Climatology and reconstruction of runoff time series in northwest Iberia: influence in the shelf buoyancy budget off Ría de Vigo, *Scientia Marina*, *74*(2), 247–266, doi:10.3989/scimar.2010.74n2247.

Peliz, Á., T. L. Rosa, A. M. P. Santos, and J. L. Pissarra (2002), Fronts, jets, and counterflows in the Western Iberian upwelling system, *Journal of Marine Systems*, *35*(1-2), 61–77, doi:10.1016/S0924-7963(02)00076-3.

Peliz, Á., J. Dubert, and D. B. Haidvogel (2003a), Subinertial Response of a Density-Driven Eastern Boundary Poleward Current to Wind Forcing, *Journal of Physical Oceanography*, *33*(8), 1633–1650, doi:10.1175/2415.1.

Peliz, Á., J. Dubert, D. B. Haidvogel, and B. L. Cann (2003b), Generation and unstable evolution of a density-driven Eastern Poleward Current: The Iberian Poleward Current, *Journal of Geophysical Research*, *108*(C8), 3268, doi:10.1029/2002JC001443.

Pensieri, S., R. Bozzano, and M. E. Schiano (2010), Comparison between quikscat and buoy wind data in the ligurian sea, *Journal of Marine Systems*, *81*(4), 286–296.

Penven, P., L. Debreu, P. Marchesiello, and J. C. McWilliams (2006), Evaluation and application of the ROMS 1-way embedding procedure to the central california upwelling system, *Ocean Modelling*, *12*(1-2), 157–187, doi:10.1016/j.ocemod.2005.05.002.

Pierson, W. J., and L. Moskowitz (1964), A proposed spectral form for fully developed wind seas based on the similarity theory of S. A. Kitaigorodskii, *Journal of Geophysical Research*, *69*(24), 5181–5190, doi:10.1029/jz069i024p05181.

Pinheiro, L., R. Wilson, R. Pena dos Reis, R. Whitmarsh, and A. Ribeiro (1996), The western iberia margin: a geophysical and geological overview, in *Proceedings-ocean Drilling Program Scientific Results*, pp. 3–26, National Science Foundation.

Pinto, L., A. B. Fortunato, Y. Zhang, A. Oliveira, and F. E. P. Sancho (2012), Development and validation of a three-dimensional morphodynamic modelling system for non-cohesive sediments, *Ocean Modelling*, *57*, 1–14, doi:10.1016/j.ocemod.2012.08.005.

Pita, C., and J. Santos (1989), Análise dos temporais da costa oeste de portugal continental, *Relatório PO_ WAVES 1/89-A*.

Quaresma, L. S., and A. Pichon (2013), Modelling the barotropic tide along the west-iberian margin, *Journal of Marine Systems*, *109*, S3–S25.

Ramos, A. M., R. Ramos, P. Sousa, R. M. Trigo, M. Janeira, and V. Prior (2011), Cloud to ground lightning activity over portugal and its association with circulation weather types, *Atmospheric Research*, *101*(1-2), 84–101.

Relvas, P., E. D. Barton, J. Dubert, P. B. Oliveira, Á. Peliz, J. C. da Silva, and A. M. P. Santos (2007), Physical oceanography of the western Iberia ecosystem: Latest views and challenges, *Progress in Oceanography*, *74*(2-3), 149–173, doi:10.1016/j.pocean.2007.04.021.

Rey, D., P. Álvarez-Iglesias, M. Araújo, A. Bernabeu, M. Comas, M. DeCastro, M. Druet, E. Ferreira Da Silva, A. Ferrín, M. Gesteira, et al. (2014), Chapter 8 the nw iberian continental shelf, *Geological Society, London, Memoirs*, *41*(1), 91–108.

Rey, J. (1993), Relacion morphose dimentaria entre la platforma continental de Galicia y las Rias bajas y su evolucion durante el Cuaternario, *Publicaciones Especiales Instituto de Oceanografia*, (17), 233.

Rosenberg, R. (2001), Marine benthic faunal successional stages and related sedimentary activity, *Scientia Marina*, *65*(S2), 107–119.

Rossi, V., V. Garçon, J. Tassel, J.-B. Romagnan, L. Stemmann, F. Jourdin, P. Morin, and Y. Morel (2013), Cross-shelf variability in the iberian peninsula upwelling system: Impact of a mesoscale filament, *Continental Shelf Research*, *59*, 97–114.

Rusu, E., and C. Guedes Soares (2009), Numerical modelling to estimate the spatial distribution of the wave energy in the Portuguese nearshore, *Renewable Energy*, *34*(6), 1501–1516, doi:10.1016/j.renene.2008.10.027.

Rusu, L., and C. G. Soares (2013), Evaluation of a high-resolution wave forecasting system for the approaches to ports, *Ocean Engineering*, *58*, 224–238, doi:10.1016/j.oceaneng.2012.11.008.

Rusu, L., S. de León, and C. Soares (2015), Numerical modelling of the North Atlantic storms affecting the West Iberian coast, in *Maritime Technology and Engineering*, pp. 1365–1370, doi:10.1201/b17494-184.

Saha, S., S. Moorthi, X. Wu, J. Wang, S. Nadiga, P. Tripp, D. Behringer, Y.-T. Hou, H.-Y. Chuang, M. Iredell, et al. (2011a), NCEP climate forecast system version 2 (CFSv2) 6-hourly products, *Research Data Archive at the National Center for Atmospheric Research, Computational and Information Systems Laboratory*.

Saha, S., S. Moorthi, X. Wu, J. Wang, S. Nadiga, P. Tripp, D. Behringer, Y. Hou, H. ya Chuang, M. Iredell, et al. (2011b), NCEP Climate Forecast System Version 2 (CFSv2) Selected Hourly Time- Series Products, *Research Data Archive at the National Center for Atmospheric Research, Computational and Information Systems Laboratory*.

Saha, S., S. Moorthi, X. Wu, J. Wang, S. Nadiga, P. Tripp, D. Behringer, Y.-T. Hou, H.-y. Chuang, M. Iredell, et al. (2014), The NCEP climate forecast system version 2, *Journal of Climate*, *27*(6), 2185–2208.

Santos, A. (2021), Sediment concentration and particle size in the water column using acoustic methods: Application to the Douro and Minho Estuaries, Ph.D. thesis, University of Lisbon.

Santos, Â., S. Mendes, and J. Corte-Real (2014), Impacts of the storm hercules in portugal, *Finisterra*, *49*(98).

Semedo, A., K. Sušelj, A. Rutgersson, and A. Sterl (2011), A global view on the wind sea and swell climate and variability from era-40, *Journal of Climate*, *24*(5), 1461–1479.

Shafiei, H., J. Chauchat, C. Bonamy, and P. Marchesiello (2022), Numerical simulation of on-shore/off-shore sandbar migration using wave-cycle concept – application to a 3d wave-averaged oceanic model (croco), *in preparation for Ocean Modelling*.

Sharp, E., P. Dodds, M. Barrett, and C. Spataru (2015), Evaluating the accuracy of cfsr reanalysis hourly wind speed forecasts for the uk, using in situ measurements and geographical information, *Renewable Energy*, *77*, 527–538.

Shchepetkin, A. F., and J. C. McWilliams (1998), Quasi-Monotone Advection Schemes Based on Explicit Locally Adaptive Dissipation, *Monthly Weather Review*, *126*(6), 1541–1580, doi:10.1175/1520-0493(1998)126<1541:QMASBO>2.0.CO;2.

Shchepetkin, A. F., and J. C. McWilliams (2003), A method for computing horizontal pressure-gradient force in an oceanic model with a nonaligned vertical coordinate, *Journal of Geophysical Research*, *108*(C3), 3090, doi:10.1029/2001JC001047.

Shchepetkin, A. F., and J. C. McWilliams (2005), The regional oceanic modeling system (ROMS): A split-explicit, free-surface, topography-following-coordinate oceanic model, *Ocean Modelling*, *9*(4), 347–404, doi:10.1016/j.ocemod.2004.08.002.

Shepard, F. P. (1954), Nomenclature based on sand-silt-clay ratios, *Journal of sedimentary Research*, *24*(3), 151–158.

Sherwood, C. R., R. P. Signell, and J. C. Warner (2005), Building a community sediment transport model, report, *Tech. rep.*

Silva, D., A. R. Bento, P. Martinho, and C. Guedes Soares (2015), High resolution local wave energy modelling in the Iberian Peninsula, *Energy*, *91*, 099–1112, doi:10.1016/j.energy.2015.08.067.

Skamarock, W. C., J. B. Klemp, J. Dudhia, D. O. Gill, Z. Liu, J. Berner, W. Wang, J. G. Powers, M. G. Duda, D. M. Barker, and X.-Y. Huang (2019), A description of the advanced research wrf version 4., *Tech. rep.*, NCAR Tech. Note NCAR/TN-556+STR.

Smith, J., and S. McLean (1977), Spatially averaged flow over a wavy surface, *Journal of Geophysical Research*, *82*(12), 1735–1746.

Snelgrove, P. V. R. (1999), Getting to the Bottom of Marine Biodiversity: Sedimentary Habitats, *BioScience*, *49*(2), 129, doi:10.2307/1313538.

Soares, C. G., A. R. Bento, M. Gonçalves, D. Silva, and P. Martinho (2014), Numerical evaluation of the wave energy resource along the atlantic european coast, *Computers & Geosciences*, *71*, 37–49.

Sommerfield, C. K., and R. A. Wheatcroft (2007), Late holocene sediment accumulation on the northern california shelf: Oceanic, fluvial, and anthropogenic influences, *Geological Society of America Bulletin*, *119*(9-10), 1120–1134.

SonTek.Inc (1997), Doppler current meters - using signal strength to monitor suspended sediment concentration; sontek technical notes; sontek inc.: San diego, ca, usa, *Tech. rep.*

Soulsby, R. L. (1995), *Bed shear-stresses due to combined waves and currents*, 4.20–4.23 pp., Wiley and Sons, Delft, The Netherlands.

Soulsby, R. L. (1997), *Dynamics of marine sands: a manual for practical applications*, Thomas Telford Publications, doi:10.1680/doms.25844.

Soulsby, R. L., L. Hamm, G. Klopman, D. Myrhaug, R. Simons, and G. Thomas (1993), Wave-current interaction within and outside the bottom boundary layer, *Coastal Engineering*, *21*(1-3), 41–69.

Stopa, J. E., and K. F. Cheung (2014), Intercomparison of wind and wave data from the ecmwf reanalysis interim and the ncep climate forecast system reanalysis, *Ocean Modelling*, *75*, 65–83.

SWAN (2013), Scientific and Technical Documentation: SWAN Cycle III version 40.51, *Tech. rep.*

SWAN (2016), SWAN User Manual. SWAN Cycle III Version 41.10. Delft University of Technology, *Tech. rep.*

Sykes, P. A., and R. M. Barciela (2012), Assessment and development of a sediment model within an operational system, *Journal of Geophysical Research: Oceans*, *117*(C4), doi: 10.1029/2011JC007420.

Teles-Machado, A., A. Peliz, J. C. McWilliams, X. Couvelard, and I. Ambar (2016), Circulation on the northwestern iberian margin: Vertical structure and seasonality of the alongshore flows, *Progress in Oceanography*, *140*, 134–153.

Thomsen, L. (2002), The benthic boundary layer, in *Ocean margin systems*, pp. 143–155, Springer.

Thomsen, L., G. Gust, et al. (2002), Processes in the benthic boundary layer at the iberian continental margin and their implication for carbon mineralization, *Progress in Oceanography*, *52*(2-4), 315–329.

Thrush, S. F., and P. K. Dayton (2002), Disturbance to marine benthic habitats by trawling and dredging: implications for marine biodiversity, *Annual review of ecology and systematics*, pp. 449–473.

Tolman, H. L. (1989), The numerical model WAVEWATCH: a third generation model for hindcasting of wind waves on tides in shelf seas, *Communications on Hydraulic and Geotechnical Engineering, Delft Univ. of Techn*, *89*(2), 72 p.

Uchiyama, Y., J. C. McWilliams, and A. F. Shchepetkin (2010), Wave–current interaction in an oceanic circulation model with a vortex-force formalism: Application to the surf zone, *Ocean Modelling*, *34*(1-2), 16–35.

van der Westhuysen, A. J. (2012), Spectral modeling of wave dissipation on negative current gradients, *Coastal Engineering*, *68*, 17–30.

van der Westhuysen, A. J., M. Zijlema, and J. A. Battjes (2007), Nonlinear saturation-based whitecapping dissipation in SWAN for deep and shallow water, *Coastal Engineering*, *54*(2), 151–170, doi:10.1016/j.coastaleng.2006.08.006.

van Rijn, L. C. (2007), Unified view of sediment transport by currents and waves. I: Initiation of motion, bed roughness, and bed-load transport, *Journal of Hydraulic Engineering*, *133*(6), 649–667, doi:10.1061/(ASCE)0733-9429(2007)133:6(649).

Van Weering, T. C., H. De Stigter, W. Boer, and H. De Haas (2002), Recent sediment transport and accumulation on the nw iberian margin, *Progress in Oceanography*, *52*(2-4), 349–371.

Viitak, M., I. Maljutenko, V. Alari, Ü. Suursaar, S. Rikka, and P. Lagemaa (2016), The impact of surface currents and sea level on the wave field evolution during st. jude storm in the eastern baltic sea, *Oceanologia*, *58*(3), 176–186.

Viitak, M., P. Avilez-Valente, A. Bio, L. Bastos, and I. Iglesias (2020), Evaluating wind datasets for wave hindcasting in the nw iberian peninsula coast, *Journal of Operational Oceanography*, *Online*, 1–14.

Vilas, F., A. M. Bernabeu, and G. Méndez (2005), Sediment distribution pattern in the Rias Baixas (NW Spain): Main facies and hydrodynamic dependence, *Journal of Marine Systems*, *54*(1-4 SPEC. ISS.), 261–276, doi:10.1016/j.jmarsys.2004.07.016.

Villacieros-Robineau, N. (2017), Bottom boundary layer dynamics and its effects on particle resuspension and transport in the NW Iberina coastal upwelling system, Doctoral dissertation, University of Vigo.

Villacieros-Robineau, N., J. L. Herrera, C. G. Castro, S. Piedracoba, and G. Rosón (2013), Hydrodynamic characterization of the bottom boundary layer in a coastal upwelling system (ría de vigo, nw spain), *Continental Shelf Research*, *68*, 67–79.

Villacieros-Robineau, N., D. Zúñiga, B. Barreiro-González, F. Alonso-Pérez, F. de la Granda, M. Froján, C. A. Collins, E. D. Barton, and C. G. Castro (2019), Bottom Boundary Layer and Particle Dynamics in an Upwelling Affected Continental Margin (NW Iberia), *Journal of Geophysical Research: Oceans*, *124*(12), 9531–9552, doi:10.1029/2019JC015619.

Vitorino, J. (1989), Circulação residual ao largo da costa nw de portugal durante a estação de afloramento de 1987, *Anais do Instituto Hidrográfico*, *10*, 25–37.

Vitorino, J., A. Oliveira, J. Jouanneau, and T. Drago (2000), Winter dynamics and the transport of fine sediments on the northern portuguese shelf, *3º Simpósio sobre a Margem Continental Ibérica Atlântica, Faro*, pp. 279–280.

Vitorino, J., A. Oliveira, J. M. Jouanneau, and T. Drago (2002a), Winter dynamics on the northern Portuguese shelf. Part 2: Bottom boundary layers and sediment dispersal, *Progress in Oceanography*, *52*(2-4), 155–170, doi:10.1016/S0079-6611(02)00004-6.

Vitorino, J., A. Oliveira, J. M. Jouanneau, and T. Drago (2002b), Winter dynamics on the northern portuguese shelf. Part 1: Physical processes, *Progress in Oceanography*, *52*(2-4), 129–153, doi:10.1016/S0079-6611(02)00003-4.

WAMDIG (1988), The wam model—a third generation ocean wave prediction model, *Journal of Physical Oceanography*, *18*(12), 1775–1810.

Warner, J. C., C. R. Sherwood, R. P. Signell, C. K. Harris, and H. G. Arango (2008), Development of a three-dimensional, regional, coupled wave, current, and sediment-transport model, *Computers and Geosciences*, *34*(10), 1284–1306, doi:10.1016/j.cageo.2008.02.012.

Warner, J. C., B. Armstrong, R. He, and J. B. Zambon (2010), Development of a Coupled Ocean-Atmosphere-Wave-Sediment Transport (COAWST) Modeling System, *Ocean Modelling*, *35*(3), 230–244, doi:10.1016/j.ocemod.2010.07.010.

Willmott, C. J. (1981), On the validation of models, *Physical geography*, *2*(2), 184–194.

Wollast, R. (1998), Evaluation and comparison of the global carbon cycle in the coastal zone and in the open ocean, *The Sea, Vol. 10*, pp. 213–252.

Wooster, W. S., a. Bakun, and D. R. McLain (1976), The seasonal upwelling cycle along the North Atlantic, *Journal of Marine Research*, *34*(2), 131–141.

Xing, J., and A. Davies (2002), Influence of wind direction, wind waves, and density stratification upon sediment transport in shelf edge regions: The Iberian shelf, *Journal of Geophysical Research: Oceans*, *107*(C8), 1–16, doi:10.1029/2001jc000961.

Xing, J., and A. M. Davies (2003a), A model study of tidally induced suspended sediment transport in the Iberian shelf edge region, *Estuarine, Coastal and Shelf Science*, *58*(2), 321–333, doi:10.1016/S0272-7714(03)00084-2.

Xing, J., and A. M. Davies (2003b), A model study of tidally induced suspended sediment transport in the Iberian shelf edge region, *Estuarine, Coastal and Shelf Science*, *58*(2), 321–333, doi:10.1016/S0272-7714(03)00084-2.

Zhang, W., Y. Cui, A. I. Santos, and T. J. Hanebuth (2016), Storm-driven bottom sediment transport on a high-energy narrow shelf (NW Iberia) and development of mud depocenters, *Journal of Geophysical Research: Oceans*, *121*(8), 5751–5772, doi:10.1002/2015JC011526.

Zhang, W., I. Didenkulova, O. Kurkina, Y. Cui, J. Haberkern, R. Aepfler, A. I. Santos, H. Zhang, and T. J. Hanebuth (2019), Internal solitary waves control offshore extension of mud depocenters on the NW Iberian shelf, *Marine Geology*, *409*, 15–30.

Zúñiga, D., N. Villacieros-Robineau, E. Salgueiro, F. Alonso-Pérez, G. Rosón, F. Abrantes, and C. G. Castro (2016), Particle fluxes in the nw iberian coastal upwelling system: Hydrodynamical and biological control, *Continental Shelf Research*, *123*, 89–98.

Zúñiga, D., and C. G. Castro (2019), RAIA sediment trap total mass fluxes near Cape Silleiro (NW Iberia), doi:10.20350/digitalCSIC/8958.